

2017 SUMMER RESEARCH PROGRAM FOR HIGH SCHOOL JUNIORS

AT THE

UNIVERSITY OF ROCHESTER'S

LABORATORY FOR LASER ENERGETICS

STUDENT RESEARCH REPORTS

PROGRAM DIRECTOR

Dr. R. Stephen Craxton

February 2019

Lab Report 414

2017 SUMMER RESEARCH PROGRAM FOR HIGH SCHOOL JUNIORS

AT THE

UNIVERSITY OF ROCHESTER'S

LABORATORY FOR LASER ENERGETICS

STUDENT RESEARCH REPORTS

PROGRAM DIRECTOR

Dr. R. Stephen Craxton

LABORATORY FOR LASER ENERGETICS

University of Rochester

250 East River Road

Rochester, NY 14623-1299

During the summer of 2017, 11 students from Rochester-area high schools participated in the Laboratory for Laser Energetics' Summer High School Research Program. The goal of this program is to excite a group of high school students about careers in the areas of science and technology by exposing them to research in a state-of-the-art environment. Too often, students are exposed to "research" only through classroom laboratories, which have prescribed procedures and predictable results. In LLE's summer program, the students experience many of the trials, tribulations, and rewards of scientific research. By participating in research in a real

environment, the students often become more excited about careers in science and technology. In addition, LLE gains from the contributions of the many highly talented students who are attracted to the program.

The students spent most of their time working on their individual research projects with members of LLE's scientific staff. The projects were related to current research activities at LLE and covered a broad range of areas of interest including laser physics, computational modeling of implosion physics, experimental diagnostic development, laser system diagnostics, physical chemistry, cryogenic target characterization, and web-based data analysis. The students, their high schools, their LLE supervisors, and their project titles are listed in the table. Their written reports are collected in this volume. By working through several iterations of their project reports, incorporating feedback from their supervisors and the Program Director, the students experience most of the steps involved in preparing a scientific paper for publication.

The students attended weekly seminars on technical topics associated with LLE's research. Topics this year included laser physics, fusion, holography, nonlinear optics, atomic force microscopy, laser focusing, and pulsed power. The students also received safety training, learned how to give scientific presentations, and were introduced to LLE's resources, especially the computational facilities.

The program culminated on 30 August with the "High School Student Summer Research Symposium," at which the students presented the results of their research to an audience including parents, teachers, and LLE staff. Each student spoke for approximately ten minutes and answered questions. At the symposium LLE presented its 21st annual William D. Ryan Inspirational Teacher Award. The recipient this year was Mrs. Lois Houlihan, a chemistry teacher at Pittsford Mendon High School. This award honors a teacher, nominated by alumni of

the LLE program, who has inspired outstanding students in the areas of science, mathematics, and technology. Mrs. Houlihan was nominated by Sapna Ramesh, a participant in the 2016 Summer Program.

A total of 364 high school students have participated in the program from its inception in 1989 through 2017. The students in 2017 were selected from approximately 60 applicants. Each applicant submitted an essay describing his or her interests in science and technology, a copy of his or her transcript, and a letter of recommendation from a science or math teacher.

In the past, several participants of this program have gone on to become scholars (formerly known as “semifinalists”) and finalists in the prestigious Regeneron (formerly Intel) Science Talent Search. This tradition of success continued this year with the selection of Nikhil Bose and Yujia Yang as two of the 300 Regeneron Scholars chosen from over 1800 applicants nationwide.

LLE plans to continue this program in future years. The program is strictly for students from Rochester-area high schools who have just completed their junior year. Application information is mailed to schools and placed on the LLE web site in early February with an application deadline near the middle of March. For more information about the program, please contact Dr. R. Stephen Craxton at LLE.

This program was supported by the U.S. Department of Energy Office of Inertial Confinement Fusion under Cooperative Agreement No. DE-NA0001944.

Table I: High School Students and Projects—Summer 2017.

Name	High School	Supervisor	Project Title
Viknesh Baskar	Webster Schroeder	J. P. Knauer and C. J. Forrest	Ion Temperature Analysis of Neutron Time-of-Flight Data
Nikhil Bose	Pittsford Sutherland	M. J. Guardalben	Compensation for Self-Focusing on the OMEGA EP Laser by Use of Frequency Conversion
Benjamin Chabak	Byron Bergen	J. P. Knauer and C. J. Forrest	Design and Analysis of Cherenkov Radiation Detectors
Meshach Cornelius	Gates Chili	T. Walker and G. Brent	Characterization and Detection of the Deteriorization of Electrical Connectors in a Flash-Lamp System
Griffin Cross	Pittsford Sutherland	W. T. Shmayda	Study of the Hydrogen Palladium System
Matthew Galan	Fairport	R. W. Kidder	Data Services for Scientific Analysis on OMEGA and OMEGA EP
Claire Guo	Penfield	A. Bose and R. Epstein	Analysis of Hot Spot Asymmetries Using Synthetic X-Ray Images
Joyce Luo	Pittsford Mendon	K. L. Marshall	Ambient-Temperature Ammonia Removal Process for Sol-Gel Anti-Reflective Coating Solutions
Jonathan Moore	Pittsford Sutherland	M. D. Wittman and A. Kalb	Predetermination of DT Fuel Mass in Cryogenic Target Capsules from Any Viewing Angle
Arian Nadjimzadah	Brighton	W. T. Shmayda	Modifying Stainless Steel Surfaces by Electropolishing
Yujia Yang	Brighton	R. S. Craxton	Improving the Uniformity of <i>Revolver</i> Designs for the National Ignition Facility

Compensation for Self-Focusing on the OMEGA EP Laser by Use of Frequency Conversion

Nikhil Bose

Sutherland High School

Advisor: Mark Guardalben

Laboratory for Laser Energetics

University of Rochester

November 2017

1. Abstract:

High-energy, short-pulse laser systems, such as OMEGA EP at the University of Rochester's Laboratory for Laser Energetics, must be carefully designed and operated to avoid laser-induced damage to their many optical components. OMEGA EP is a petawatt-class laser system and global resource for basic science research in high-energy-density physics.¹ One common pathway to damage among such laser systems is self-focusing of the laser beam caused by a nonlinear response of optical materials to high-intensity laser light. Maintaining the laser intensity below the damage threshold requires the beam size to be large, driving up the fabrication cost of optical components and increasing the design and operational complexity of the laser system. Even for large beam sizes, the maximum energy must be limited to avoid the self-focusing effect. For example, shots on the short-pulse beamlines of OMEGA EP are limited to below their maximum design energy for pulse widths of 100 ps to avoid damage from small-scale self-focusing. We have developed a simulation model to explore the use of a frequency conversion crystal that is inserted into an OMEGA EP beamline to compensate for this self-focusing. A Matlab frequency conversion model was developed and used to design a crystal whose effective nonlinear response partially cancels the nonlinear response that produces self-focusing of the beam. By incorporating this model into an OMEGA EP system model,² it was shown that a 4.5-cm DKDP crystal reduces the peak-to-mode modulation in the beam by up to 10%. This suggests that it might be possible to increase the on-target energy limit in OMEGA EP to close to its design energy for 100-ps shots.

2. Introduction:

On the short-pulse beamlines of OMEGA EP, shots are limited to below their maximum design energy in order to reduce the risk of damage to many of the optical components in the laser system. As the beam propagates, spatially localized regions of high intensity form across the face of the beam by the process of self-focusing, increasing the risk of damage. For 100-ps pulse widths on OMEGA EP, the self-focusing effect is greater at higher laser energies. In order to increase the beamline energy, it is necessary to limit the formation of high intensity spikes across the beam by reducing the self-focusing effect. This effect originates from the intensity-dependent refractive index of the optical components, causing small intensity modulations that initially exist across the laser beam to grow nonlinearly as the beam propagates through the laser system. Self-focusing occurs because the intensity-dependent refractive index imparts nonlinear (B-integral) phase to the beam, effectively producing localized “lenslets” across the beam where the laser beam’s phase changes rapidly.

In this work, we investigate the use of a deuterated potassium dihydrogen phosphate (DKDP) frequency conversion crystal to reduce the self-focusing effect by producing an intensity-dependent phase opposite in sign to that produced by the intensity-dependent refractive index. The crystal imparts an intensity-dependent compensating phase to the laser beam by converting the fundamental frequency of the laser to its second harmonic, and then back again to the fundamental in a cascaded frequency conversion process. In second-harmonic generation (SHG), such crystals are typically used to maximize the second-harmonic conversion efficiency by precisely aligning the crystallographic axes to the input beam direction such that the SHG process is phase-matched. In the cascaded frequency conversion process, the crystal is angularly detuned away from the phase-matched angle so that the energy, while remaining mostly in the form of the fundamental, cycles between the fundamental and second harmonic. Compensation for self-focusing by use of frequency conversion was demonstrated in BBO (beta barium borate) under very different laser conditions than exist in OMEGA EP.³ The large beam size of fusion-scale lasers such as OMEGA EP constrains the choice of crystals to the KDP family of crystals, imposing unique design complexities. We show that by careful choice of crystal length and detuning angle, phase compensation and maximum fundamental wave throughput can be achieved simultaneously.

This report is organized as follows. In Section 3, we provide a background to the problem by briefly describing the origin of laser beam self-focusing and showing its effect on the OMEGA EP beam. In Section 4, the theory of the cascaded frequency conversion process is described. Section 5 discusses the crystal design methodology with considerations specific to OMEGA EP. Section 6 presents the proposed design solution and expected reduction in self-focusing. We provide concluding remarks in Section 7.

3. Background

Due to small-scale beam modulation, the on-target energy of Beam 2 in OMEGA EP is limited to 2300 Joules for 100-ps pulses, which is 300 J below the design energy of 2600 J. As shown by the measured near-field beam profiles in Fig. 1, small-scale beam modulation caused by self-focusing and the risk of laser damage are greater for higher energy shots when the pulse width is held constant. In Fig. 1, (a) is an image of a lower energy shot while (b) is a higher energy shot.

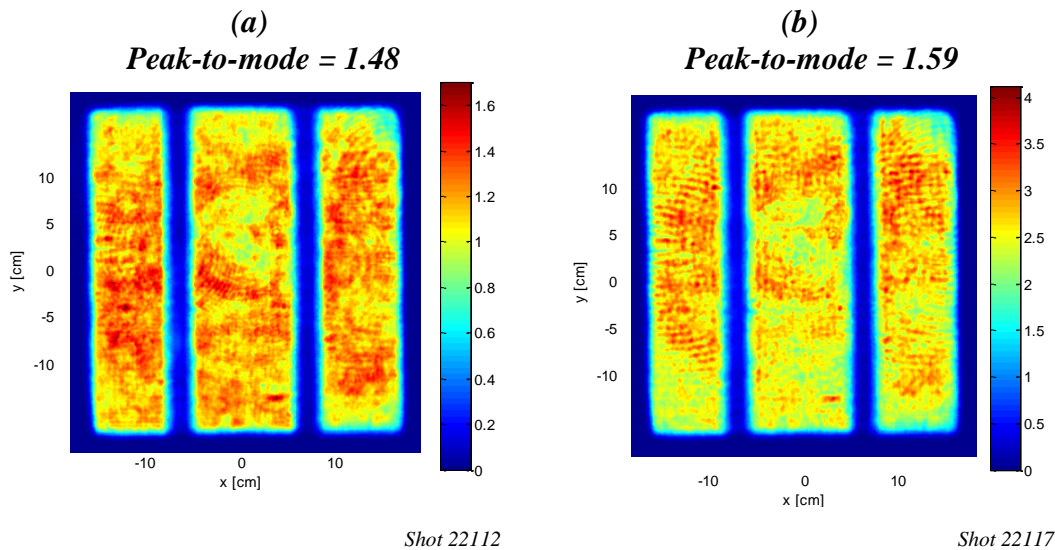


Figure 1: Measured near-field beam fluence of OMEGA EP Beam 2 at 100-ps pulse width at (a) low energy (1151 J) and (b) high energy (2600 J). The small-scale beam modulation, represented by the peak to mode* fluence of the beam, and the risk of laser damage are greater for higher intensity shots. Units of fluence are J/cm^2 .

*Peak to mode is the ratio of the maximum fluence in the beam to the most common value, thus it is a good way to measure how uniformly the energy is spread across the beam.

Fig. 2 describes how the intensity dependent refractive index, n_2 , can cause a laser beam to self-focus. The total refractive index can be written as

$$n = n_0 + n_2 I \quad (1)$$

where n is the refractive index, n_0 and n_2 are the linear and nonlinear parts of the refractive index, respectively, and I is the intensity of the light.⁴ Eq. (1) states that as the intensity (I) increases, the refractive index (n) also increases. Since refractive index is a measure of the phase velocity of the light within a substance and a higher refractive index corresponds to a delay in phase, the beam's phase front is impeded at locations of higher intensity for positive values of n_2 . This effect is illustrated in Fig. 2. For a beam entering a positive n_2 material with an initially Gaussian intensity profile, a phase curvature is imparted to the beam's wavefront that produces an intensity spike at its center upon further propagation (Fig. 2c). Phase is accumulated via the B-integral phase equation:

$$B(x, y) = \frac{2\pi}{\lambda} \sum_{optics} n_2 L_{optic} I_{optic}(x, y) \quad (2)$$

where λ is the wavelength, L_{optic} is the length of the optic, and $I_{optic}(x, y)$ is the intensity of the beam at the point (x, y) .

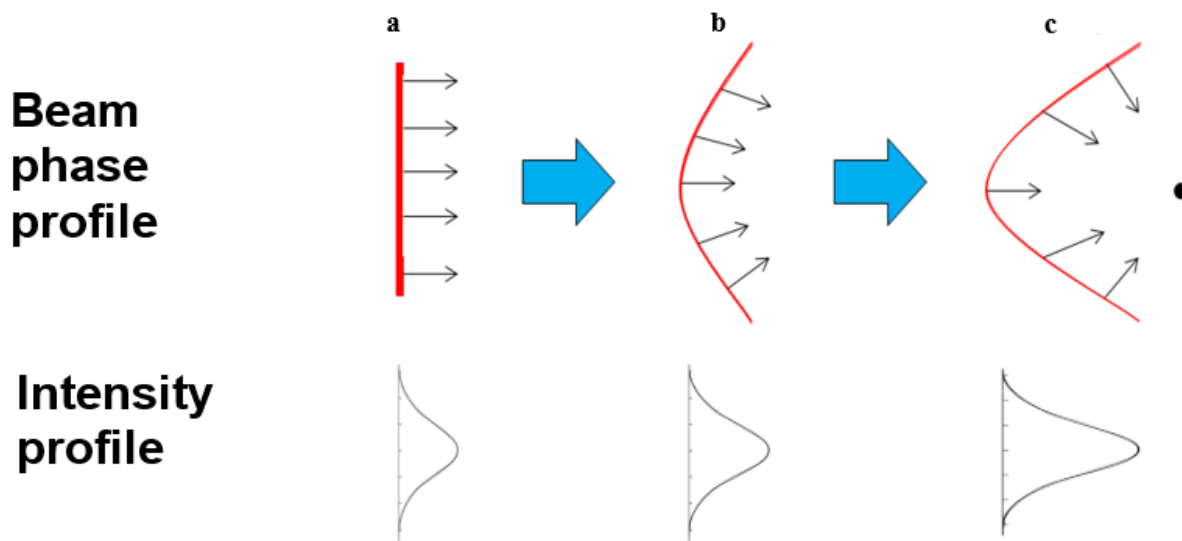


Figure 2: Phase and intensity profile for a beam showing the effect of the B-integral phase. As the beam propagates, the energy becomes more concentrated at the center due to self-focusing. (a) The phase front is initially flat and the intensity is initially Gaussian. (b) As the beam propagates, the beam's phase is impeded at locations where the intensity is higher due to the intensity-dependent refractive index. Since the direction of propagation is perpendicular to the beam's phase front, the energy gets more concentrated at the beam's center. (c) Further self-focusing occurs with propagation where the risk of damage to many of the optical components of the laser is high.

In addition to this whole beam self-focusing effect, small-scale self-focusing can occur if the beam contains localized regions of higher and lower intensity. For example, diffraction

around dust particles on the surfaces of optical components in OMEGA EP produces intensity modulation that can seed the self-focusing process.

4. Theory of Cascaded Frequency Conversion

In phase-matched SHG, the phase relationship between an input fundamental wave and its generated second harmonic is fixed such that maximum conversion efficiency is achieved. As shown in Fig. 3, in non-phase-matched (e.g., angularly detuned) SHG, the input beam, while remaining mostly as the fundamental, cycles between its fundamental frequency and its second harmonic frequency as it propagates through the crystal. The rate at which this cycling occurs is intensity dependent. This periodic energy exchange between the fundamental wave and the second harmonic wave produces a corresponding intensity-dependent nonlinear phase shift in the fundamental wave.⁵ Because the process is not phase matched, the second harmonic travels at a different phase velocity with respect to the fundamental. Thus, when the second harmonic converts back to the fundamental, the resulting fundamental wave will have a different phase from the original beam had it not undergone the conversion to the second harmonic and back but instead had traveled the same distance.⁵ The resulting phase difference is intensity dependent, and can either add to or decrease the accumulated phase on the original beam.⁵ A type-I frequency conversion crystal can be designed such that the change in phase has the opposite sign of the intensity-dependent B-integral phase that is initially on the fundamental wave. Since both processes are intensity dependent, phase perturbations on the fundamental beam leading to self-focusing can be selectively reduced in regions where B-integral phase is large.

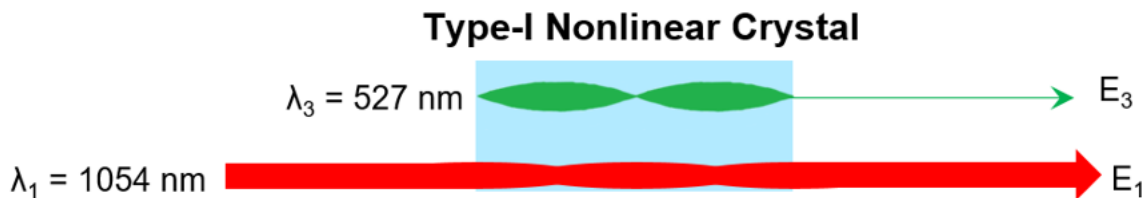


Figure 3: Illustration of the cascaded SHG process in a type-I nonlinear crystal, such as DKDP. The red beam represents the fundamental wave and the green beam represents its second harmonic. E_1 , λ_1 , and E_3 , λ_3 respectively represent the electric field amplitudes and wavelengths of the beams. For non-phase-matched conditions, periodic energy exchange occurs between the two waves, producing an intensity-dependent nonlinear phase shift in the fundamental wave.

The frequency conversion process is governed by the coupled wave equations, Eq. (3) and Eq. (4), that describe the evolution of the fundamental and second harmonic slowly varying electric field amplitudes (E_1 and E_3 , respectively) with propagation distance, z , in the crystal.⁵ In Eqs. (3) and (4), E_1 and E_3 are normalized such that $|E_1|^2$ and $|E_3|^2$ are the respective irradiances of the two waves. The other parameters in these equations and their values used in the DKDP crystal design process are given in Table 1. The first two terms on the right-hand side of Eqs. (3) and (4) represent absorption and the SHG process, respectively. The third term in Eq. (3) accounts for the change in refractive index due to the intensity of the fundamental.

$$\frac{dE_1}{dz} = -\frac{1}{2}\gamma_1 E_1 - i\kappa E_3 E_1^* e^{i\Delta kz} - i \frac{3\omega}{(cn)^2 \epsilon_0} \chi_{eff}^{(3)} |E_1|^2 E_1 \quad (3)$$

$$\frac{dE_3}{dz} = -\frac{1}{2}\gamma_3 E_3 - i\kappa E_1^2 e^{-i\Delta kz} \quad (4)$$

Parameter	Definition	Value ⁶
γ_1	Absorption coefficient of fundamental	0.021 cm ⁻¹
γ_3	Absorption coefficient of second harmonic	0.001 cm ⁻¹
ω	Angular frequency of fundamental	1.7871e15 rad/s
κ	Nonlinear coupling coefficient	9.9512e-06 sec ^{1/2} /J ^{1/2}
$\chi_{eff}^{(3)}$	Third-order optical susceptibility of fundamental	3e-23 m ² /V ²
Δk	Phase mismatch between fundamental and second harmonic	256.76 m ⁻¹
ϵ_0	Permittivity of free space	8.8541e-12 F/m
c	Speed of light in vacuum	2.9979e8 m/s
n	Refractive index of fundamental	1.4935

Table 1: Definitions of parameters in Eqs. (3) and (4) and their values used in the DKDP crystal design process. Values of Δk and κ are those for angular detuning of 0.55 mrad from the phase matched angle. The fundamental angular frequency shown corresponds to the wavelength of 1054 nm. The value for γ_1 was calculated using a weighted average for KDP and 99% deuterated KDP, assuming the typical value of 70% deuteration level for the crystal size and cut required.

In Eqs. (3) and (4), the phase mismatch between fundamental and second harmonic (Δk) can be expressed as,

$$\Delta k = 2 * k_1 - k_3 \quad (5)$$

where k_1 and k_3 are the wave numbers of the fundamental and the second harmonic, respectively. Since,

$$k = \frac{n*\omega}{c} \quad (6)$$

where n is the refractive index, ω is the angular frequency, and c is the speed of light, Eq. (5) can be expressed as,

$$\Delta k = 2 * \frac{n_1 * \omega_1}{c} - \frac{n_3 * 2 * \omega_1}{c} = \frac{2 * \omega_1}{c} * (n_1 - n_3) \quad (7)$$

where n_1 and n_3 are the refractive indices of the fundamental and second harmonic, respectively. Since this is type-I frequency conversion, E_1 is an ordinary wave whereas E_3 is an extraordinary wave. This means that as the detuning angle changes, n_1 does not change while n_3 does. Thus, in this setup, Δk is proportional to the detuning angle. This means that by changing the detuning angle the rate of energy transfer between the waves and their relative phases can be changed.

A frequency conversion model was developed using Eqs. (3) and (4), and used as a subroutine in an OMEGA EP beamline model² to test different crystal configurations, as discussed in Sections 5 and 6. The subroutine works by modeling all points across the laser beam as it travels through the frequency conversion crystal and by assuming the pulse is flat in time of width 1.2 ns. This pulse width is approximately equal to the width of the pre-compressed pulse in the OMEGA EP beamline, described in Section 6.

5. Design Considerations and Methodology

When designing a crystal to compensate for the self-focusing effects on OMEGA EP, one must consider the limited commercial availability of sufficiently large aperture nonlinear crystals that would accommodate the OMEGA EP beam size of approximately 36 cm x 36 cm. The only suitable crystals available at this size are the KDP family of single crystals grown from aqueous solution of component salts. Thus, principal design considerations were crystal length (L) and detuning angle for the expected intensity level in the OMEGA EP beamline. Fig. 4 shows (a) the beam intensity and (b) the nonlinear phase for four different detuning angles as the beam goes through the crystal. The four different detuning angles and their corresponding values of dkL (the product of Δk , given by Eq. (5), and the crystal length), are shown in the key. As seen in Fig. 4, the detuning angle and crystal length are coupled such that only discrete crystal lengths provide maximum fundamental wave throughput for a given input intensity and amount of detuning. In addition, a trade-off exists among the choices of crystal length, detuning angle, and amount of compensating phase. Since maximum fundamental throughput is required, only crystal lengths very close to the peaks of the different intensity curves in Fig. 4(a) can be selected. For example, the red dashed line in Fig. 4(a) is drawn at the peak of the curve for a

detuning of 0.55 mrad (the “moderate detuning” in Fig. 4), so the corresponding crystal length of 44 mm can be considered. With this choice of crystal length and detuning, Fig. 4(b) indicates that approximately -0.12π radians of accumulated phase can be achieved. In order to reduce crystal fabrication costs and sensitivity to alignment in the laser system, it is desirable to have crystal lengths within the range of approximately 10 mm – 45 mm. In Fig. 4(a), as the detuning angle increases, more crystal lengths within the 10 mm – 45 mm range offer maximum transmission, but Fig. 4(b) shows that the accumulated nonlinear phase is correspondingly smaller. Thus, a detuning angle of 0.55 mrad was selected, which allowed for sufficient phase compensation while also providing the choice of reasonable crystal lengths (22 – 24 mm and 43 – 45 mm). It is important to note that Fig. 4 is derived using a single beam intensity while OMEGA EP’s beams have intensity variations. Thus, while the crystal lengths that correspond to maximum transmission in Fig. 4 are good starting points, they may vary slightly from the optimal solution for OMEGA EP. To show the locations of maximum energy transmission clearly, the plots in Fig. 4 do not take the absorption of the crystal into account. However, DKDP was selected due to its lower absorption coefficient compared to other KDP family crystal choices.

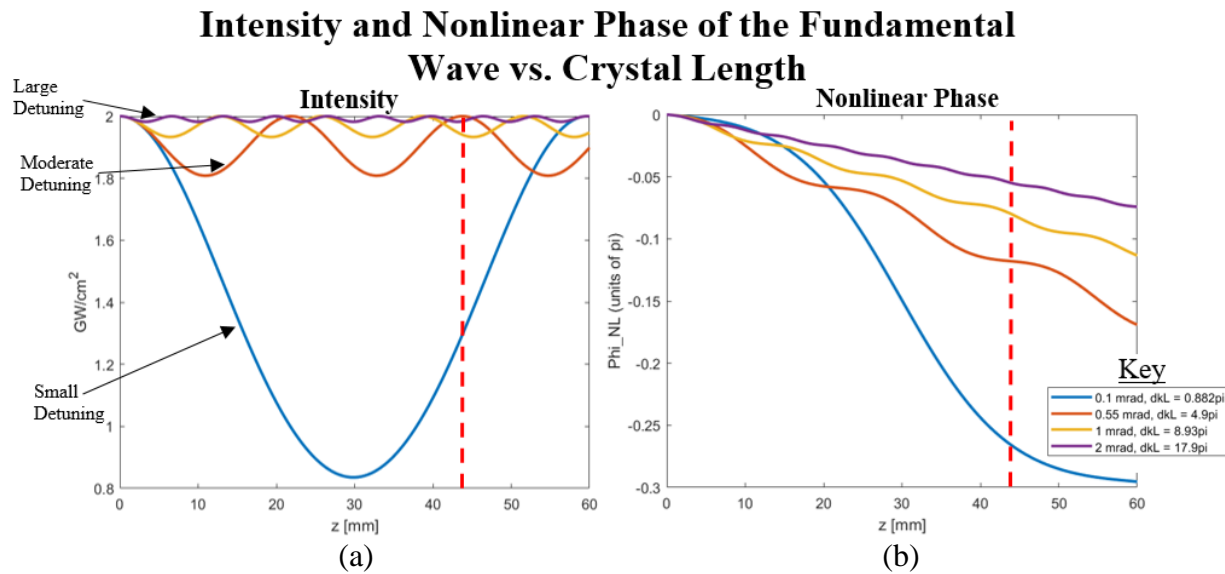


Figure 4: Plots of (a) output intensity and (b) the accumulated nonlinear phase of the fundamental wave vs. the length of DKDP crystal. These plots were made using Eqs. (3) and (4), but without the absorption term to illustrate the primary considerations in the design optimization process. For maximum output energy in the fundamental wave, a trade-off exists among crystal length, tilt angle, and nonlinear phase. The vertical dashed line identifies one design solution that requires a crystal length of 44 mm and tilt angle of 0.55 mrad to achieve approximately 0.12π radians of nonlinear phase. Input intensity to the crystal used in these plots is 2 GW/cm^2 , and is close to the maximum beamline intensity after the last path through the booster amplifiers (see Fig. 5).

The amount of phase compensation that is necessary to compensate the B-integral phase is dependent on the location of the crystal in the beam's path. The localized "lenslets" across the beam, produced by the B-integral phase, vary in size. The amount of phase compensation must match the amount and local size of the B-integral regions for the compensation to be effective. Early in the beam's path the lenslets are essentially non-existent because, at this point, the laser beam has very little B-integral phase. As the beam propagates, the intensity modulations and lenslets change in size and the overall intensity gets higher. To account for this, locations early and late in the beam's path were investigated.

6. Proposed Design Solution

The OMEGA EP short-pulse beams are generated through two of its four beamlines. A schematic of the portion of one beamline relevant to this investigation is shown in Fig. 5, illustrating the major optical components, the laser beam's path, and the three crystal locations investigated. The laser pulse is injected into the beamline from a separate laser source location toward the 7-disk booster amplifier and the 11-disk main cavity amplifier, where it sees significant amplification of its energy. After making four passes through the main cavity, the laser pulse is switched out of the main cavity, making a second pass through the booster amplifier. The laser pulse then propagates through several optical components on its way to the target, including a grating pulse compressor and off-axis parabola focusing mirror (not shown in Fig. 5) that respectively compress the laser pulse in time and focus it onto the target.

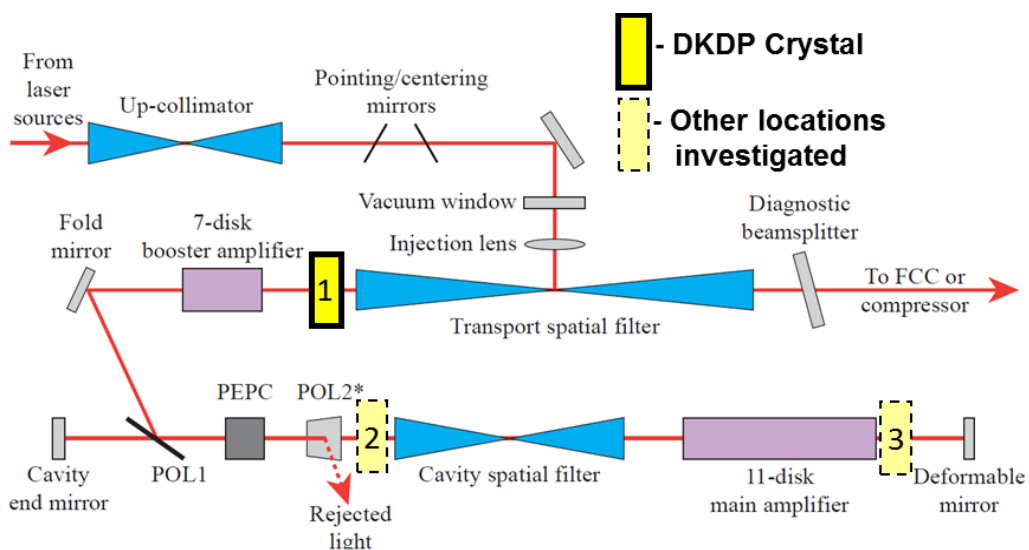


Figure 5: Schematic of the OMEGA EP beamline showing the three locations for the DKDP crystal that were investigated (also see Table 2).

Table 2 provides a summary of why the three locations shown in Fig. 5 were chosen for investigation. The more times the beam passes through the crystal the more opportunities there are for the crystal to impart phase, and the higher the intensity on each pass the more compensating phase is imparted. However, there is a trade-off between the number of times the beam passes through the crystal and the beam's intensity. This is because the beam passes through the crystal four times at locations 2 and 3, as opposed to 2 times at location 1, but the beam reaches its highest intensity just before its last pass of location 1.

Location	Description	Motivation
1	Between the transport spatial filter and booster amplifiers	<ul style="list-style-type: none"> Higher intensity in a single pass than locations 2 and 3 owing to final pass through booster amplifiers
2	Between polarizer 2 (POL2) and the cavity spatial filter	<ul style="list-style-type: none"> Main cavity allows four passes through crystal, potentially providing greater accumulated nonlinear phase than location 1 Lower single-pass intensity than location 1, but higher than location 3 on final pass of main cavity
3	Between the main amplifiers and the deformable mirror	<ul style="list-style-type: none"> Main cavity allows four passes through crystal Close to image plane located at the deformable mirror* Beam's intensity is higher during its first and third pass of the crystal but lower during the second and fourth compared to location 2.

Table 2: Different locations tested for placement of DKDP crystal nonlinear phase compensator in the OMEGA EP beamline and motivation for each choice. Location 1 provided the greatest amount of compensating phase because of the high input intensity to the crystal on the beam's final pass, and produced the greatest reduction in downstream self-focusing among the three locations investigated, as described in the text.
*In general, beam modulation gets worse as the beam gets farther away from an image plane. Thus, by placing the crystal near an image plane, the relative contribution of imaging to the phase compensation can be investigated.

Plots similar to those shown in Fig. 4 were used to choose possible crystal lengths and angular detunings. For each choice of crystal length, detuning, and crystal location in the beamline, the OMEGA EP system model² was used to calculate the beam's intensity modulation at several locations along the beam path. Through this process, a 4.5-cm DKDP crystal at location 1 in Fig. 5, detuned by 0.55 mrad, was determined to achieve the greatest phase compensation while also minimizing residual second harmonic light.

Fig. 6 shows the beam's peak-to-mode value and its maximum intensity for the beam's final pass through the beamline, where the vertical red line in the figure represents the location where the beam makes its second pass through the compensator. Without the crystal, the on-target energy was 2520 J. To compensate for the absorption of energy by the crystal, the input energy to the beamline was increased when the crystal was inserted into the beamline to produce

comparable on-target energy of 2510 J. This higher injected energy is apparent in the beam's higher maximum intensity before the second pass through the crystal (left of the vertical red line in Fig. 6(b)). After passing through the crystal, however, Fig. 6 shows that both the beam's peak-to-mode modulation and maximum intensity are significantly reduced at all subsequent beamline locations (right of vertical red line in Fig. 6). Maximum intensity in the beam is reduced at components most susceptible to laser damage, which include the fourth grating of the grating pulse compressor and those components downstream of this grating (UC G4 and components to the right of UC G4 in Fig. 6). The higher intensity in the region of the beamline to the left of the vertical red line in Fig. 6 when the crystal is inserted is well below the damage threshold for these optical components.

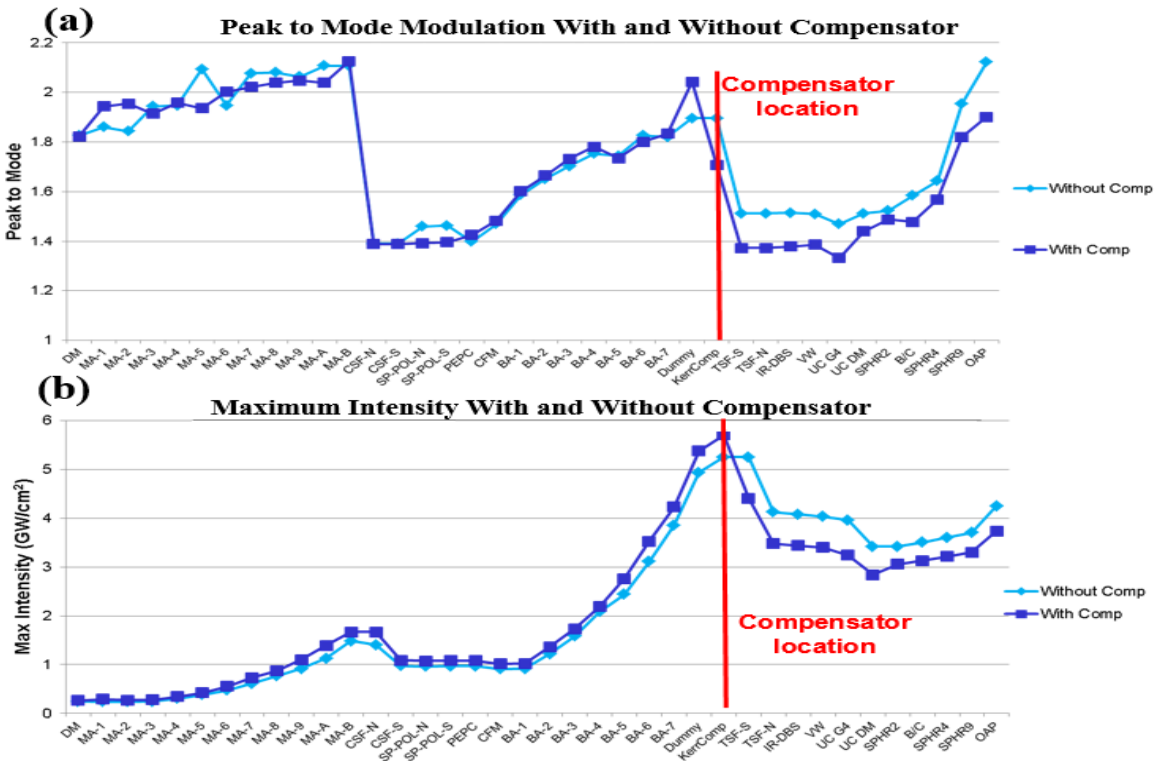


Figure 6: Plots of (a) peak-to-mode and (b) maximum intensity of the beam at the output of successive beamline components for the last pass through the beamline starting at the deformable mirror, with and without the crystal compensator. The beam's path is from the left to the right in the plots. The red line indicates the location of the compensator (location 1 in Fig. 5). Components most susceptible to laser damage include UC G4 and those to the right of UC G4 in the plots. DM – deformable mirror, MA-1 through MA-B – 11 disks of main amplifiers, CSF-N and CSF-S – ends of cavity spatial filter, SP-POL-N and SP-POL-S – ends of short-pulse polarizer, PEPC – plasma-electrode Pockels cell, CFM – cavity fold mirror, BA-1 through BA-7 – 7 disks of booster amplifiers, Dummy – empty optic inserted to allow OMEGA EP model to continue diffraction of the beam until it reaches the crystal, KerrComp – frequency conversion crystal, TSF-S and TSF-N – ends of transport spatial filter, IR-DBS – diagnostic beam splitter, VW – vacuum window, UC G4 – fourth grating of upper compressor, UC DM – upper compressor deformable mirror, SPHR2 – short pulse high reflector 2, B/C – beam combiner, SPHR4 and SPHR9 – short pulse high reflectors 4 and 9, OAP – off-axis parabola.

The compensating phase generated by the DKDP crystal is shown in Fig. 7 for one case. At the vacuum window (VW in Fig. 6), without phase compensation, the average B-integral phase across the beam was approximately 2.5 radians (Fig. 7(a)). With the phase compensation crystal, the average phase at the vacuum window was reduced to approximately 1.8 radians (Fig. 7(b)). This reduction in phase was due to phase of opposite sign from the crystal of approximately -0.7 radians (Fig 7(c)).

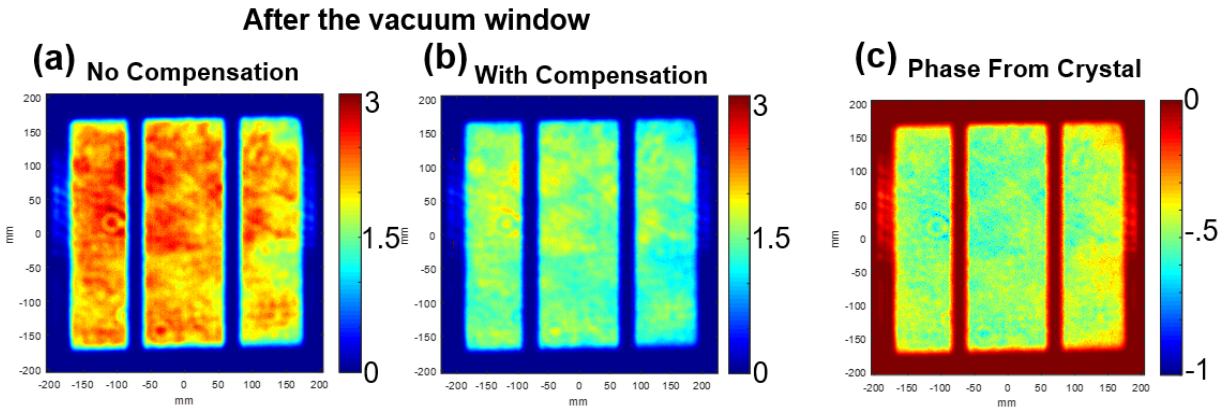


Figure 7: Calculated near-field beam accumulated phase in radians at the vacuum window. (a) B-integral phase without the DKDP crystal compensator; (b) beam phase with the DKDP crystal compensator at location 1. Phase of opposite sign imparted by the crystal is shown in (c). Regions in the beam shown in (a) that have higher B-integral phase also have greater compensating phase in (c).

Shown in Fig. 8 are the near-field images and peak-to-mode (P:M) values of the beam at the compressor vacuum window, the UC G4 grating, and the off-axis parabola with and without the compensator. These key elements are very expensive and difficult to replace, thus damage to them is of great concern when increasing the on-target energy of the beam. In the simulation, there is a significant smoothing effect on the beam when the crystal is inserted into the beamline due to a reduction in the self-focusing effect. This is shown in Fig. 8 by the decrease in the peak-to-mode at these locations by up to 10%, compared to simulations without the crystal.

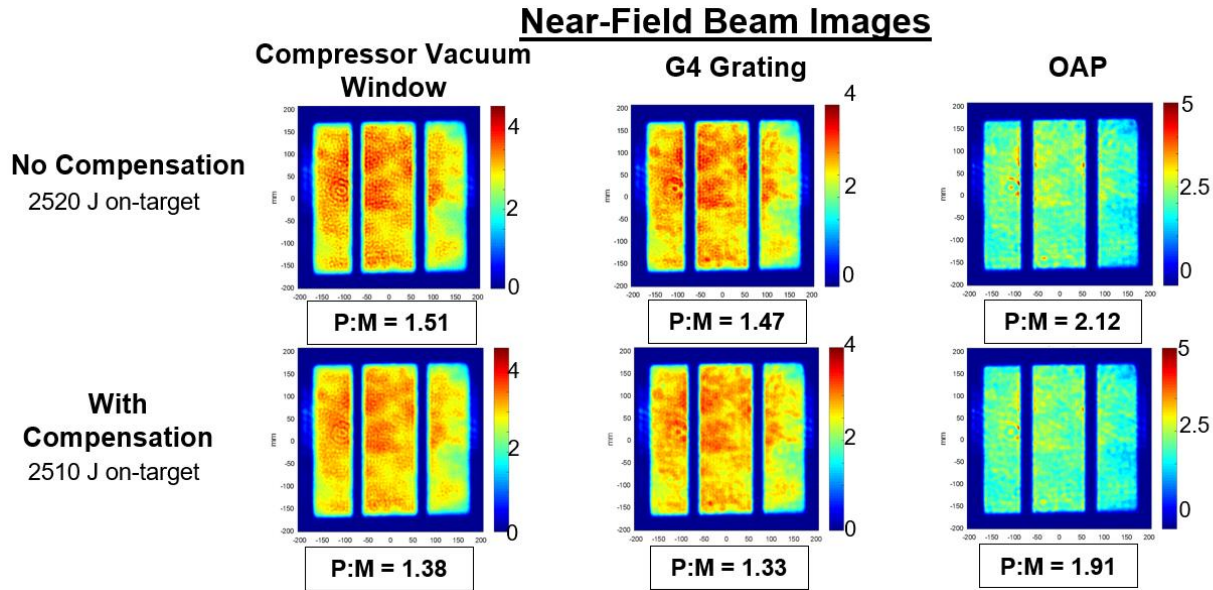


Figure 8: Calculated near-field images of the beam at the compressor vacuum window, the G4 grating, and the off-axis parabola (OAP). The images represent the fluence of the beam which is a measure of energy per unit area and has units of J/cm^2 . Significant smoothing of the beam is seen with the compensating crystal inserted, owing to a reduction in self-focusing.

Since the amount of phase compensation and residual second harmonic conversion is dependent upon the angular detuning of the crystal, the sensitivity of the crystal to angular alignment errors is an important consideration in its design. Other frequency conversion crystals designed for high conversion efficiency in OMEGA EP are routinely maintained at crystal angles to within ± 0.025 mrad of peak conversion, and beam wavefront errors typically have gradients of up to approximately 0.015 mrad. Thus, we investigated the sensitivity of the compensating crystal to comparable changes in the detuning angle, as shown in Fig. 9, where the normalized fundamental wave energy and the peak-to-mode values at the OAP are plotted for a range of detuning angles about the design angle of 0.55 mrad. Within a range of ± 0.05 mrad, the fundamental wave energy varied by only 6%, while the peak-to-mode ranged from 1.85 to 2.00. These relatively small changes suggest that small alignment errors or beam wavefront errors will not be a major impediment to successful deployment of a phase compensator in the laser system.

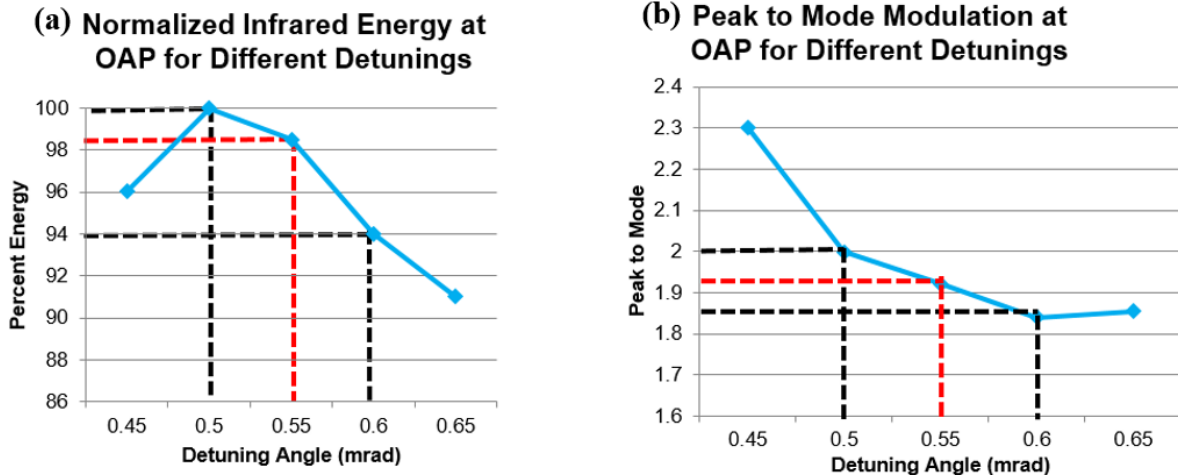


Figure 9: a) Normalized energy and b) beam modulation at the OAP vs. crystal detuning angle showing the sensitivity of the crystal to angular alignment and beam wavefront errors. The red dashed line shows the design 0.55 mrad while the black dashed lines show the bounds of the ± 0.05 mrad range.

7. Conclusion

In this work we explored the use of a frequency conversion crystal to compensate for self-focusing on 100-ps laser shots in OMEGA EP. A MATLAB frequency conversion model was used to design a crystal whose effective nonlinear response partially compensates for the self-focusing effects of the beam. This model was incorporated into an OMEGA EP system model² to simulate the effects of frequency conversion crystals within the OMEGA EP beam path. Based on these simulations, it was determined that a 4.5-cm DKDP crystal, detuned by 0.55 mrad and placed between the booster amplifiers and transport spatial filter, achieved the best results. With the crystal inserted into the beamline, the beam modulation was reduced by approximately 10% at optical components most susceptible to laser damage. These results suggest that it may be possible to increase the on-target energy on the short-pulse beamlines of OMEGA EP from 2300 J to close to the design energy (2600 J) for 100-ps shots with the use of a DKDP compensator.

8. Acknowledgements

I would like to thank my advisor, Mark Guardalben, for all his advice, time, and help. I would also like to thank Dr. R. Stephen Craxton and the Laboratory for Laser Energetics for giving me this wonderful opportunity to spend my summer doing research and Dr. B. Kruschwitz

for creating the OMEGA EP beamline model into which I incorporated my frequency conversion model.

References

1. University of Rochester - Laboratory for Laser Energetics - OMEGA EP, www.ile.rochester.edu/omega_facility/omega_ep/.
2. MATLAB OMEGA EP SP model provided courtesy of Dr. Brian Kruschwitz.
3. Beckwitt, Kale, et al. "Compensation for Self-Focusing by Use of Cascade Quadratic Nonlinearity." *Optics Letters*, vol. 26, no. 21, pp. 1696–1698, 2001.
4. Roth, Ulrich, et al. "Compensation of Nonlinear Self-Focusing in High-Power Lasers." *IEEE Journal of Quantum Electronics*, vol. 36, no. 6, pp. 687–691, 2000.
5. Stegeman, George I. "Cascading: Nonlinear Phase Shifts." *Quantum and Semiclassical Optics: Journal of the European Optical Society Part B*, vol. 9, no. 2, pp. 139–153, 1997.
6. Values for γ_1 and γ_3 from Dimitriev, Valentin G., et al. "Handbook of Nonlinear Optical Crystals". Springer. 1999.
Value for $\chi_{eff}^{(3)}$ is estimated from Ganeev, R. A. "Characterization of Nonlinear Optical Parameters of KDP, LiNbO₃, and BBO Crystals." *Optics Communications*, vol. 229, pp. 403–412, 2004.

**Characterization and Detection of the Deterioration of Electrical Connectors in a
Flash-lamp System**

Meshach Cornelius

Gates Chili High School

LLE Advisors: Troy Walker and Greg Brent

Laboratory for Laser Energetics

University of Rochester

Summer High School Research Program 2017

Abstract

In the OMEGA and OMEGA EP high-energy pulsed laser systems, high-intensity flash lamps are used to excite the laser glass amplifier medium to increase the energy of laser beams for experiments. This amplification system includes a continuous flow of high-resistance deionized water around the flash lamp. This keeps the lamps cool to decrease required laser-glass cool-down time and maximize the frequency of shot operations. When electrical current travels through the flash-lamp connections, a small amount of metal is displaced into the cooling water which causes the resistance of the cooling water to decrease. The metal components in the flash-lamp connector system undergo degradation over time due to repeated displacement of metal debris. Replacing the damaged connectors after a failure occurs is a costly process. Failures also interrupt laser experiment shot operations. To remedy the problem, the concept of a non-invasive process in detecting the levels of flash-lamp connector deterioration was developed and tested. This involves analyzing changes in the resistance of the water flowing through the flash-lamp cooling system. Both cooling-water and flash-lamp systems at different stages of degradation were tested. It was found that the transient change in water resistance is correlated with the level of deterioration in flash-lamp connectors. The minimum current needed to detect a resistance change was determined. Results from this research will allow for non-invasive detection of deteriorated flash-lamp connectors in the amplification system before failure. Implementation of this technique will decrease the risk of failed laser amplifier operation during a laser shot, thereby increasing the reliability of the amplifier system.

1. Introduction

In the 1990s, the Laboratory for Laser Energetics (LLE) Flash-lamp Test Facility was carrying out life expectancy testing on flash lamps to test the maximum number of shots the lamps could undergo before failure. Investigators observed that deionized water coming from the system momentarily dropped in resistance due to metal displacement from the connectors after each operation. Cleveland et al. provide data that supports this observation [1]. It was suspected that electrical arcing, as seen in Figure 1, caused this metal displacement in the connectors. The research described in

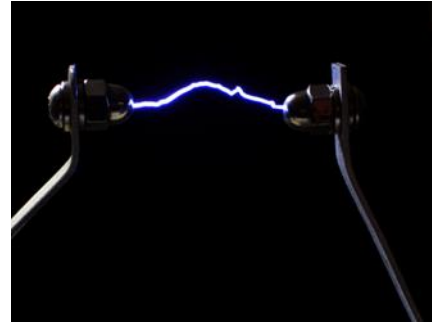


Figure 1: Electrical arcing between two electrodes.

this report aims to create a system to detect transient changes in water resistance and develop a method to characterize the properties of the changes. In turn, this characterization will assist lab operators in determining when maintenance is required on a flash-lamp system before an imminent failure occurs. A lab setup was developed to execute a proof of concept. This setup contained a deionized cooling-water system, a pulse forming network, and the flash-lamp system. Three flash-lamp systems were examined. Each had a different set of connectors. New (never used), slightly used (just burned-in but not worn-out), and used (ready to be replaced) sets of connectors were tested. Figure 2 shows connectors from a new set and a used set in comparison to a failed connector.



Figure 2: Progression of flash-lamp connectors from new, used, to failed.

The amount of metal displacement at different currents was detected via changes in the deionized cooling-water resistance. The amount of metal displaced after a test was found to be correlated to the level of connector degradation. Tests were conducted to measure the minimum amount of current that could yield a detectable change in water resistance. Experiments at different resistances were also conducted. The development of this work will provide a flash-lamp system maintenance indicator to avoid failures caused by end-life flash-lamp connectors.

Connectors were inspected after testing was completed. The connectors in Figure 3 are from a used set of connectors. For this set of connectors, alternate sides of the same connector displayed different degrees of deterioration. Figures 3(a) and 3(b) show opposite views of the connector at one end of a flash lamp. A large difference in the degree of deterioration is clearly seen. Opposite views of the connector at the other end (Figures 3(c) and 3(d)) show the same trend. This is caused by the flash-lamp system sitting horizontally, as has been demonstrated by the flash-

lamp maintenance team at LLE [2]. Varying degrees of deterioration on the same connector side are common on the OMEGA and OMEGA EP lasers at LLE.



Figure 3(a)



Figure 3(b)



Figure 3(c)



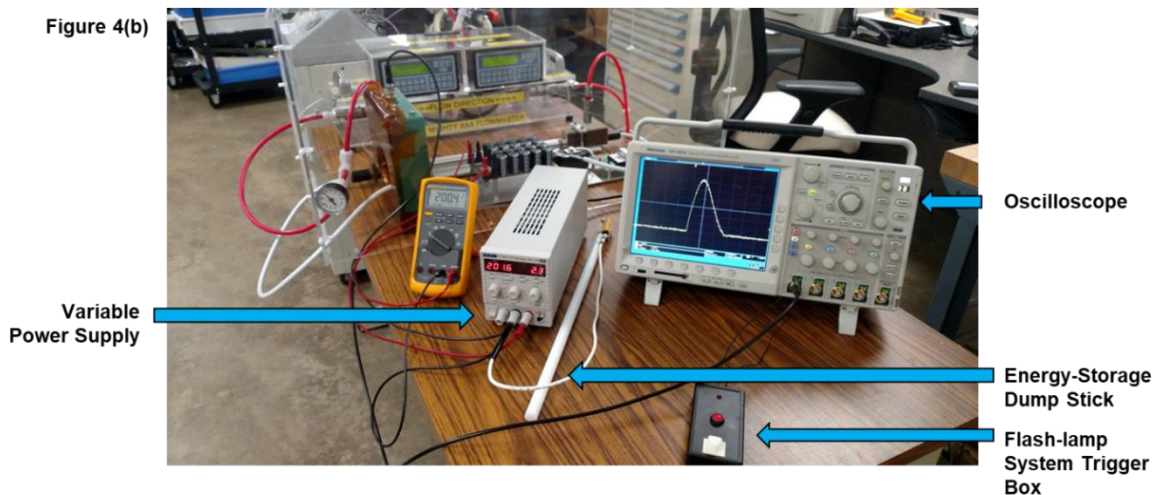
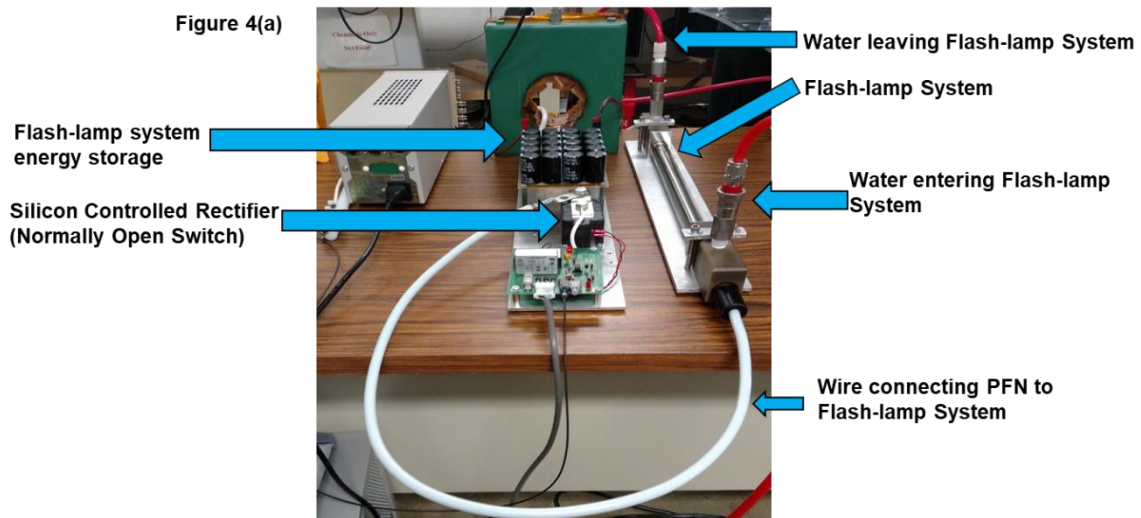
Figure 3(d)

Figure 3: Side comparison of connectors used on the flash-lamp system. Figures 3(a) and 3(b) show the connector at one end of a flash lamp and Figures 3(c) and 3(d) the connector at the other end. Figures (a) and (c) view from the opposite side of (b) and (d).

2. Experimental Setup

Figures 4(a), (b), and (c) show the layout of the experimental setup. Figure 4(a) displays the flash-lamp system energy storage, which powers the flash-lamp system. The silicon-controlled rectifier momentarily allows the energy in the flash-lamp system energy storage to flow through the flash-lamp system. Deionized cooling water and energy from the pulse forming network (PFN) interact with the flash-lamp system. In Figure 4(b), the variable power supply charges the flash-lamp system energy storage. On the oscilloscope, there is a nominal graph of

current with respect to time after a test. The energy-storage dump stick discharges the flash-lamp system energy storage to ensure safe conditions for handling components in the test bed after experiments. The flash-lamp system trigger box connects to the silicon-controlled rectifier. When the trigger box is pressed, the silicon-controlled rectifier allows the flash-lamp system energy to be released. Figure 4(c) shows the connections of the pump to the resistance sensors and flash-lamp system. The resistance sensors measure the resistivity of the cooling water before and after passage through the connectors.



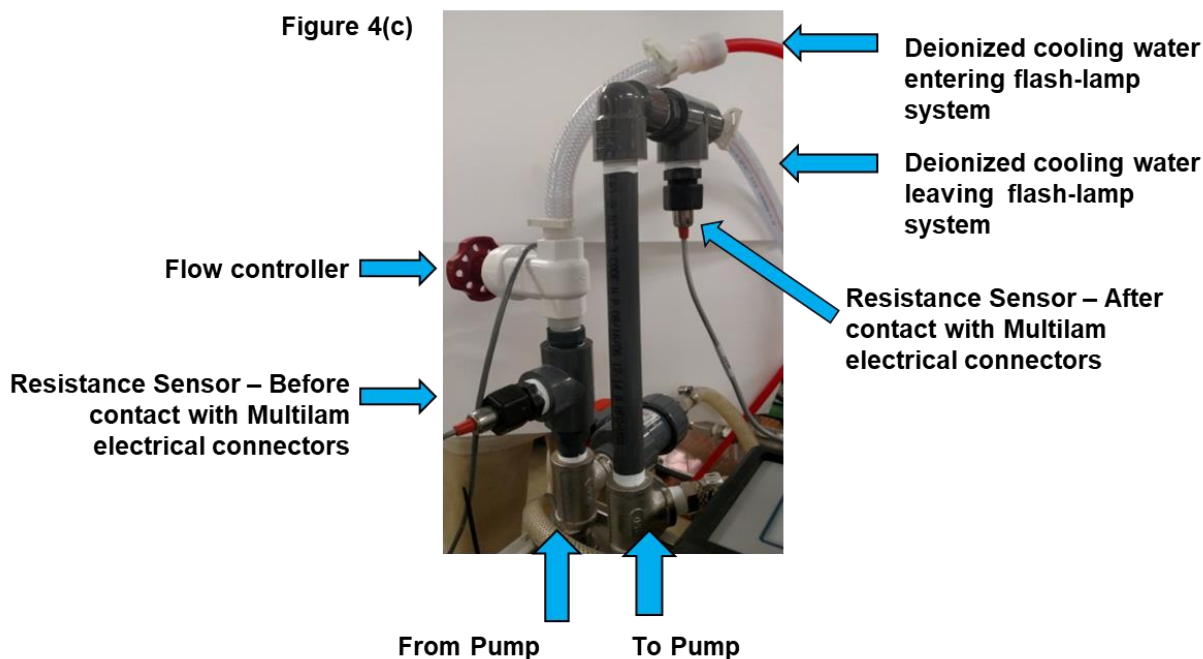


Figure 4: The entire experimental layout. (a) View showing the flash-lamp system. PFN: pulse forming network. (b) View showing auxiliary instruments of the PFN. (c) View showing the resistance sensors.

2.1 Flash-Lamp System

The flash-lamp system contained the connectors that were tested. A modified flash-lamp setup (Fig. 5) was used to optimize the compactness of the proof-of-concept testing. Brick ends, where the connectors are housed, from 52” flash lamps were combined with a metal rod surrogate of 10” arc lamp distance. Figure 5 shows a metal rod used as a surrogate for an arc lamp on the modified setup to decrease the voltage required to reach the standard current simulating OMEGA and OMEGA EP laser flash-lamp operation.

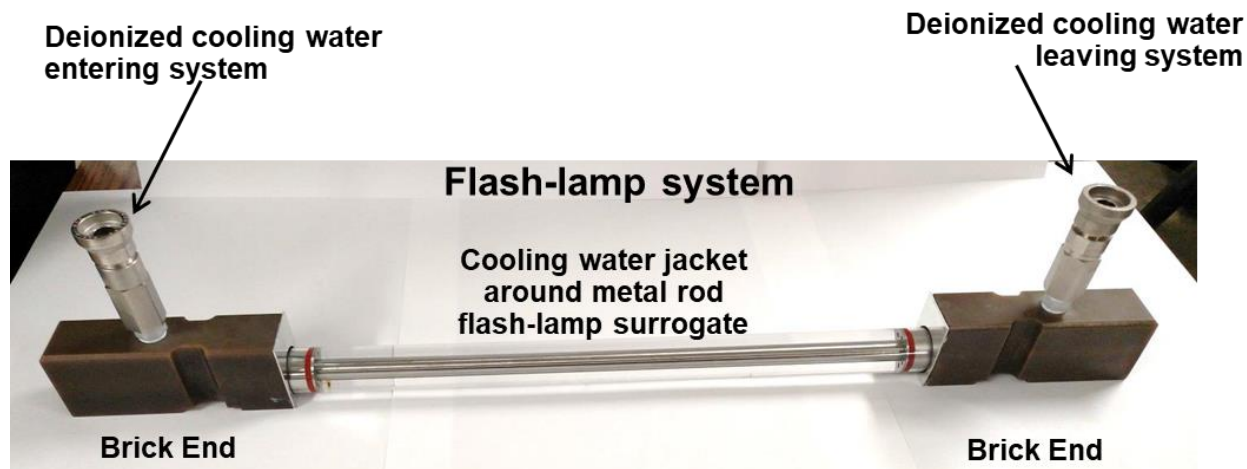


Figure 5: Modified flash-lamp system. The metal rod surrogate is between two brick ends from a 52" flash lamp. The flow of deionized cooling water through the system is shown.

The metal displacement that is captured on the sensors originates from inside the brick ends. The electric arcing that causes this deterioration occurs mainly at connections with Stäubli Multilam contact bands. Figure 6 shows where these Multilam contact band connections are placed on the flash lamp [3].

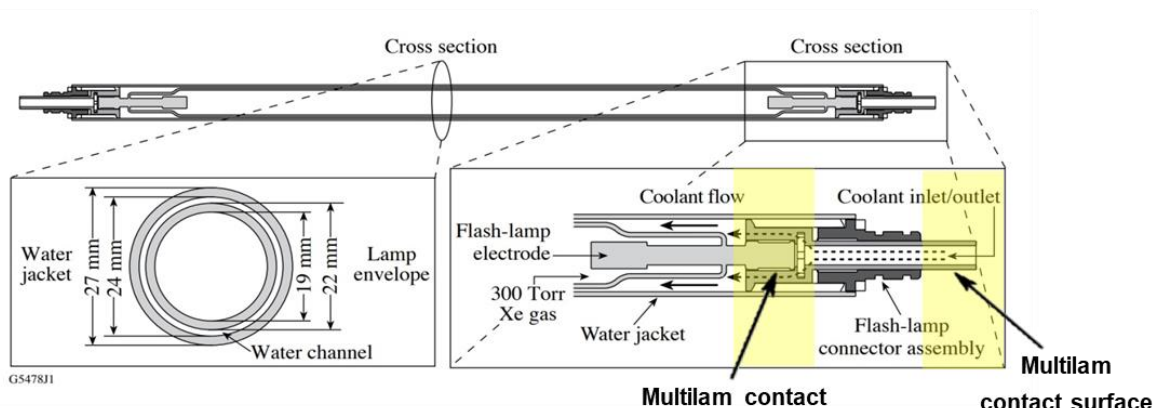


Figure 6: Cross sections of a flash lamp and its connector assembly. Highlighted yellow areas show Multilam contacts where deterioration in the flow of deionized cooling water can occur. Multilam bands are inside the female parts of connections. The male parts at these points, seen in the highlighted areas, incur deterioration.

2.2 Deionized Water System

The setup of the deionized water system is displayed in Figure 7.

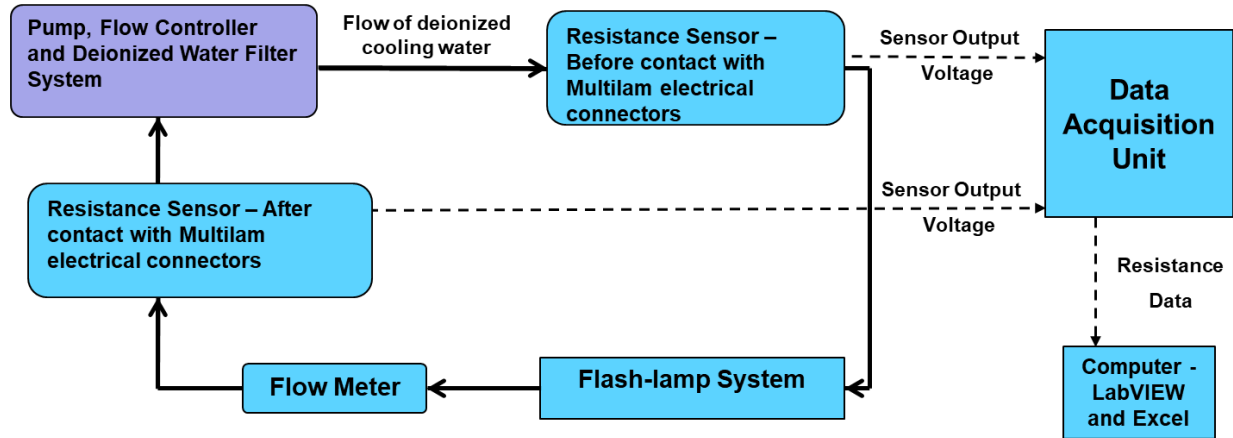


Figure 7: A block diagram of the deionized water system. Black lines indicate the flow of deionized cooling-water. Dashed lines signify the resistance data.

An FTS Systems Maxicool Recirculating Chiller, model # RC-00263-A is used to pump the deionized cooling-water through the system. The deionized cooling-water follows the same path during each experimental procedure. A flow controller is connected in the stream of water to control the velocity of the water. From the pump, the water moves to a resistance sensor. The deionized water goes through the flash-lamp system and acquires metal by the degradation at Multilam connections. The contaminated water then travels through a flow meter and reaches a second resistance sensor. It is sent back into the pump, where the water is purified through the deionized water filter system. The tubing which connected the deionized water system together is 3/8" in diameter. The resistance monitor resolution is approximately 0.02 Megaohms-cm. The average water velocity is 0.5 gal/min as detected by the flow meter. This matches the flow rate used on OMEGA and OMEGA EP. Resistance sensors were used to diagnose contaminated water from connectors. These sensors are easily attachable to the lab setup and are compact for

implementation into OMEGA and OMEGA EP. Myron L CS-10 resistivity sensors were inserted into the flow of water before and after contact with the flash-lamp system. The sensors delivered resistance data to a Myron L 750 Series II resistivity monitor. This data was then converted to a voltage and sent to a data acquisition unit. The acquisition unit data was read by a LabVIEW application. The values were collected in an Excel file, where data reduction could occur.

2.3 Pulse Forming Network (PFN)

The pulse forming network used in this experiment simulated one found on OMEGA or OMEGA EP. A block diagram of the PFN can be seen in Figure 8. The variable power supply controls how much energy is stored in the flash-lamp system energy storage. Once the trigger is pressed on the flash-lamp system trigger box, the silicon-controlled rectifier allows the energy to flow through the flash-lamp system and back to ground. The network had the capacity to reach 7000 A to cover the range of the amplifiers used on OMEGA and OMEGA EP. Twenty 470-microfarad capacitors were used in parallel for energy storage. Capacitors were charged to a set voltage for the experiments. For different tests, the set voltage could be adjusted. The oscilloscope was used to monitor the pulse current on the PFN. Maximum currents ranged up to 6600 Amperes with a current pulse width of 500-600 microseconds.

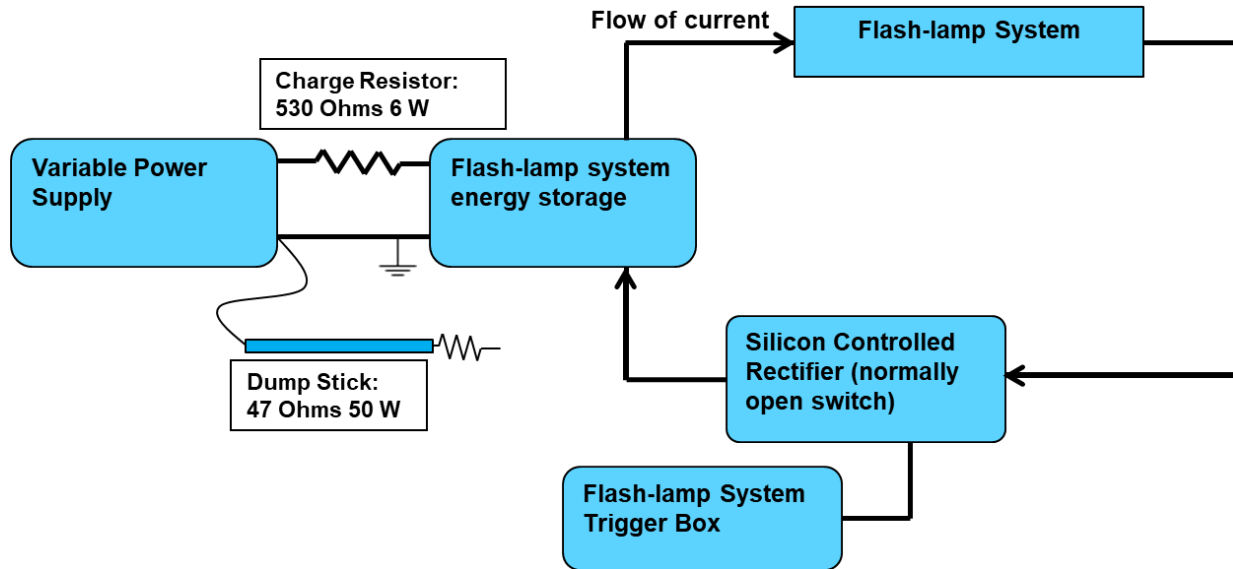


Figure 8: A block diagram of the pulse forming network which supplied current to the flash-lamp system

3. Experimental Data

The test procedure began with a charge of the flash-lamp system energy-storage capacitors. As the energy was stored, a LabVIEW program began recording data on the resistivity of the water. When the appropriate energy storage voltage was reached, the energy was released through the silicon-controlled rectifier into the flash-lamp system. The time of discharge relative to the start of the program's data collection was recorded in the LabVIEW data. This fundamental procedure was repeated for all tests.

Figure 9 shows a typical plot of a new flash-lamp system test. The starting resistance of the transient change of the water resistance was determined by the falling edge of the resistance drop. The time at which this drop occurred was usually between five and eight seconds after the PFN trigger. This matches the expected time the water takes to reach the sensor from the flash-lamp system. Approximately 8 oz of deionized cooling water separates the end of the flash-lamp

system and the resistance sensor after contact with Multilam connections. At a flow rate of 64 oz per 60 sec (0.5 gal/min), the drop theoretically would begin at approximately eight seconds from the pulse.

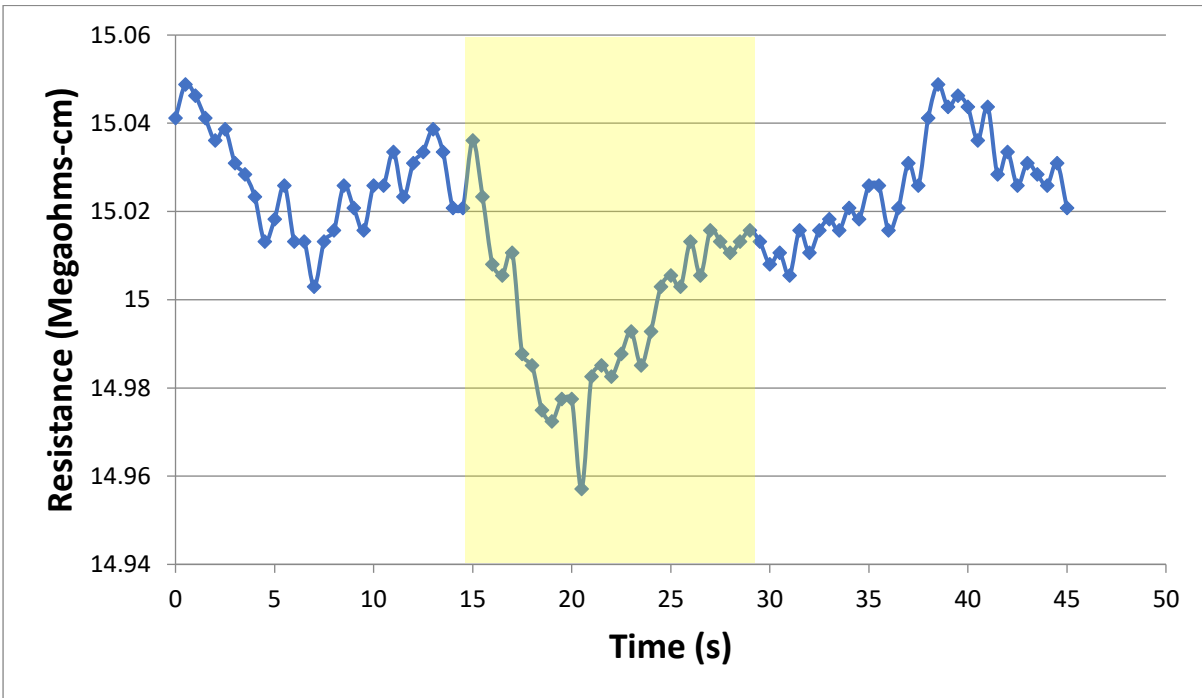


Figure 9: Typical plot of the cooling-water resistance as a function of time during a new flash-lamp system test. The current is 6700 A. The voltage is 210 V. A maximum drop of 0.061 Megaohms-cm was observed ten seconds after the pulse forming network trigger occurred. The yellow area highlights the drop induced by the pulse.

The resolution of the Myron L 750 Series II Resistivity Monitor is approximately 0.02 Megaohms-cm. If the resistance change of the test was within 0.02 Megaohms-cm, the flash-lamp system was deemed to effectively have no change.

Each new connector system test was done with the same flash-lamp system. Table 1 provides data for tests done with the new flash-lamp system. The transient change in water resistance is shown. The average change in resistance for each voltage is shown at the bottom of

the respective column. Table 1 shows that as the peak current of the pulse increased the transient change in water resistivity increased as well.

Table 1: Maximum change in water resistance from the new connector flash-lamp system. Values are in Megaohms-cm.

Capacitor Charge Voltage Peak PFN Current	175 V 5200 A	200 V 6400 A	210 V 6700 A
Shot 1	0.056	0.0433	0.051
Shot 2	0.040	0.079	0.0554
Shot 3	0.043	0.060	0.061
Shot 4		0.0404	0.056
Shot 5		0.054	
Shot 6		0.0458	
Average	0.046	0.053	0.056

The transient changes in water resistance for slightly used flash-lamp system tests are displayed in Table 2. Again, the data shows that as the peak current of the pulse increased the transient change in water resistivity increased. Figure 10 shows a typical plot of a test done on the slightly used flash-lamp system.

Table 2: Maximum change in water resistance from the slightly used connector flash-lamp system. Values are in Megaohms-cm.

Capacitor Charge Voltage Peak PFN Current	175 V 5670 A	200 V 6400 A	210 V 6700 A
Shot 1	0.021	0.021	0.036
Shot 2	0.025	0.028	0.076
Shot 3		0.02	0.058
Shot 4			0.025
Average	0.023	0.023	0.049

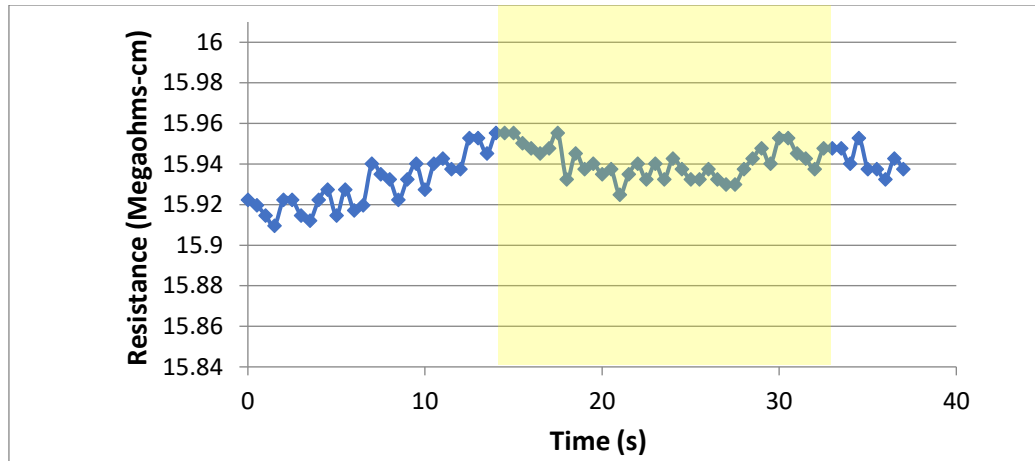


Figure 10: Typical plot of slightly used flash-lamp system test. The current is 5670 A. The voltage is 175 V. The graph illustrates a small change in resistance of approximately 0.02 Megaohms-cm. The pulse forming network trigger occurred at ten seconds. The yellow area highlights the drop induced by the pulse.

Used flash-lamp system data is shown in Table 3. The transient change in water resistance is listed. Figure 11 shows a typical plot of a used connectors test.

Table 3: Maximum change in water resistance from the used connector flash-lamp system. Values are in Megaohms-cm.			
Capacitor Charge Voltage	175 V	200 V	210 V
Peak PFN Current	5500 A	6300 A	6600 A
Shot 1	0.071	0.059	0.179
Shot 2	0.058	0.114	0.168
Shot 3	0.033	0.059	0.091
Shot 4	0.084	0.048	0.117
Shot 5		0.097	
Shot 6		0.038	
Shot 7		0.051	
Shot 8		0.194	
Average	0.062	0.083	0.139

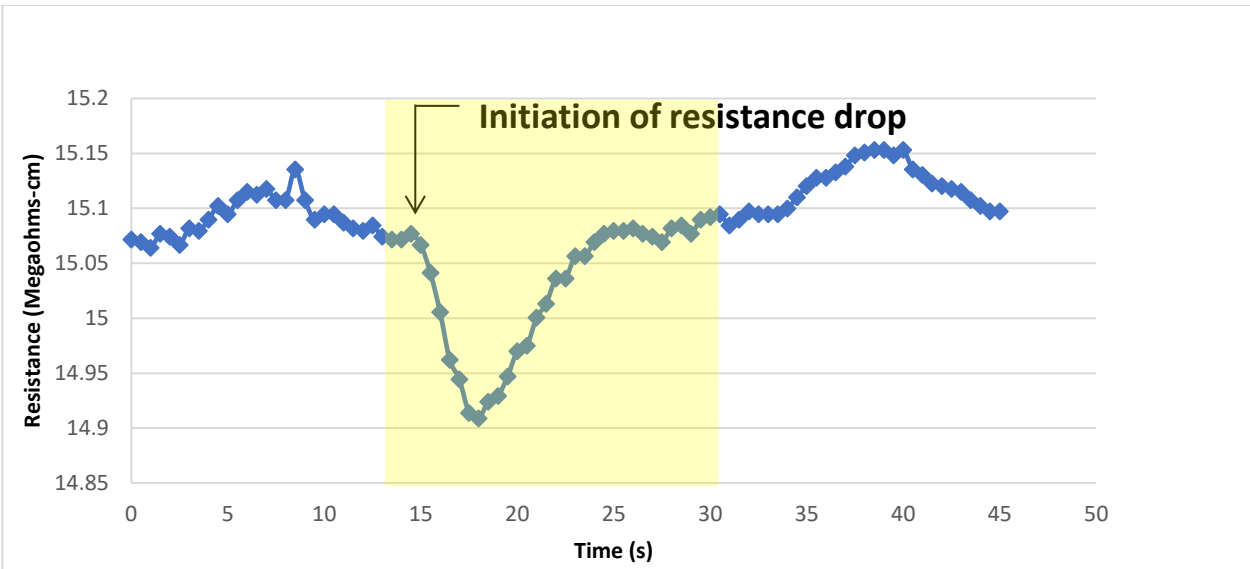


Figure 11: Typical plot of a used flash-lamp system test. The current is 6600 A. The voltage is 210 V. The plot illustrates a drop of approximately 0.16 Megaohms-cm. The pulse forming network trigger occurred at ten seconds. The yellow area highlights the drop induced by the pulse.

At an energy storage voltage of 210 V, the used flash-lamp system produced the greatest average change in water resistance, and therefore the highest amount of metal displacement from its connectors. The new and slightly used flash-lamp systems both exhibited similar magnitudes of water resistance change at 210 V.

Oils and scratches from manufacturing are found on the surface of the new connectors. The process of the male connector seating with the Multilam connections causes metal deterioration. As electricity passes through the slightly used connectors, the connection gets stronger and incurs spots of welding. Over time, this welding and repeated use causes the used connector to deteriorate and large amounts of metal debris release. This explains the counterintuitive observation that the slightly used set of flash-lamp connectors has a lower average change in deionized cooling-water resistance than the new set of flash-lamp connectors.

At all energy storage voltages, the used flash-lamp system produced the highest average change in water resistance, significantly above the other two flash-lamp systems tested.

4. Low Voltage Tests

Tests were conducted to measure the minimum amount of current that could be pulsed into the flash-lamp test system with a detectable change in cooling-water resistance. The minimum current was determined when the change in water resistance dropped consistently at or less than 0.02 Megaohms-cm. Figures 12, 13, and 14 shows tests done at decreasing energy storage voltages, corresponding to decreasing peak current. The change in deionized cooling-water resistance for the slightly used flash-lamp system was below the resistivity monitor threshold of 0.02 Megaohms-cm in a range from 4700 A to 5100 A. The change in deionized cooling-water resistance was below the resistivity monitor threshold for the new and used flash-lamp system in ranges from 4400 A to 4500 A and 4060 A to 4460 A, respectively. The minimum current necessary to release detectable metal particulate was lowest for the used flash-lamp system. This system also produced the highest average change in water resistance. The minimum current range was highest for the slightly used flash-lamp system, which exhibited the lowest average change in water resistance. The minimum energy needed for a flash-lamp system to release metal debris is related to the system's average change in water resistance. As the average change in water resistance and the level of released metal particulate increases, the energy needed to cause a change in water resistance decreases. As the set of flash-lamp connectors increases in deterioration, the amount of debris that is released after a pulse will also increase.

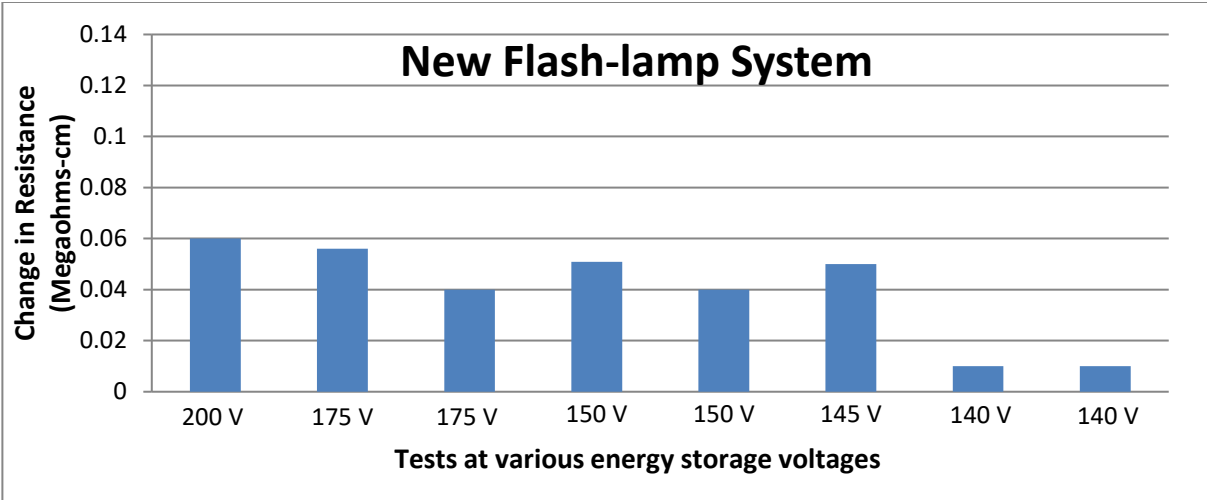


Figure 12: Changes in resistance at decreasing voltages on the new flash-lamp system. The peak current at 140 V was between 4500 A and 4400 A.

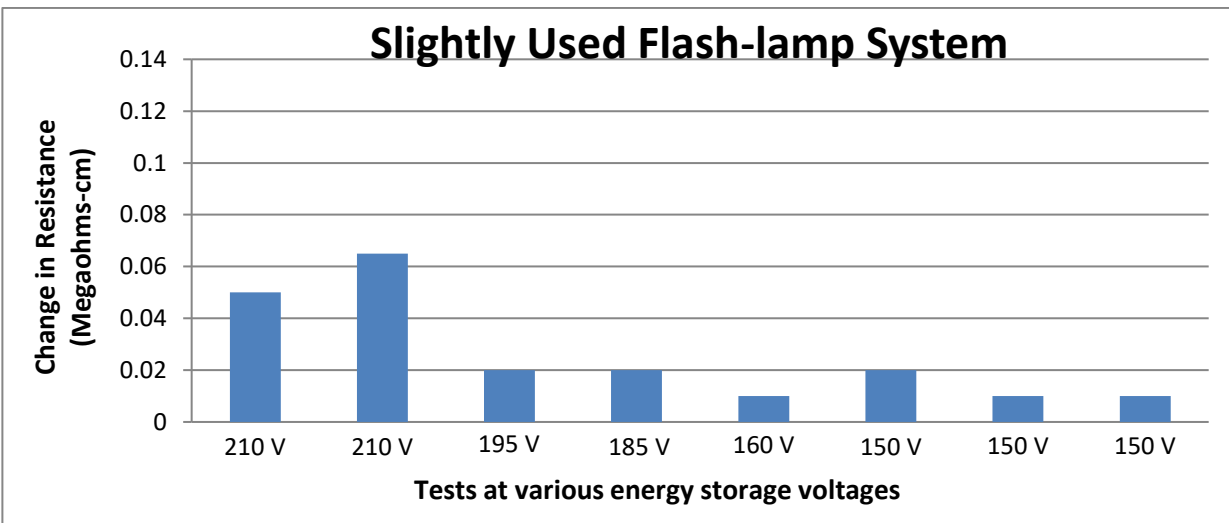


Figure 13: Changes in resistance at decreasing voltages on the slightly used flash-lamp system. The peak currents at 160 V and 150 V were 5100 A and 4700 A, respectively.

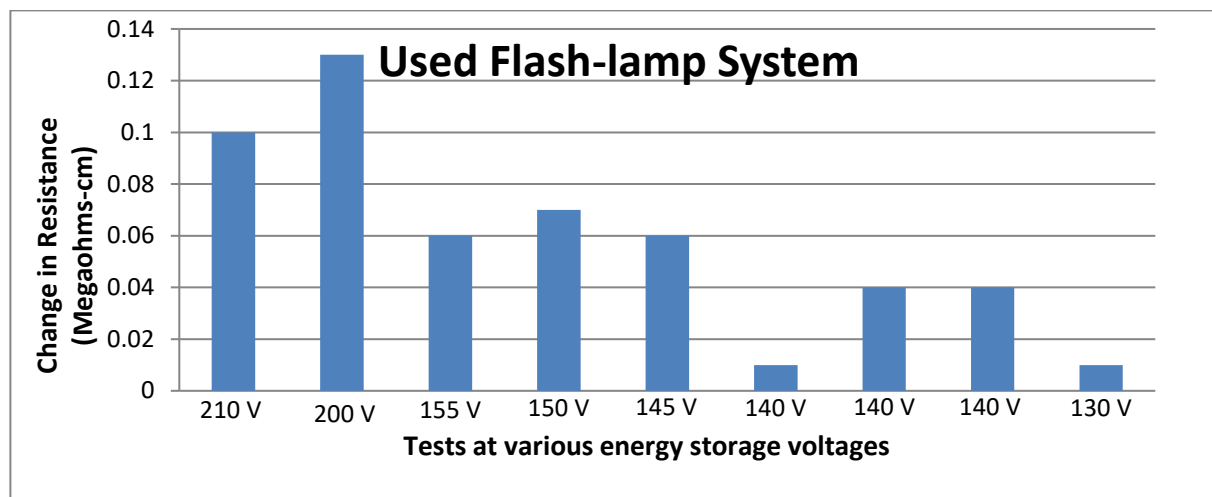


Figure 14: Changes in resistance at decreasing voltages on the used flash-lamp system. The peak currents at 140 V and 130 V were 4460 A and 4060 A, respectively.

5. Low Resistance Testing

Experiments at different deionized cooling-water resistances were conducted. Figure 15 shows these test results. The goal of these tests was to determine if the starting resistance of the cooling water would affect the magnitude and detectability of changes in water resistance. The flow controllers to the water reservoir filters were changed before using the fundamental procedure. This changed the percentage of contaminant which was filtered from the water. This gave control over the starting resistance of the cooling water. Each of these tests was conducted at the same energy storage voltage of 200 V, corresponding to a peak current of 6300 A, with the used flash-lamp system. The initial water resistance was determined by the monitor on the resistance sensor before contact with the flash-lamp system. As the starting resistance went down, the amount of change detected during flash-lamp testing also decreased. Below an initial starting point of 10 Megaohms-cm, the change in water resistance during flash-lamp tests was less than the resistance monitor resolution.

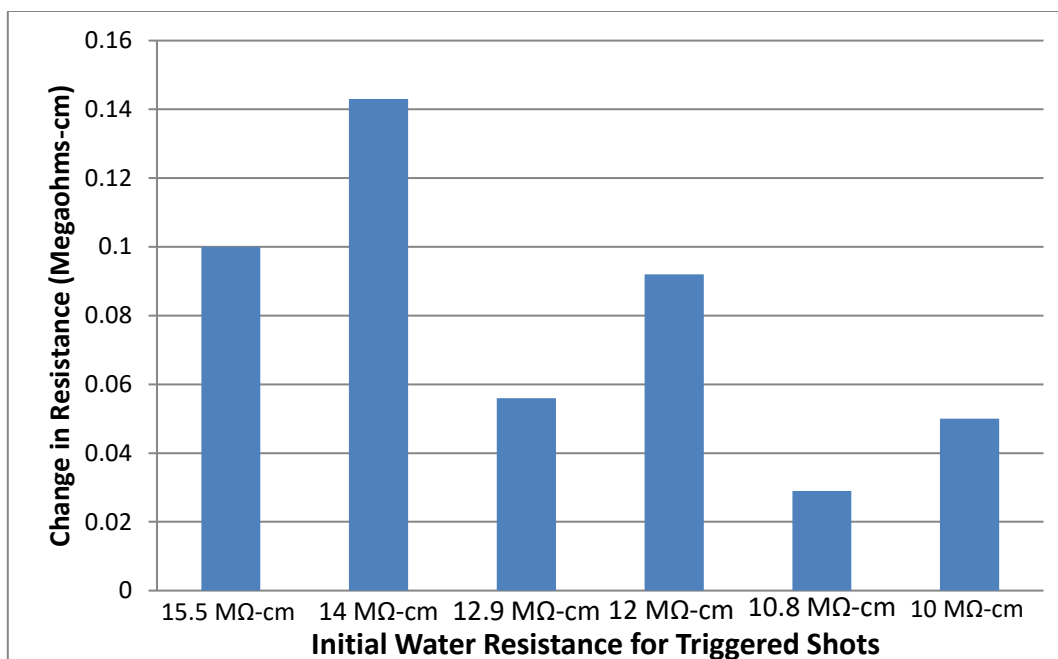


Figure 15: Changes in water resistance at decreasing starting resistances

6. Consecutive Drops

On some of the flash-lamp tests, a secondary drop in water resistance was detected after the first drop produced by a single current pulse. Figure 16 shows an exemplary graph with two consecutive drops in water resistance. This second drop was consistently smaller than the first drop and ranged from 0.07 Megaohms-cm to 0.02 Megaohms-cm in magnitude. The used lamp had the highest average discernible second drop. As the energy storage voltage increased, the frequency of secondary drops above the 0.02 Megaohms-cm benchmark increased. It was theorized that this double drop was produced by displaced metal from the second connector. This theory is supported by the secondary drop coming approximately 16 seconds after the pulse. The inside of the flash-lamp system, where the surrogate metal rod was housed, is 8 oz in volume. 16 oz of deionized cooling water separates the resistance sensor after contact with Multilam bands and the second

connector in the flash-lamp system. At a flow rate of 64 oz per 60 sec, the second drop should arrive at the sensor approximately 16 seconds after the pulse forming network trigger.

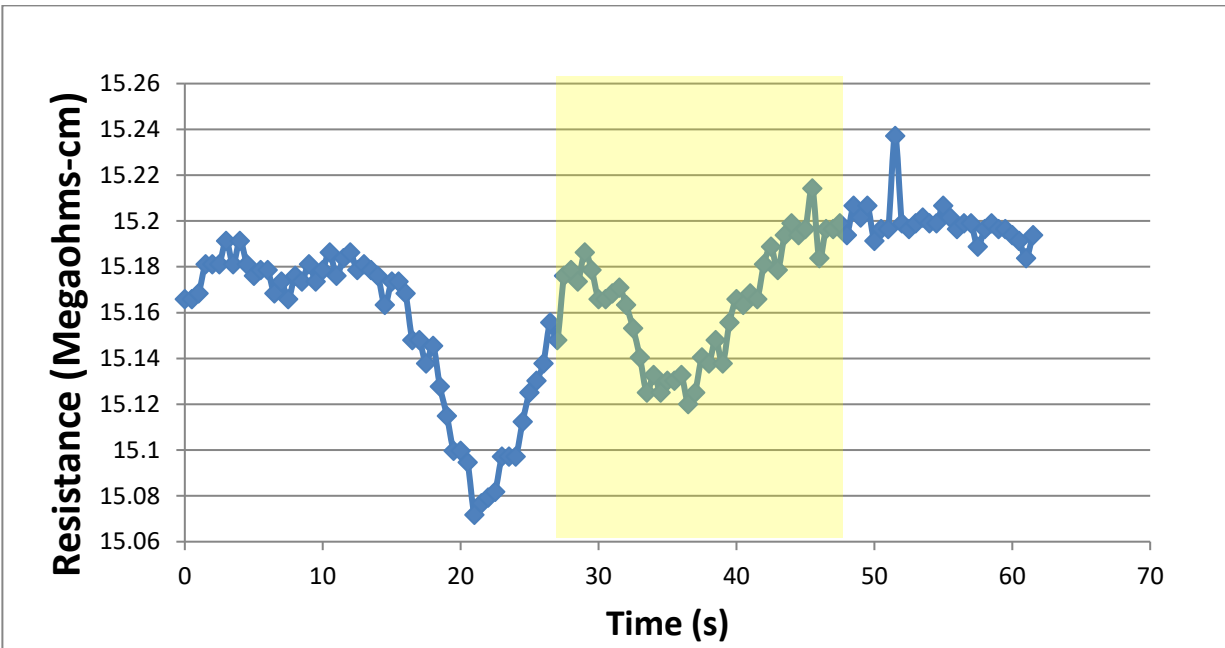


Figure 16: Data from sensor after contact with used flash-lamp system. There is a drop at 15.5 seconds followed by a second drop at 29 seconds. This test was conducted at 200 V. The Pulse Forming Network trigger occurred at ten seconds. The yellow area highlights the second drop induced by the pulse.

A possible explanation for the inconsistency of the appearance of the second drop under very similar conditions to Fig. 11 is that the released flash-lamp connector particulate varies in size. When relatively large particulate flows through the system, it requires a longer time for the debris to reach the sensor after contact with Multilam bands. If the amounts of debris for tests are approximately the same, the composition of the debris may be dissimilar. On tests where the flash-lamp connector releases particulate of a larger average size, the drop is longer in time and therefore has a lower magnitude. This explains why some tests, such as Fig. 11, show second drops with a

change in resistance close to or below the resistance monitor threshold, while others, such as Fig. 16, show a change in resistance that exceeds the threshold. For more deteriorated flash-lamp connector sets, the amount of debris is great enough that a drop above 0.02 Megaohms-cm can still be recorded over a longer time. This effect of particulate size is compounded by the second connector because the holes which allow deionized water to enter the flash-lamp reservoir are higher than the base of the flash lamp. This could affect both the characteristics and timing of the second drop. Experiments that involve introducing different particulate of known sizes will help to understand the effect that particulate size has on how the release of flash-lamp connector debris is recorded on the graph.

7. Different Flow Rates

Different flow rates were explored and tested to see if any characteristics of resistance drops changed. With the new flash-lamp system, the flow rate was increased from 0.5 to 0.9 gal/min. Figure 17 shows a data set resulting from this faster flow rate. The flow rate had no effect on the magnitude of the drop. The resistance change did come earlier. At a flow rate of 115 oz per 60 sec (0.9 gal/min), the resistance drop should theoretically arrive at approximately four seconds after the trigger is initiated.

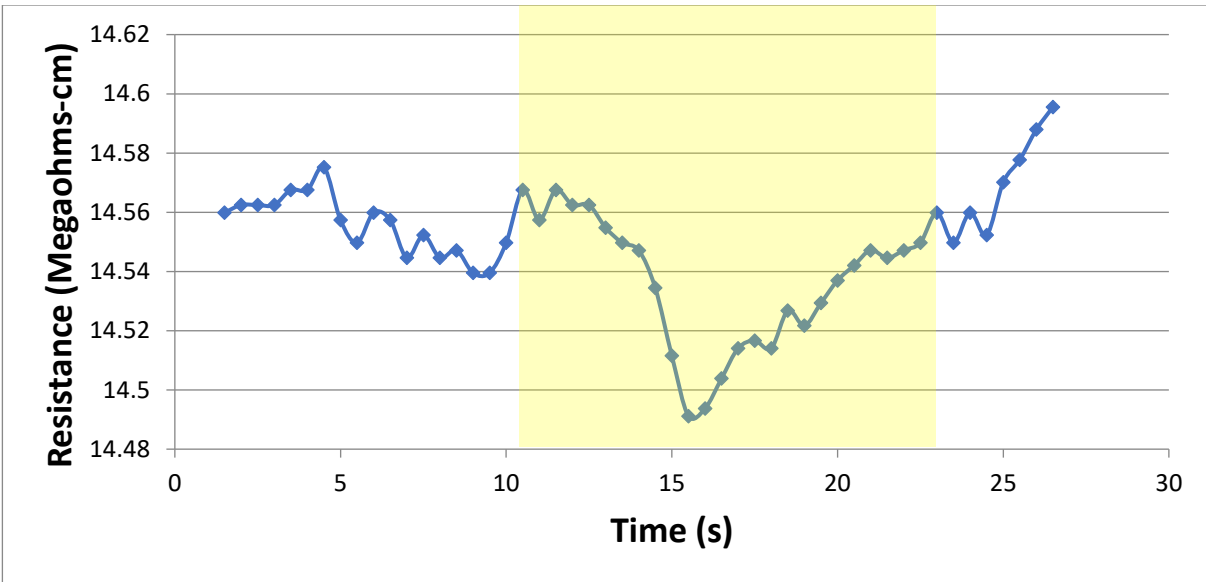


Figure 17: A graph of resistance with a flow rate of 0.9 gal/min. The change occurs at 12.5 seconds. The new flash-lamp system at 200 V was used to conduct this test. The Pulse Forming Network trigger occurred at ten seconds. The yellow area highlights the drop induced by the pulse.

8. Conclusion

Several conclusions can be drawn from these tests. The transient change in water resistance after a release of energy through the flash-lamp system can be reliably measured. As the current that flows through the flash-lamp system increases, the amount of metal displacement that occurs increases, thus the larger the resistance change. The used flash-lamp system consistently delivered the largest change in water resistance at all currents.

As a proposed future application, a surveillance system can be created to alert when the change in resistance after a laser shot exceeds a benchmark level. This will signify that the flash-lamp system, from which the large drop originated, needs to be serviced due to deteriorated

connectors. Preemptive replacement of the flash-lamp connectors will avoid a flash-lamp system connector failure and laser shot failure.

Automation of the test used for this work may allow an insight into how many triggered shots it takes for a new flash-lamp system to produce resistance-change readings comparable to the used flash-lamp system.

The flash lamps on OMEGA and OMEGA EP that amplify the laser are connected in series-parallel. Analysis of flash lamps in series and series-parallel jacket connections is important for implementation into the OMEGA and OMEGA EP lasers.

Further research of the second connector in the flash-lamp system will increase the understanding of the water resistance graphs and increase accuracy in identifying flash-lamp connectors that need replacement.

On the experimental lab setup, debubbling can be tested. The process of removing dissolved gas bubbles in the water can decrease the amount of metal displacement and therefore increase the longevity of the flash-lamp systems. Results of the low resistance tests indicate that a lower resistance of the deionized cooling water negatively affects the accuracy of the change in resistance. For future implementation on OMEGA, the average starting point resistance would have to increase above 11 Megaohms-cm to be effective.

9. Acknowledgements

I would like to acknowledge Dr. Stephen Craxton and the Laboratory for Laser Energetics for giving me the opportunity to do this research. The internship was a fantastic experience. Special

thanks to my advisors, Troy Walker and Greg Brent. They were instrumental in the growth of my knowledge in science and the success of this project.

10. References

[1] C. Cleveland, S. Moghaddam, and M. Orazem, “Nanometer-Scale Corrosion of Copper in De-aerated Deionized Water,” *Journal of the Electrochemical Society*, vol. 161, pp. C107-C114, Dec. 31, 2013.

[2] Mike Scipione, Private Communication

[3] “Chapter 3: Laser Amplifiers,” *OMEGA EP System Operations Manual Volume VII–System Description*, pp. 17, August 2005.

Study of the Hydrogen Palladium System

Griffin Cross

Pittsford Sutherland High School

Advisor: Walter Shmayda

Laboratory for Laser Energetics

University of Rochester

Rochester, NY

June 2018

Abstract

Palladium is a metal which has been found to absorb hydrogen at low temperatures. Releasing the absorbed hydrogen into a closed volume, it is possible to compress the hydrogen and its isotopes to high pressures at modest temperatures. An experimental setup comprising a palladium getter connected to a hydrogen distribution loop was used to measure the hydrogen pressure over palladium hydride as a function of the hydrogen-to-palladium (H/Pd) atom ratio and the palladium-hydride temperature. Equilibrium hydrogen pressures at palladium-hydride temperatures below 293 K are scarce in the open literature. In this study the equilibrium pressures have been measured for H/Pd ratios between 0.0 and 0.8 and temperatures between 123 K and 373 K. This extends the prior minimum temperature of study from 293 K down to 123 K and demonstrates that the H/Pd plateau region extends to 0.8 at the lower temperatures, compared with 0.6 at higher temperatures.

Section 1: Introduction

Prior to this work, published data on hydrogen pressure over palladium-hydride was in the temperature range of 293 K to 1270 K. The hydrogen/metal plateau region in these studies extended for hydrogen-to-palladium (H/Pd) atomic ratios from 0.1-0.6. The plateau region is where the hydrogen pressure does not increase much while the H/Pd ratio is increased, resulting in a relatively flat slope for part of the graph of the pressure vs. H/Pd ratio. Naturally, it is logical to expand the data base of the palladium-hydride system below this temperature range, which would hypothetically correspond to an increase in the range of the hydrogen/metal plateau region. In the known temperature range, a larger percentage of hydrogen atoms bond to palladium at temperatures below 570 K, so it is hypothesized that an even larger percentage of hydrogen atoms will be able to bond to the palladium at temperatures below 293 K.

Section 2: Theory and Motivation

Palladium is one of a special category of metals that can form hydrides. This means that it is able to absorb large quantities of hydrogen gas. Palladium stores hydrogen by breaking the hydrogen molecules into two hydrogen atoms, which then bond to the palladium in three stages. The initial stage is known as the alpha region, shown in figure 1. In this region, hydrogen atoms dissolve in the palladium metal lattice, but are not chemically bonded to the palladium. The second stage is the mixed alpha and beta region, also shown in figure 1. In this region, a fraction of hydrogen atoms is chemically bound to the palladium atoms, while the remainder remain dissolved in the lattice spaces. The third stage is the beta region, where all the possible hydrogen-palladium bonds have been made and any extra hydrogen must dissolve in the metal hydride lattice. The beta region requires much more pressure to insert gas into the structure because the hydrogen is no longer binding to the palladium but just finding space to inhabit within the lattice.

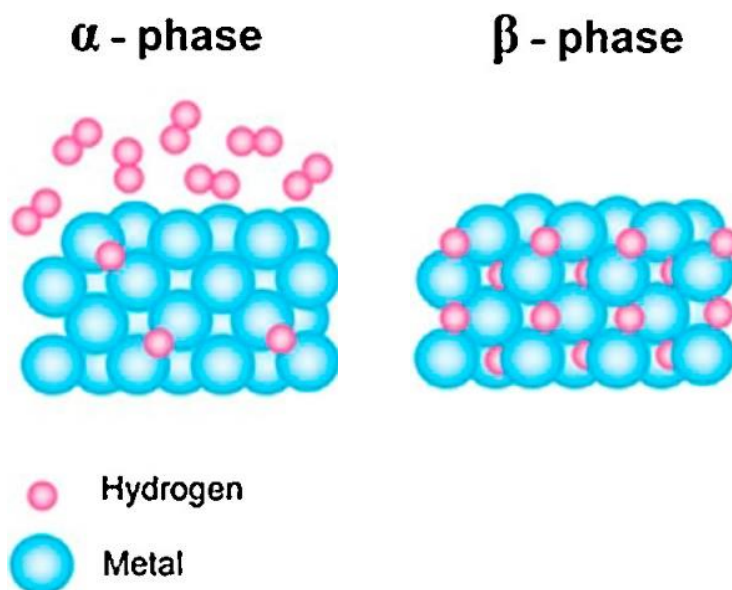


Figure 1: Alpha and beta phases at a molecular level. In the alpha phase, the hydrogen particles are simply occupying the space in between the palladium lattice without bonding to them, resulting in the more disorganized pattern. In the beta phase, the hydrogen atoms are bonded to the palladium atoms which is why the palladium hydride is more structured in the beta phase.

The progression of the three phases is shown graphically in Figure 2.

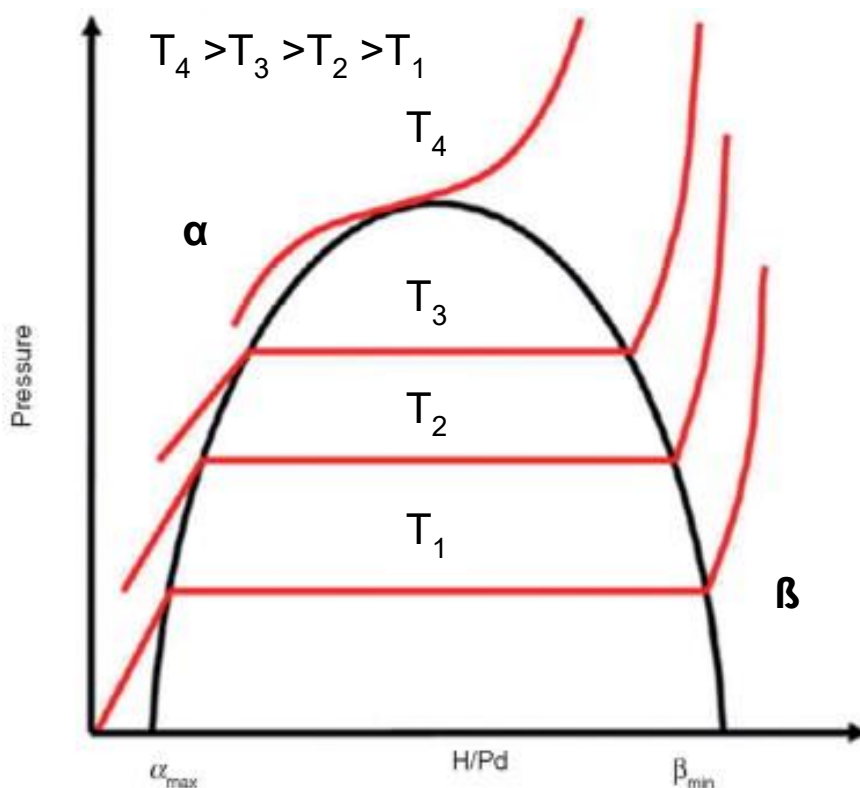


Figure 2: Pressure-temperature-composition curves at increasing temperatures, T_1 - T_4 . The different regions of palladium hydride are represented by regions around the parabola. To the left of the parabola is the alpha region. In the middle of the parabola is the alpha and beta region. To the right of the parabola is the beta region. α -max shows the end of the alpha region, and β -min shows the beginning of the purely beta phase.

As the temperature increases from T_1 to T_4 , the pressure exerted by the hydrogen also increases, which is seen in Figure 1. As the temperature changes, the sizes of the three regions also shift, with the mixed alpha and beta region shrinking as the temperature increases. At the peak of the parabola in Figure 1, the alpha and beta regions coalesce. Extending the trends from the graph to temperatures below T_1 , the hypothesis is that the mixed alpha and beta region will extend from lower H/Pd ratios to larger H/Pd ratios, thereby making it possible to store more hydrogen with less pressure.

The van't Hoff equation (1) applies to the palladium hydride region. This equation provides the relationship between the hydrogen pressure and the temperature of the hydride. This relationship depends on the standard enthalpy change, ΔH , and standard entropy, ΔS for the process. The standard form of the van't Hoff equation is

$$\ln P = \frac{\Delta H}{RT} - \frac{\Delta S}{R} \quad (1)$$

This equation is often simplified to

$$\ln P = \frac{A}{T} + B \quad (2)$$

When plotting $\ln P$ against $1/T$ at a given H/Pd ratio, the relationship is linear. The A value is the slope of the graph and the B value, equal to $-\Delta S/R$, is obtained by solving Equation 1 for a given temperature and pressure. An example of a van't Hoff curve is shown below in figure 3.

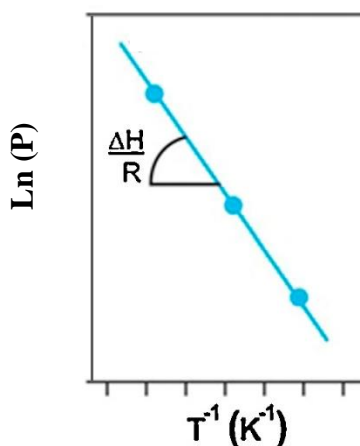


Figure 3: A typical van't Hoff curve, where the y-axis represents the \ln of pressure (in torr) and the x-axis represents $1/\text{temperature}$ (in Kelvin). The slope of the graph is $\Delta H/R$ (which is also known as the A value).

Palladium is being investigated for use as a storage medium and pump for hydrogen and its isotopes, deuterium and tritium. Current pumps are expensive and mechanically complicated, which increases the potential for the release of radioactive tritium. Palladium offers a simpler and more robust alternative. A palladium sponge would allow inertial confinement fusion targets to be filled by alternating the temperature of the palladium, initially cooling the palladium to absorb tritium from a reservoir and then warming the palladium in a controlled manner to pressurize the targets. For this reason, it is important to collect data on the pressure as a function of hydrogen to palladium ratio at sub-zero temperatures. This data is necessary to test if hydrogen can be stored at higher ratios at lower temperatures to optimize the amount of hydrogen that can be stored in a given volume of palladium. The exact data is also significant so that the relation between temperature, time, and hydrogen absorbed/excreted can be known since the targets require a very precise amount of hydrogen, deuterium, or tritium.

Section 3: Experimental System

The experimental system used (shown schematically in figure 4) includes a palladium bed, a calibrated volume, a cryogenic cooler (Q-Drive), a hydrogen supply tank, an MKS pressure gauge, a scroll vacuum pump, a turbo vacuum pump and a series of valves labeled as V_H , V_{Pd} , V_{Vac} , V_{Iso} , V_1 , V_{Cal} , and V_{2nd} . All components are connected by stainless steel pipes and Swagelok fittings. The integrity of the system was measured using a helium leak detector and demonstrated to be less than $1 \cdot 10^{-9}$ scc/sec helium.

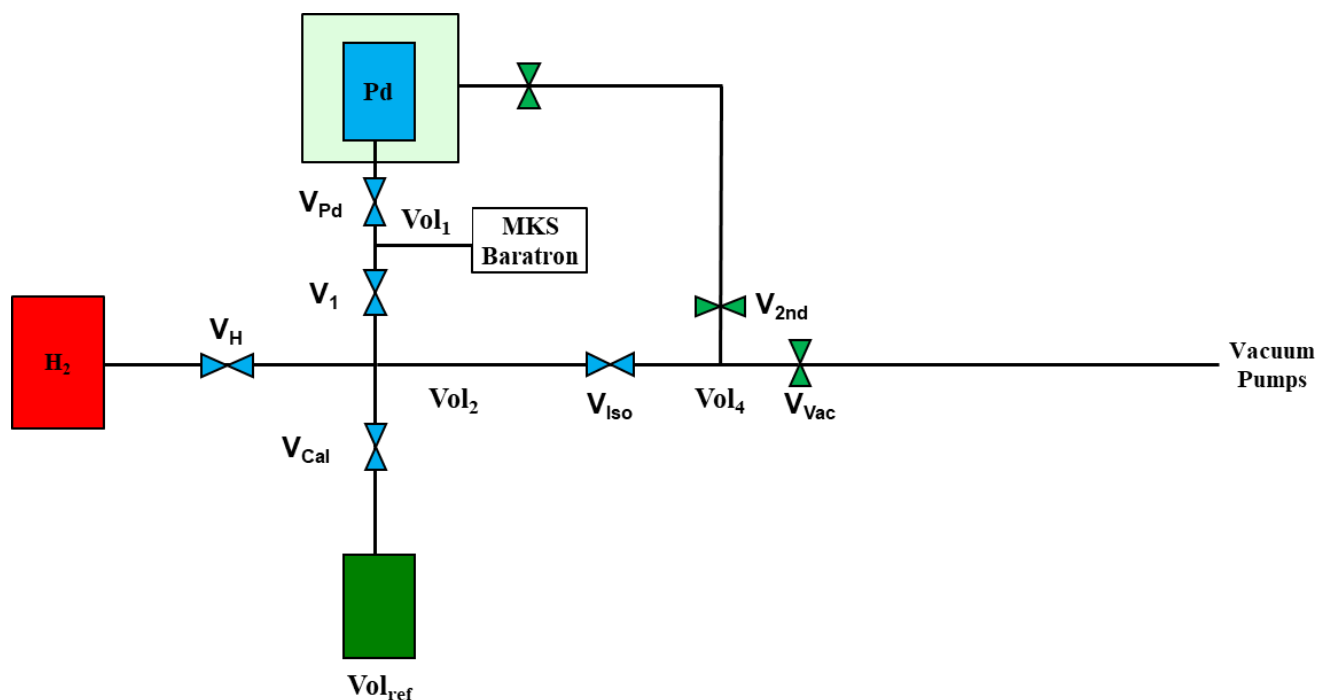


Figure 4: Schematic of the experimental setup used to measure the hydrogen isotherms

As seen in figure 4, the hydrogen tank is on the left, the palladium bed is on the top, the calibrated volume is on the bottom, and the vacuum pumps are off to the right. The blue color, seen on some valves, represents that they are closed. The position of the valves on the schematic drawing are for when the system is finished unloading and is ready for another run. The volumes labeled are the volumes in the pipes connecting the different parts of the system.

Data was collected in individual “runs,” each of which consisted of a loading and unloading procedure. The loading procedure describes the steps used to administer hydrogen from the hydrogen tank to the palladium bed. The hydrogen is transferred in small amounts, called loads.

Before each load was initiated, V_{Cal} , V_{Pd} , V_{H} , and V_{Iso} were closed while $V_{2\text{nd}}$, V_1 , and V_{Vac} were open. V_{Ref} was a calibrated volume only used to find the volume of the other segments, and was not meant to be included as part of the loading process. After all valves were in the correct position, V_{H} was opened extremely cautiously to begin loading. V_{H} was closed after reaching the desired pressure for the load. Gas was allowed to reach equilibrium, then V_1 was closed. Pressure measurements were recorded from the gauge and inserted in an Excel spreadsheet. V_{Pd} was then opened to allow the gas to enter the palladium bed. After about 5 minutes, data was taken from LabVIEW and copied into Excel. This data was used to create graphs of pressure vs time, discussed later. Gas was allowed to reach equilibrium, and then pressure measurements were taken from the gauge again. Data was entered into an Excel spreadsheet which tracks pressure vs. the H/Pd ratio. The loading process was repeated until the pressure vs H/Pd graph approached 1000 Torr in the beta region.

Before beginning the unloading process, $V_{2\text{nd}}$ was closed and the turbomolecular vacuum pump was turned off so that it does not get damaged when unloading the palladium bed. The Pd bed was heated in increments of 20 °C, with gas being let out of the Pd bed every 20 °C. Gas was released by first closing V_{Vac} and $V_{2\text{nd}}$, then opening V_{Pd} to allow the system to fill with gas. Once it stabilized, V_{Pd} was closed and V_{Vac} was opened. The steps for heating the system and evacuating it in increments were repeated until the system reached 180 °C and all gas was evacuated from the Pd bed. After all the gas was evacuated from the Pd bed, the turbomolecular pump was turned on and the entire system was left at hard vacuum with all valves except for V_{H} and V_{Cal} open. The system was left with the turbomolecular pump on for multiple hours, often overnight. After the system demonstrated a steady-state hard vacuum, the Pd bed was cooled to the desired temperature by setting the temperature on the controller. Once the temperature cooled to about 20 °C the Q-drive was turned on to accelerate the cooling process. Once the system reached the desired temperature, V_{Iso} , V_{Cal} , and V_{Pd} were closed but V_{vac} , $V_{2\text{nd}}$, and V_1 were left open. The system was then prepared to be loaded.

Section 4: Results and Observations

Pressure-temperature-composition curves were generated in the temperature range 133 K to 373 K. The results are shown in figures 5 and 6 below.

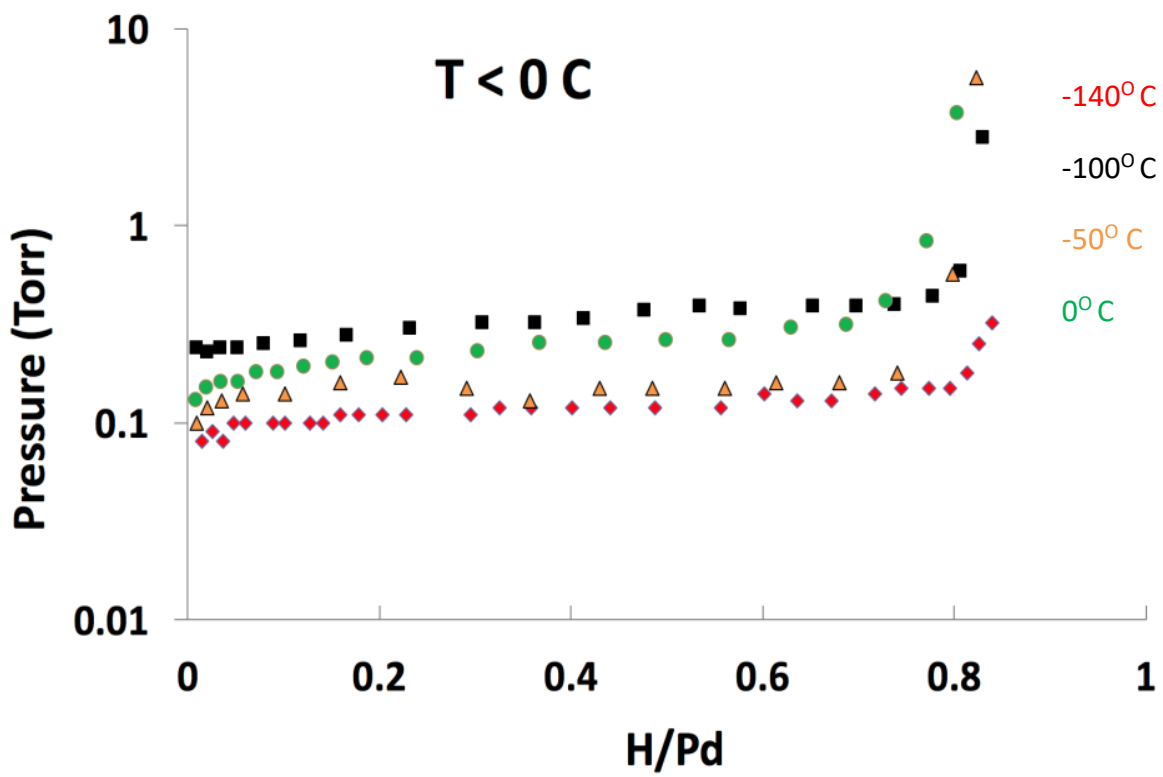


Figure 5: Measured isotherms for temperatures 0 C and below

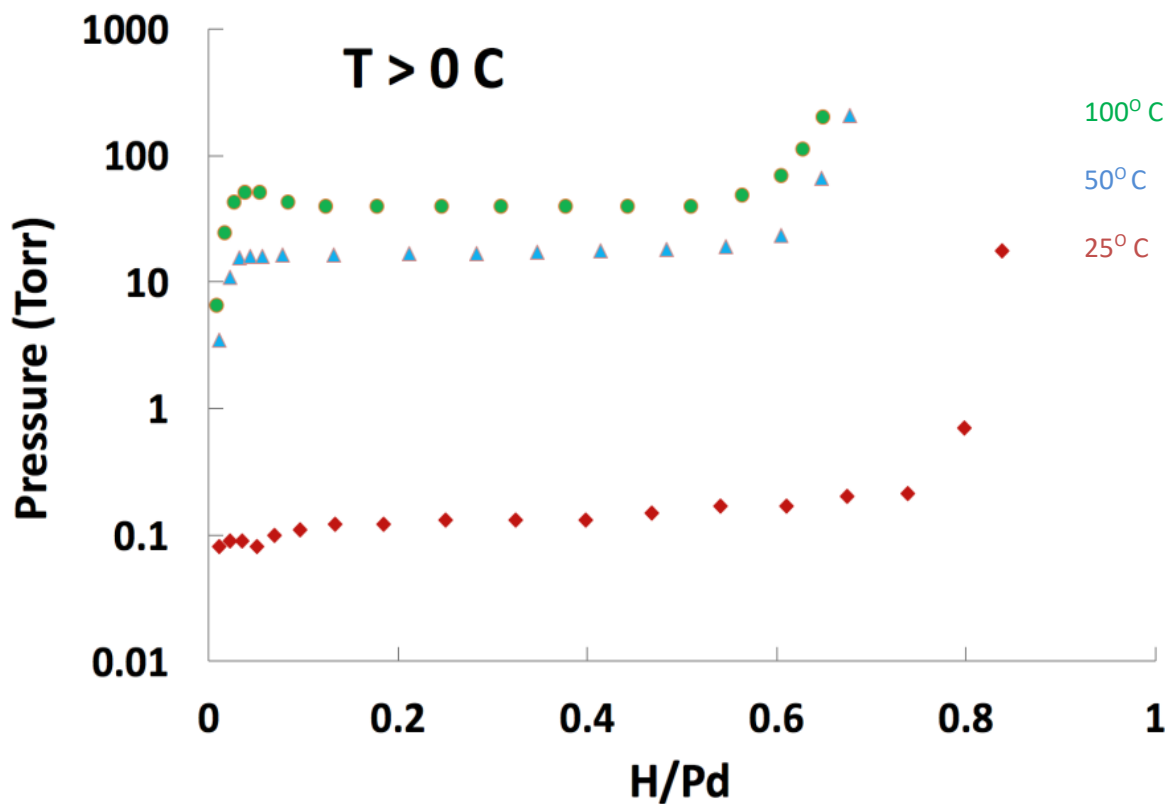


Figure 6: Measured isotherms for temperatures greater than 0°C

For data taken at temperatures above 273 K, increasing temperature corresponded to increasing pressure, but below 273 K decreasing temperature did not correspond with decreasing pressure, as can be seen on figure 5. The data below 273 K went against our hypothesis and the reason for this behavior is presented in the discussion section.

The loading times for different temperatures and hydrogen/metal ratios were obtained by plotting the pressure over the Pd bed as a function of time as shown in figures 7 and 8. The loading time is defined the time required for the pressure to decrease to a steady value.

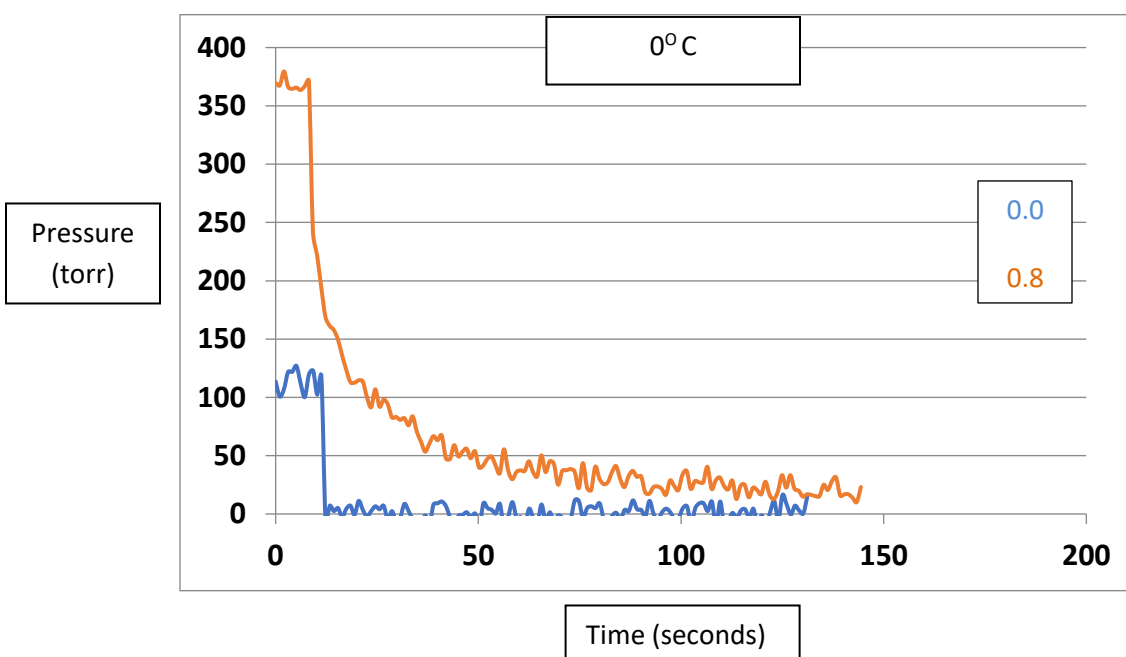


Figure 7: Pressure vs time graph at 0°C for hydrogen/metal ratios of 0.0 and 0.8.

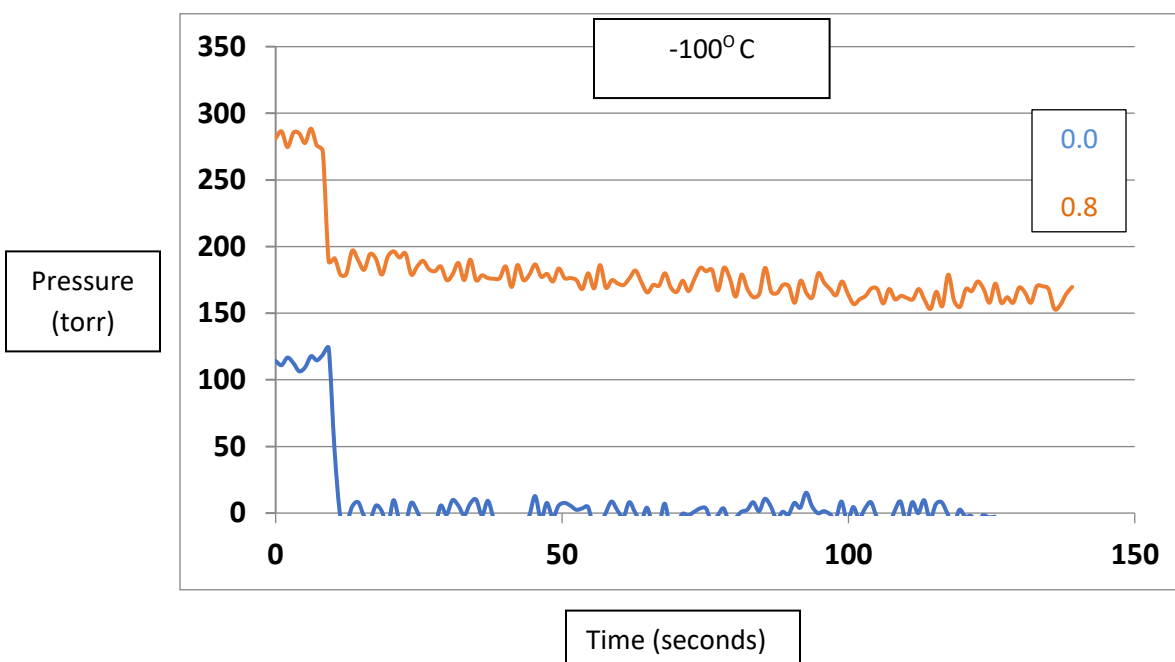


Figure 8: Pressure vs time graph at -100°C at hydrogen/metal ratios for 0.0 and 0.8.

By comparing Figure 7 and Figure 8, it can be observed that the loading time at a hydrogen/metal ratio of 0.8 is much larger at -100°C than at 0°C . In both figures, the pressure drops rapidly at a hydrogen/metal ratio of 0.0, but at a hydrogen/metal ratio of 0.8 the pressure continues to decrease slowly after the initial drop in pressure. In figure 7, the pressure continues to decrease for 140 seconds until it stabilizes. In figure 8, the pressure continues to decrease slowly for 140 seconds but does not fully stabilize with the measured time. After the initial drop in pressure, the pressure in Figure 8 decreases much more slowly than in Figure 7.

In figure 8 the pressure shown is much greater than the pressure graphed in figure 5 because figure 8 only shows the first 150 seconds of the loading time, while a typical load at -100°C would sit for about 30 minutes before reaching equilibrium.

Section 5: Discussion and Conclusions

The data in Figure 6 above 273 K was consistent with past data in studies such as Gillespie (2,3), but at 273 K and below (Figure 5), the data did not follow the expected trend. While the temperature was above 273 K, the descending temperature corresponded with decreasing pressure as seen in figure 6. The van't Hoff equation applied to the data for temperatures above 273 K and was calculated to be

$$\ln(P) = 18.9 - 5497/T$$

where P is in Torr and T is in Kelvin. The B value, which was calculated to be 18.9, was similar to the value of 16.9 obtained by Gillespie and Hall (3), who conducted research in the temperature range of 273 K to 453 K. In addition, the A value, which was calculated to be -5497, was similar to the value of -4225 obtained by Gillespie and Hall.

However, this van't Hoff equation does not apply to temperatures below 273 K. Below 273 K, the data is not as expected. Lowering the temperature below 273 K resulted in all data being fairly similar, despite spanning a temperature range of 140 K. The disorderly curves shown in figure 3 run counter to expectations. However, while the data were all fairly similar below 273 K, the plateau region did extend to a hydrogen/metal ratio of 0.8, compared to 0.6 at 323 K from Figure 6. This is consistent with the hypothesis that the lower temperatures would allow a larger percentage of hydrogen atoms to bond with the palladium, as seen in Figure 2. This is significant since it proves that palladium is valid as a pump and that it will store the maximum amount of hydrogen at temperatures below 273 K.

The cause of the unexpected plateau pressure behavior below 273 K is attributed to poor temperature control of the palladium powder. While the present design of the Pd bed is adequate for its intended use as a pump and compressor, it does not lend itself to a fine control of the palladium temperature for an investigation of the plateau pressures below room temperature. The cooling power of the Q-drive at the bottom of the palladium column and the heater at the top of

the palladium column establish a strong temperature gradient along the Z axis. While one portion of the bed is pumping the other portion is releasing hydrogen. The temperature gradient is not constant and is affected by the hydrogen gas pressure in the Pd bed, thereby changing the ratio of which part is releasing and which part is pumping. The investigation of the Pd/hydrogen isotherms at temperatures below room temperature requires a redesign of the test Pd bed with emphasis on maintaining the palladium at a uniform temperature.

Section 6: Acknowledgements

I would like to thank my LLE advisor Dr. Shmayda, as well as Dr. Sharpe for assisting me throughout the study and offering their advice regarding the experimental procedure and other facets of the study. Additionally, I would like to thank Dr. Craxton for organizing the Summer Internship Program and creating such a great opportunity.

Section 7: References

- 1: Metal Hydrides; Mueller, Blackledge, Libowitz Academic Press, 1968 Chapter 6
- 2: L. J. Gillespie and W. R. Downs. The Palladium-Deuterium Equilibrium. Research Laboratory of Physical Chemistry, Massachusetts Institute of Technology. Jul 10, 1939
- 3: L. J. Gillespie and F.P. Hall, The Palladium-Hydrogen Equilibrium and Palladium Hydride, American Chemical Society (1964)

Data services for scientific analysis on OMEGA and OMEGA EP

Matthew Galan

Fairport High School

Advisor: Richard Kidder

Laboratory for Laser Energetics

University of Rochester

Rochester, New York

January 2018

1. Abstract

A data service was developed that allows scientists to easily incorporate data from experiments on the OMEGA and OMEGA EP lasers into their data analysis programs. This data service is designed to replace the previous method of manually copying and pasting from a static web-based report page, which was prone to error, and to augment database querying with the programming language SQL, which is complex and not accessible outside the laboratory's perimeter firewall. The data service allows scientists to programmatically incorporate large amounts of data into their data analysis programs, including MatLab, Python, and Jupyter, regardless of their location. This simplifies data access for scientists and provides a one-step authentication scheme that is directly integrated into the data service, providing robust protection from unauthorized or malicious users.

2. Introduction

During experimental shot operations the OMEGA and OMEGA EP laser systems produce large quantities of highly valuable data on an hourly basis. While LLE prides itself on the efficiency of these lasers' operation, methods in which Principal Investigators (PIs) can currently access the data from their experiments are nothing short of obtuse, outdated, and prone to error. PIs had two options: use the OMEGA Shot Images and Reports page (*see Fig. 1*), or try their hand at writing custom SQL code to manually query the database. *Fig. 2* illustrates the relationship between the database, Shot Images and Reports page, and PIs. With the OMEGA Shot Images and Reports Page, PIs had to sift through pages of plaintext data without a standard format in order to find the data they needed. Once found, PIs had to manually copy, paste, and format the data to fit it to their needs. If PIs were to use SQL, they would have to first understand the complex Omega database schemas and data relationships, then write upwards of fifty lines in order to connect to the database and pick out the data they needed (*See Fig. 3*). Scientists external to the database networks can not access the database directly and cannot use SQL to query LLE data; they would either have to get it directly from a colleague in LLE, or by copying what is presented through web-based plaintext reports. Scientists that are within the facility that can access the database network were given the option of using a generic user account. However, a universal login does not protect data from those not authorized to see it, nor does it hold users connecting directly to the database accountable. In order to efficiently view, manipulate, and share experimental data, PIs need a solution that is secure, performant, and extendable.

OMEGA Shot UR LLE Query Page
Omega Home Page

Images and Reports

- OR/PGR/DriverLine
- Beam Termination Diagram
- Power Conditioning Reports
 - Summary Report
 - PCU Report
 - Fault Report
 - Reduced Waveform Data
- Calorimetry Reports
 - System Calorimetry
 - Fixed Calorimetry
 - Backscatter Calorimetry
 - Leg Energy Calorimetry
 - A-Split Calorimetry
 - Rover Calorimetry
 - Driver Calorimetry
- HED Reports
 - On-Target Beams
 - Beam Groups
 - Tripling Cell
 - Tripling Cell(Re-Order)
 - System Energy
 - Blue System Energy
 - BWA Degradation
- Laser Images
- Experimental Reports
 - TIM Diagnostic Setup Report
 - Online Target Diagnostic Report
 - Gas Pressure Report per Target
 - Neutron Yield
- Experimental Images

Log Number: 86353 UV On-Target / BWA Degradation Report
 SSD Mode: SSD
 26-Jul-2017 09:26:20

Last BWA swap before this shot: 07/07/2017 # target shots since: 80
 Reported losses are predicted from witness beam measurements taken on 07/18/2017 # target shots since: 32

Non-SG4 DPPs are not beam specific. Quoted transmissions are average for that DPP type.
 E-IDI-300 Average Loss set on 10/06/2016

Beam	HED On-Target UV Energy	Estimated BWA Loss	DPP	Estimated DPP Transmission	Adj. On-Target UV Energy
15	470.5	-0.7%	E-IDI-300	97.9%	457.5
16	480.2	-0.6%	E-IDI-300	97.9%	467.4
17	502.9	-0.7%	E-IDI-300	97.9%	489.0
10	469.1	-0.9%	E-IDI-300	97.9%	455.2
32	468.8	-0.7%	E-SG4-865	96.1%	447.5
33	486.5	-1.0%	E-IDI-300	97.9%	471.4
37	481.1	-0.8%	E-IDI-300	97.9%	467.4
39	471.3	-0.5%	E-IDI-300	97.9%	458.9
46	457.4	-0.7%	E-IDI-300	97.9%	444.6
59	446.3	-0.8%	SG8-FLAT	96.9%	428.8
66	463.8	-0.5%	SG8-FLAT	96.9%	447.0
67	462.0	-1.2%	SG8-FLAT	96.9%	442.3
68	484.1	-0.7%	E-SG4-865	96.1%	462.1
69	462.4	-1.0%	E-SG4-865	96.1%	439.7
Mean	471.9	-0.8%			455.6
RMS%	2.9	0.2%			3.3
P/V%	12.0	0.7%			13.2

Fig 1: The LLE OMEGA Short Images and Reports page

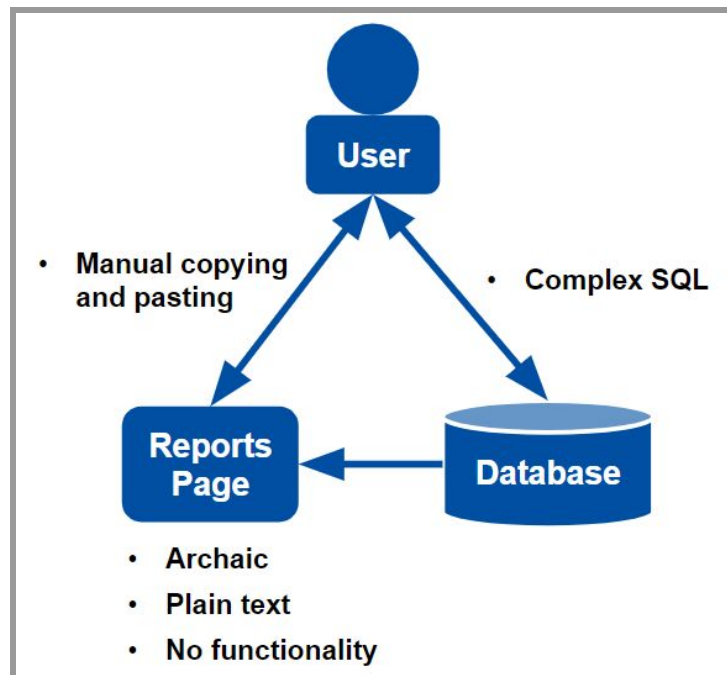


Fig 2: A triangular relationship between the user (PIs), database, and reports page.

```

1  function dbConn=getLLEdatabase(<name>, genericFlag)
2  % Use generic/generiuc if the user requests it.
3  if nargin < 2 || isempty(genericFlag) || ~genericFlag
4      uname = '';
5      pass = '';
6  else
7      uname = '<user>';
8      pass = '<password>';
9  end
10 if nargin < 1 || isempty(<name>)
11     % A function argument can override the environment variable
12     <name> = getenv('DATABASE');
13     if isempty(<name>)
14         % The replication database is the default
15         <name> = 'rep';
16     end
17 end
18
19 % On windows, this is all we need to do.
20 if strfind(computer, 'PCWIN')
21     dbConn = database(<name>, pass);
22 else
23
24     % If we get here, it's not windows. JDBC drivers should be
25     % available. Use them.
26     javaaddpath(fullfile(getenv('ORACLE_HOME'), 'lib', 'ojdbc6.jar'))
27     switch <name>
28     case 'exp'
29         <host> = 'hostname:port';
30
31     case {'ep_exp', 'epexp'}
32         <host> = 'hostname:port';
33         <name> = 'epexp';
34
35     case {'dev', 'ep_dev'}
36         %walnut?
37         <host> = 'hostname:port';
38
39     otherwise
40         error('ckin:UnknownDatabase',...
41             'Database ID "%s" is unknown.', <name>);
42     end
43
44     dbConn = database(<name>, uname, pass,...
45         'oracle.jdbc.driver.OracleDriver',...
46         ['jdbc:oracle:thin:@' <host> ':' <name>]);
47     end
48
49     % Make sure it's a working connection, or error out.
50     assert(isconnection(dbConn) == 1,...
51         'ckin:LLEdatabase:ConnectionFailed',...
52         'Connection to database "%s" failed: %s', dbName, dbConn.Message)

```

Fig 3: An example of the MatLab code needed to query the LLE database

3. Development

A data service was developed that would eliminate the need for PIs to retrieve the data from the OMEGA Shots and Reports page or write their own SQL to query the database. The data service calls prewritten SQL procedures inside the database in order to retrieve needed data (see Fig. 4).

```
PROCEDURE p_ASBOI
( p_LOG_NUM IN NUMBER,
  p_PI_USER IN VARCHAR2,
  p_result_set IN OUT SYS_REFCURSOR )
IS
  p_RID NUMBER := 0;
  l_cursor SYS_REFCURSOR;
  rid_not_allowed_error EXCEPTION;
BEGIN
  -- COMMENTS HERE
  SELECT omega.confirm_pi_has_access_to_rid( omega.find_RID_from_SRnum(p_LOG_NUM),p_PI_USER ) INTO p_RID FROM dual ;

  IF p_RID = 0
  THEN
    RAISE rid_not_allowed_error;
  ELSE
    OPEN p_result_set FOR
    select json_object
    ( 'RID' value sa_rid ,
      'ROSS_ID' value sa_interferometer_1,
      'offset' value sa_offset_1,
      'sweep' value sa_sweep_card_1,
      'time_interested' value sa_time_interested_1,
      'fiducial_delay' value sa_fiducial_delay_1,
      'sa_spec_inst' value sa_spec_inst,
      'sa_monitor_atten' value sa_monitor_atten,
      'sa_fiber' value sa_fiber,
      'sa_image_rotation' value sa_image_rotation,
      'sa_cylindrical' value sa_cylindrical,
      'sa_pulse_duration' value sa_pulse_duration,
      'ross_filter1' value sa_ross_filter1,
      'dove_prism' value sa_dove_prism_1,
      'delay_list' value sa_delay_list_1,
      'filter1' value sa_filter_1_1,
      'filter2' value sa_filter_1_2,
      'filter3' value sa_filter_3_1,
      'filter_list' value sa_filter_list_1,
      'total_filter' value sa_total_filter_1,
      'etalon' value sae_etalon,
      'ORDER' value sae_order,
      'sae_offset' value sae_offset
    )
    from SRF_ASBO a1,SRF_ASBO_ETALONS
    where SRF_ASBO_ETALONS.SAE_ETALON in
    (select regexp_substr(
      (select sa_etalon_list_1 from srf_asbo a2 where a2.sa_rid = a1.sa_rid),
      '[^,]+', 1, level) from dual connect by regexp_substr(
      (select sa_etalon_list_1 from srf_asbo a3 where a3.sa_rid = a1.sa_rid),
      '[^,]+', 1, level) is not null)
    and sa_rid in (p_rid) ;
  END IF;
  EXCEPTION
  WHEN rid_not_allowed_error THEN
    NULL ;
  WHEN OTHERS THEN
    NULL ;
END p_ASBOI ;
```

Fig. 4: An example database procedure that would be called by the data service.

The data service then formats the data into JavaScript Object Notation (JSON), a human readable format that is compatible with any programming language or most data analysis programs (including MatLab 2016 and up - earlier versions require a publicly available toolkit for JSON) . See Fig. 5 for an example of the JSON the data service returns.

```
[
  {
    "log": 84251,
    "hs_date": "2017-01-31T18:14:36",
    "beam": 10,
    "ir": 169.48577839206084,
    "green": 42.178540427902796,
    "uv": 510.83841640208857,
    "hed_total": 722.5027352220521,
    "cell_in": 921.6612565725013,
    "conv": 0.5794044704649481,
    "uv_on_target": 446.8364526458662,
    "cal_date": "2017-01-05T14:37:26",
    "trans_date": "2017-01-30T08:39:06",
    "dpr_serial": "352-22",
    "dpr_in_out": "IN ",
    "ocl_set": 513,
    "ssd_mode": "SSD"
  },
  {
    "log": 84251,
    "hs_date": "2017-01-31T18:14:36",
    "beam": 11,
    "ir": 171.45534470198933,
    "green": 41.44056133164611,
    "uv": 511.16208851801423,
    "hed_total": 724.0579945516497,
    "cell_in": 924.1653772613896,
    "conv": 0.5786240491859618,
    "uv_on_target": 446.89128855531703,
    "cal_date": "2017-01-05T14:37:26",
    "trans_date": "2017-01-30T08:39:06",
    "dpr_serial": "307-08",
    "dpr_in_out": "IN ",
    "ocl_set": 513,
    "ssd_mode": "SSD"
  },
],
```

Fig. 5: A snippet of JSON that the data service may return.

In order to maximize compatibility and usability, the data service is a RESTful web service. The service returns data based only on parameters in the URL that the user provides. Since all modern programming languages are capable of retrieving content provided by a webpage, the service is both operating system and language agnostic, meaning PIs can access the data easily no matter what their preferences may be. Given its web-based nature, the service is also location agnostic, given that users are authenticated. Furthermore, PIs working with large quantities of data may do so easily by simply iterating their URL parameter of choice. This allows for blocks of data to be retrieved in a convenient, organized manner.

In order to use the dataservice, PIs need to obtain a token from a web portal and then insert a url provided by the dataservice. Example implementations for Python 2 and MatLab 2016 are demonstrated in *Fig. 6* and *Fig. 7*, respectively.


```

1 # Import packages
2 import urllib
3 import json
4 # Pick a procedure and shot number
5 procedure = "asb01"
6 shot_num = 52818
7 token = "d798ee4c30bc9c0808e6debb797a4e7cb19b8f4bdd5f58f9b7fcc794538c752c"
8 # Get a dictionary from the JSON using json.loads()
9 data = json.loads(urllib.urlopen("http://lle-stage-informatics2:3140/api/" + procedure + "/" + str(shot_num)).read() + "/" + token)
10 # Example use of dictionary - get the sae_offset of the first entry
11 print data[0]["sae_offset"]

```

Fig 6: The only Python 2 code needed to use the data service.

```

1 % Pick a procedure and shot number
2 - procedure = 'asb01';
3 - shot_num = 52818;
4 - token = 'd798ee4c30bc9c0808e6debb797a4e7cb19b8f4bdd5f58f9b7fcc794538c752c';
5 % Get a struct from the JSON using webread()
6 - data = webread(strcat('http://lle-stage-informatics2:3140/api/', procedure, '/', num2str(shot_num), '/'), token));
7 % Example use of struct - get the sae_offset of the first entry
8 - val = data(1).sae_offset;

```

Fig 7: The only MatLab 2016+ code needed to use the data service.

Several improvements were made to the code driving the data service. The original data service code had a separate function written for each database procedure. The code inside of these functions was identical, except for the names of the database procedure, which were hard coded in. This meant for every database procedure that was written, of which there would be dozens in the future, the same code block in the data service code had to be duplicated and the name for the procedure modified. *Fig. 8* illustrates the hard coded nature of the functions.

Users specify only the shot number.

```
163 app.get('/api/cryo/:sid', function(req, res){
164   res.setHeader('Content-Type', 'application/json');
165   var sid = req.params.sid;
```

Notice that the procedure name isn't a variable; it's hard-coded in.

```
178   connection.execute(
179     "BEGIN omega.lle_web_pkg.SRnum_cryo1j(" + sid + ", :rc); END;",
```

Fig. 8: Snippets of a data service function

The data service functions in question were reduced down to a single template version that takes the procedure name as an argument provided in the URL in addition to the shot number. Additionally, user authentication was being developed at the same time. Users would provide their unique, temporary ID string at the end of the URL. The data service would then verify that the user was authorized to view the data they were trying to access. Fig. 9 reveals the changes made to the data service functions.

Users specify the name of the procedure, the shot number, and their identity.

```
91 app.get('/api/:procedure/:shotNum/:userID', function (req, res) {
92   res.setHeader('Content-Type', 'application/json');
93   var procedure = req.params.procedure;
94   var shotNum = req.params.shotNum;
95   var userID = req.params.userID;
```

```
112   connection.execute(
113     //Here we call the database procedure
114     "BEGIN omega.lle_diagnostics_pkg.p_" + procedure + "(" + shotNum + ", " + userID + ", :rc); END;",
```

The web service then uses that information to call the database procedure.

Fig 9: The new, template version of the data service functions.

These revisions were successful in reducing both the size of the code behind the data service and the work required to maintain its functionality. *Fig. 10* provides a visual representation of the resultant code reduction.

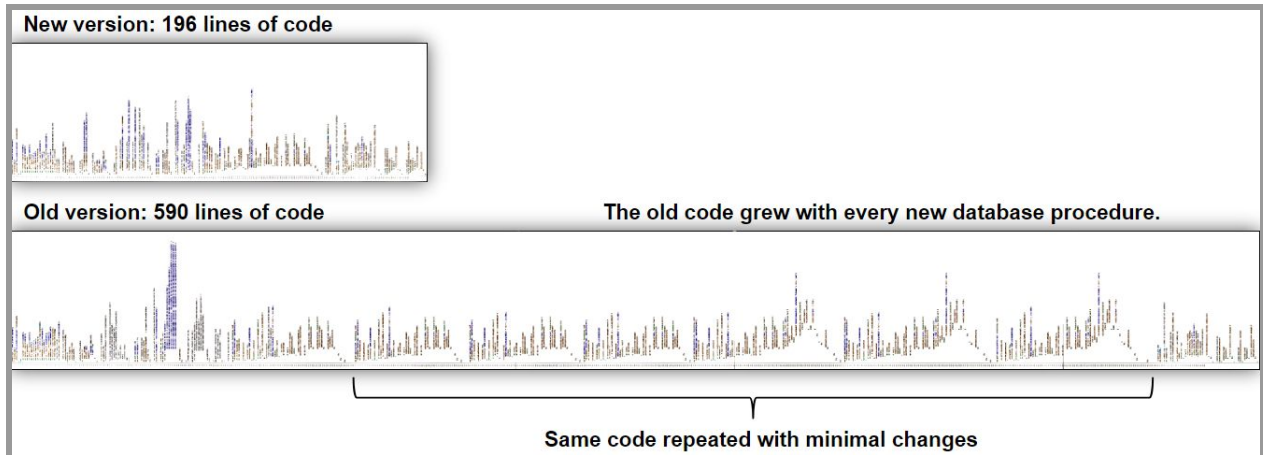


Fig 10: A side by side comparison of actual pictures of the old and new code behind the data service. The code displayed is rotated 90°.

5. Future Plans

Built-in data service support for the LLE diagnostic analysis page is still under development. This feature would allow PIs to view and graph selected data instantly without having to pull the data from the data service using a programming language (such as Python 2) or a data analysis program (such as MatLab 2016). The data service integration is also the mechanism that provides PIs with an easy way to get the URL needed to get a specific data set from the data service. See *Fig. 11* for a mockup of what the LLE diagnostic analysis page may look like with these features.

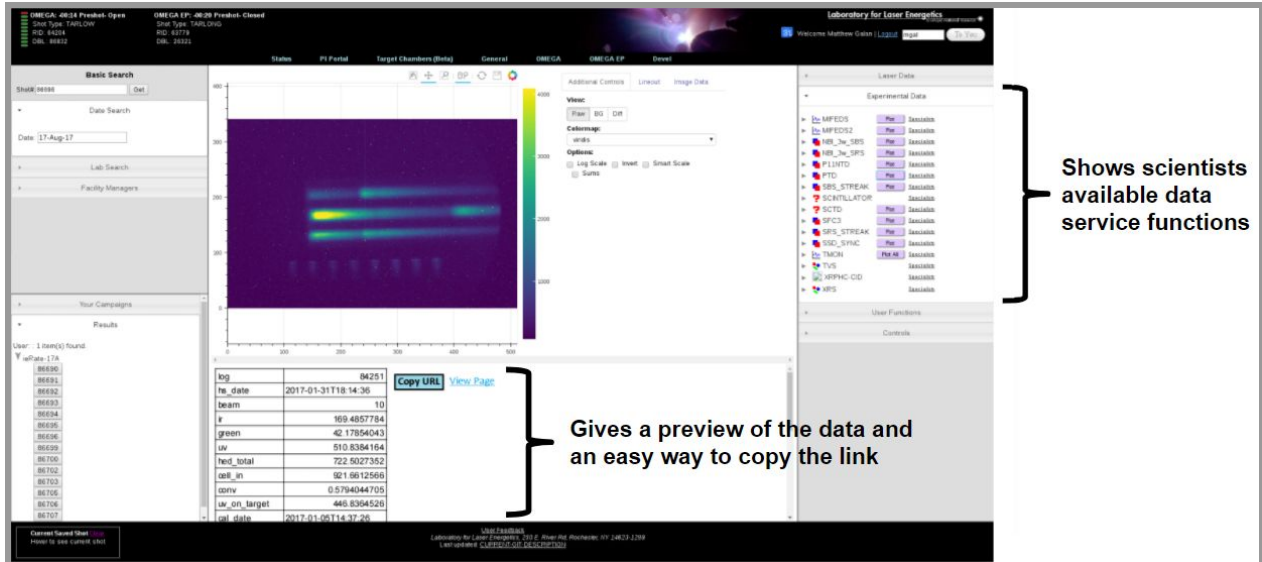


Fig 11: A mockup of the in-development diagnostic analysis page

6. Conclusion

In order to streamline the data retrieval process for the OMEGA and OMEGA EP laser systems, a data service was developed that allows PIs to seamlessly incorporate data from the database into their favorite data analysis solutions using only a few lines of prewritten code. Older methods involved manually copying, pasting, and formatting large blocks of data from the OMEGA Shot Images and Reports page, or directly connecting to the database with over fifty lines of SQL. Integration into the LLE Diagnostic Analysis page, as well as user authentication, is currently in development.

7. Acknowledgements

My sincerest gratitude to Mr. Richard Kidder, Dr. Stephen Craxton, and Ms. Jean Steve for making this project, as well as the LLE Summer Research Program as a whole, possible. This was not only an incredible opportunity, but a tremendous learning experience. Of course, I would be nowhere without the unending support from my family and friends. Thank you.

Analysis of Hot Spot Asymmetries Using Synthetic X-Ray Images

Claire Guo

Penfield High School

Advisor: Dr. Arijit Bose

Co-advisor: Dr. Reuben Epstein

Laboratory for Laser Energetics

University of Rochester

Rochester, NY

January 2018

Abstract

In inertial confinement fusion (ICF) implosions, self-emission x-ray images are used to estimate the hot-spot size and shape. The asymmetry modes of the hot spot can be inferred using these images. Both time-integrated and time-resolved images can be obtained from cryogenic implosion experiments performed on the OMEGA laser. These images are analyzed for the detection of long- and mid-wavelength asymmetries that can be degrading the experiments. This is done by comparison of the experimental images with synthetic images obtained from hydrodynamic simulations. The stagnation phase of implosions is simulated using the 2-D hydrodynamic code *DEC2D*, followed by post-processing using the atomic-physics radiation-transport code *SPECT3D* to produce the synthetic images. From the synthetic images, it is found that the time evolution of the inferred radius and shape of the image differs for implosions with low- and mid-mode asymmetries. This finding can be used to investigate the asymmetry modes degrading the implosion experiments.

2. Introduction

In direct-drive inertial confinement fusion (ICF) [1], multiple high-power laser beams are used to irradiate a deuterium (D) and tritium (T) gas-filled spherical target in order to compress it to high temperatures and pressures. Under these conditions, the fusion of D and T ions is facilitated, leading to energy release. The 60-beam OMEGA laser at the Laboratory for Laser Energetics (LLE), University of Rochester is capable of delivering about 26-30 kJ of energy within a ~ 2 ns pulse duration. This high-power laser is used to routinely perform ICF implosion

experiments. The ultimate goal of ICF research is to produce unlimited clean and safe energy through thermonuclear fusion.

High-intensity laser beams are focused symmetrically on a spherical shell made up of a DT ice layer coated on the inside of a plastic (CH) layer and filled with DT gas. The energy from the laser causes the plastic layer to ablate outward, thereby compressing the DT ice layer and gas fill of the target. This is analogous to rocket propulsion directed spherically inward. The rapid compression of the gas, by a factor of $\sim 20^3$ in volume within a span of $\sim 1-2$ ns, heats it up to high temperature. This allows deuterium and tritium nuclei to collide and fuse, each fusion reaction producing an alpha particle, a neutron, and about 17.6 MeV of fusion energy. Initially, the DT shell is accelerated inwards. When the shell nears the origin, it encounters resistance from the hot compressed gas and decelerates.

In a perfect scenario, a spherically symmetric compression of the fuel can lead to significant fusion yields on OMEGA, which have been estimated using simulations. However, nonuniformities arising from several plausible sources can provide initial seeds for the Rayleigh-Taylor instability [2]. During the deceleration phase of an implosion, this instability occurs at the interface of the low-density hot spot (the hot compressed gas) and the high-density shell. The Rayleigh-Taylor instability can introduce growth of compression asymmetries that degrade the fusion yield, relative to the predictions of uniform symmetric calculations. Nonuniformities present on the target are characterized by the mode number ℓ . Targets with two perturbation wavelengths around a great circle will have $\ell=2$. Low-mode asymmetries include $\ell=1-6$ perturbations, mid-mode asymmetries include $\ell=8-40$ perturbations, and high-mode asymmetries include perturbations with $\ell>40$. Different modes can also be combined. For

direct-drive implosions on OMEGA, it is anticipated that the core is degraded by a combination of low and intermediate modes, as shown by Bose *et al.* [3] and Regan *et al.*[4] Although the actual source of the asymmetries is not uniquely identified, low modes can arise from several factors, including long-wavelength DT ice modulations, target positioning, laser beam balance, and laser beam pointing. In addition, the superposition and overlap of all 60 OMEGA laser beams can produce intensity variations that introduce intermediate-mode nonuniformities.

The hot spot produces x-ray emission during the final stages of the compression that can be imaged using x-ray framing cameras. These hot-spot self-emission images can provide information about the symmetry of the hot spot. However, since the hot-spot radius is of the order of $\sim 20 \mu\text{m}$, these images are limited by the spatial resolution arising from the imaging optics. In order to better understand these images and identify the specific perturbation modes present in the target during the experiments, the x-ray images are compared with simulated synthetic x-ray images of different modes. The images can be time integrated or time resolved as outlined in Fig. 1.

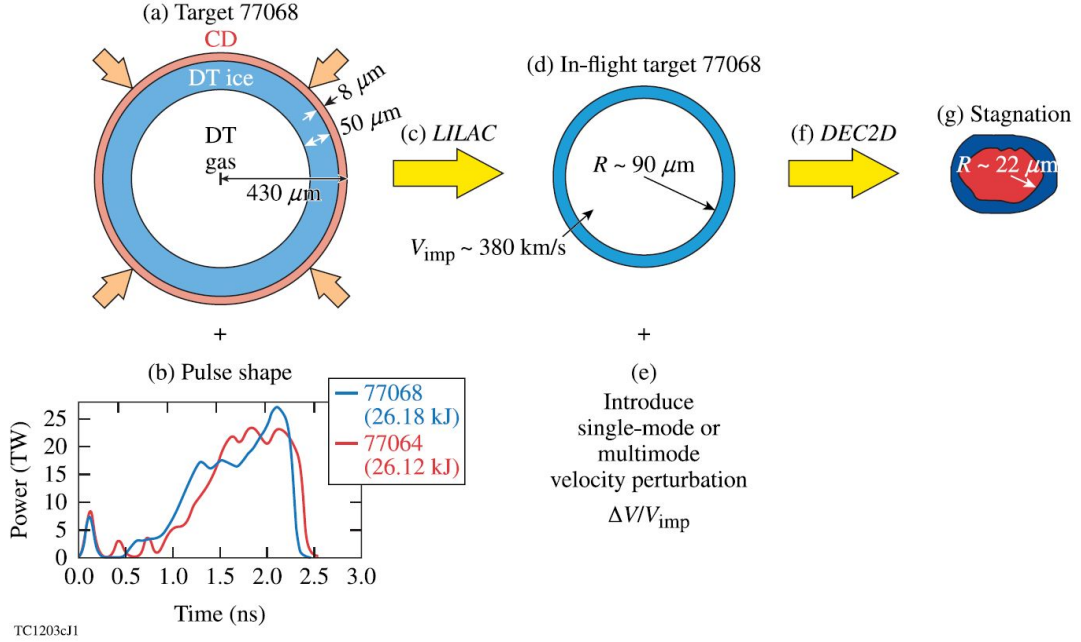


Figure 1: The process of producing synthetic x-ray images for comparison with experiments. The target (a) and pulse shape (b) are used as initial conditions for the 1-D hydrodynamic code LILAC, which is used to (c) simulate the acceleration phase of implosions. The hydrodynamic profiles from the (d) in-flight target simulation are transferred to DEC2D; single- or multimode velocity perturbations are (e) introduced at the inner surface of the shell. (f) The deceleration phase of the implosion is simulated in 2-D. (g) The stagnation parameters are extracted from these simulations.

Synthetic images with different asymmetry modes were processed using DEC2D [5] and SPECT3D [6] calculations. These images were normalized to the maximum intensity for each image and fit with the following function:

$$f(x,y) = e^{-[(x/a)^2 + (y/b)^2]^{\eta/2}}$$

The hot-spot radius $R_{17}(t)$ is defined by $R_{17} = \sqrt{a \times b} [-\log(0.17)]^{1/\eta}$. For a circularly symmetric image, $R_{17}(t)$ gives the radius where the intensity is 17% of maximum. The index

$\eta(t)$ represents the index of the super-Gaussian fit, with $\eta = 2$ representing a Gaussian

function. Data such as the time evolution of the hot-spot radius $R_{17}(t)$ and the super-Gaussian

index $\eta(t)$ can be used to infer the presence of mid-modes in implosions.

Figure 2 shows an example implosion for which the similarity between the experimental x-ray image and the simulation post-processed image can be seen. Comparison of the experimental images with synthetic images, like in Fig. 2, provides a tool to investigate the asymmetries that are degrading the experiments. The similarities between Images (b) and (c) and both line-outs in Image (d) demonstrate the validity of the synthetic reconstructions.

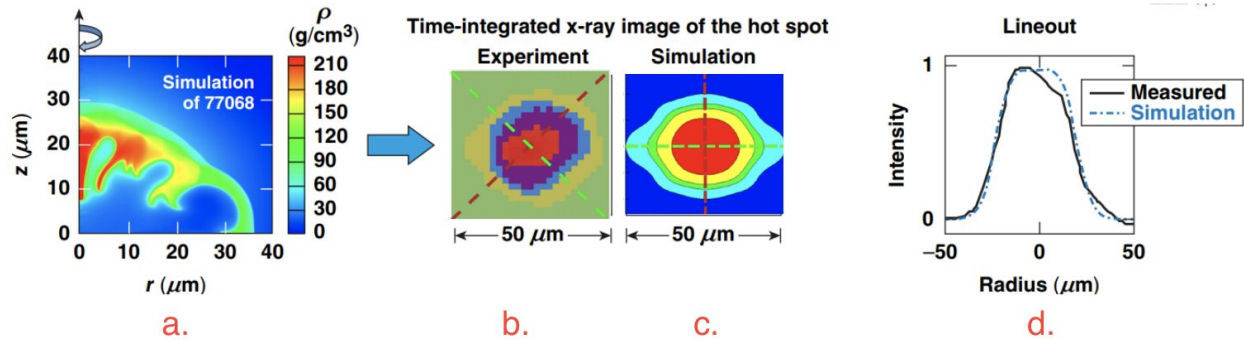


Figure 2: Comparison of synthetic images with the experimental images. Image (a) shows the DEC2D simulation of the shot 77068. Image (b) shows the time-integrated x-ray image from the experiment and image (c) shows the SPECT3D generated synthetic image. Image (d) is a plot of the line-outs taken from the red dashed line of Image (b) and the green dashed line of Image (c).

3. Application of the image processing procedure

Case 1: Symmetric implosion simulations

Synthetic images for symmetric implosion simulations, i.e. without any seed velocity perturbation, were produced from *DEC2D* and *SPECT3D*. An example is shown in Fig. 3. These images were used to study the relationship between the target density profile and the x-ray emission. Lineouts were taken along the x- and y- axes of the synthetic x-ray image, in order to plot the relationship between normalized intensity and radius and to calculate the super-Gaussian index.

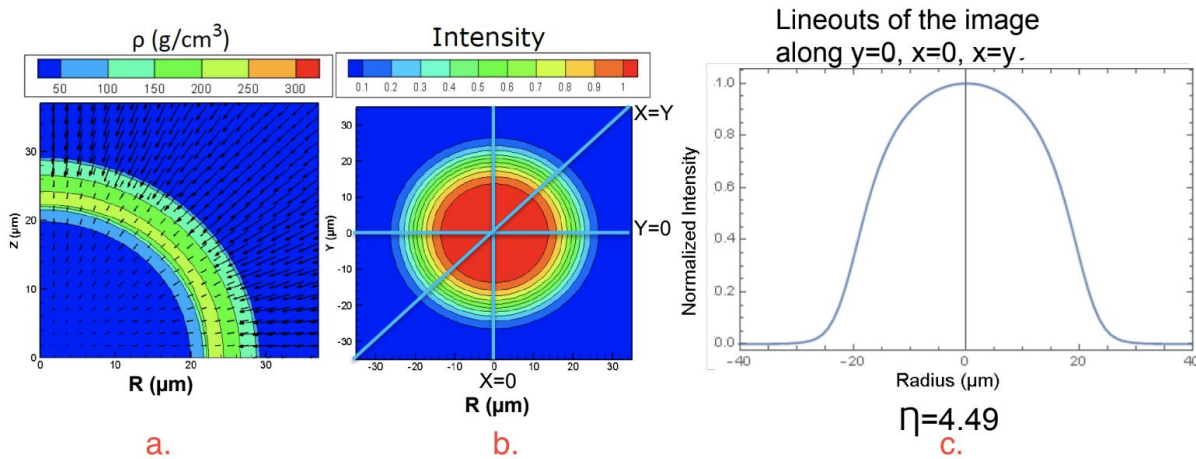


Figure 3: Simulation results for a symmetric implosion (mode 0). (a) is a contour plot of density (g/cm^3) in the (R, Z) plane, (b) is a time-integrated simulated SPECT3D image, and image (c) is a graph of normalized intensity vs. radius from line-outs taken along $y=0$, $x=0$, and $x=y$ from (b). The super-Gaussian index is found to be 4.49. The y-axis of (b) corresponds to the z-axis of symmetry of the simulation (a). Clean SPECT3D images are used to calculate the hot-spot radius and super-Gaussian index.

Image (a) shows that the density profile is symmetric and Image (b) shows that the target is evenly compressed with the maximum intensity of the hot spot being centralized in the middle of the target. The lineouts seen in Fig. 3 (c) are also uniform and identical.

This process of image development was repeated three more times for low, mid, and combination-mode targets. The new images with perturbations were compared to that of the clean simulation of Fig. 3 in order to study the effect of different Rayleigh-Taylor instability modes on an implosion.

Case 2: Simulations with low-mode asymmetry

Low-mode ($\ell=2$ asymmetry) was introduced in the DEC2D simulation. The resulting density contour plot is shown in Fig. 4(a). The x-ray image produced using *SPECT3D* is shown in Fig. 4(b). Compared to the images seen in Fig. 3, the images in Fig. 4 are less uniform because of the asymmetry.

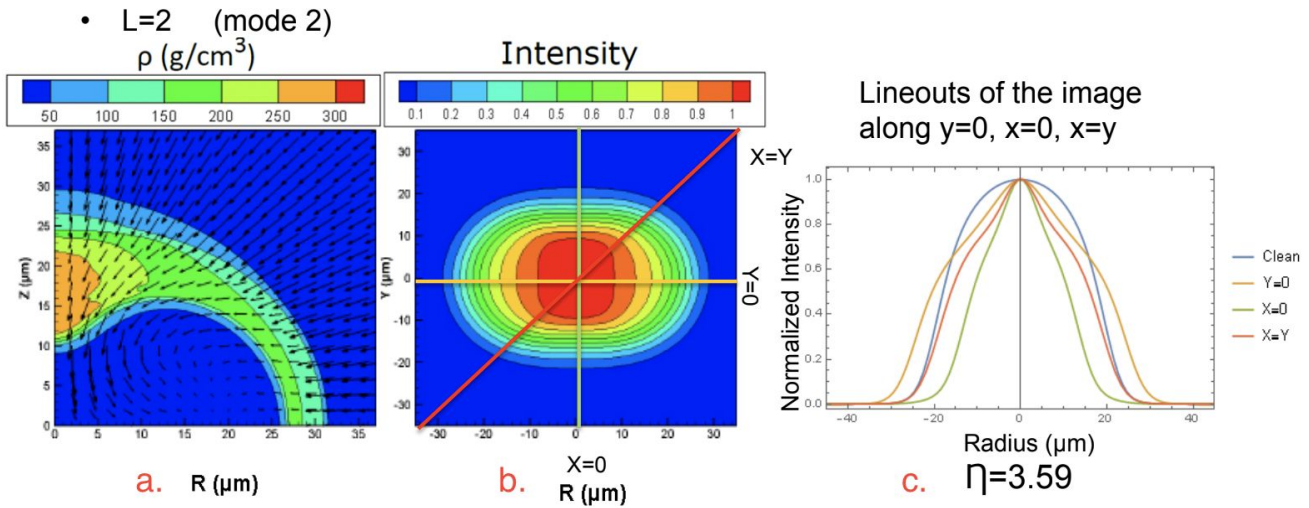


Figure 4: Simulation results for a low-mode (mode 2) implosion. (a) is a contour plot of density (g/cm^3) in the (R,Z) plane, (b) is a time-integrated simulated SPECT3D image, and image (c) is a graph of normalized intensity vs. radius from line-outs taken along $y=0$, $x=0$, and $x=y$ from (b). The super-Gaussian index is found to be 3.59. The y -axis of (b) corresponds to the z -axis of symmetry of the simulation (a). SPECT3D images are used to calculate the hot-spot radius and super-Gaussian index.

Areas of greater density are centralized on the upper and lower areas of the target shell. The resulting intensity contours of Fig. 4(b) are close to elliptical in shape. The lineouts taken in Image (c) are slightly more peaked in the center than that for the clean simulation. This causes the super-Gaussian index to decrease from the 4.49 of Fig.3(c) to 3.59.

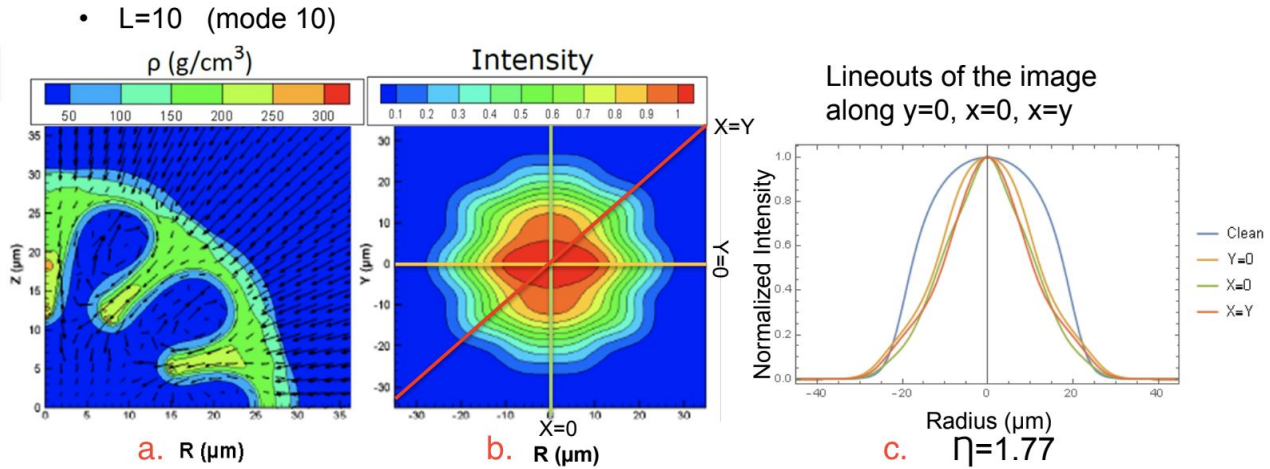


Figure 5: Simulation results for a mid-mode (mode 10) implosion. (a) is a contour plot of density (g/cm^3) in the (R,Z) plane, (b) is a time-integrated simulated SPECT3D image, and image (c) is a graph of normalized intensity vs. radius from line-outs taken along $y=0$, $x=0$, and $x=y$ from (b). The super-Gaussian index is found to be 1.77. The y-axis of (b) corresponds to the z-axis of symmetry of the simulation (a). SPECT3D images are used to calculate the hot-spot radius and super-Gaussian index.

Case 3: Simulations with mid-mode asymmetry

A DEC2D simulation with a mid-mode asymmetry ($\ell=10$) was post-processed using SPECT3D. The resulting density contour plot is shown in Fig. 5(a). Compared with that in Fig. 3(a), the density contours show significant structure. Areas of greater density begin traveling into the middle of the target and more density variations occur on the target shell, compared to clean and low-mode simulations. The target has compressed so that there are peaks and troughs on the inner surface instead of it being compressed smoothly into a sphere or an ellipse. The SPECT3D image of Fig. 5(b) mirrors the structure seen in the density contour plot of Fig. 5(a). The lineouts taken in Image (c) are more strongly peaked at the center than the clean and low-mode lineouts. This causes the super-Gaussian index to decrease substantially from the 4.49 of the symmetric case of Fig. 3(c) to 1.77. There is also less variation between the three lineouts.

Case 4: Simulations with combination of low- and mid-mode asymmetry

X-ray images for a simulation with both mode 2 and mode 10 perturbations were processed. These images were used to study how a combination of two modes would affect the properties of the x-ray images.

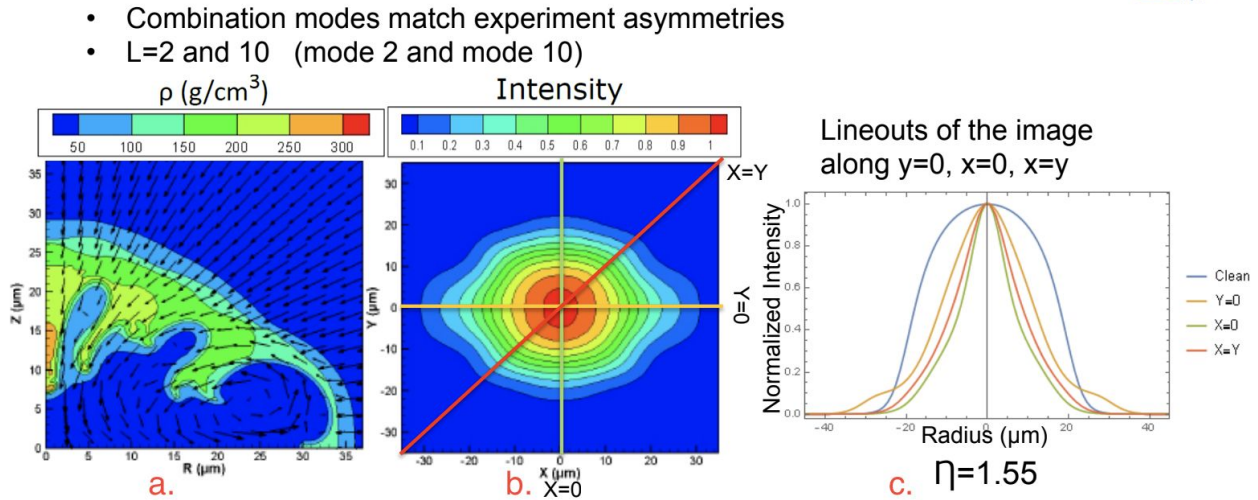


Figure 6: Simulation results for a combination-mode (mode 2 and 10) implosion. (a) is a contour plot of density (g/cm³) in the (R,Z) plane, (b) is a time-integrated simulated SPECT3D image, and image (c) is a graph of normalized intensity vs. radius from line-outs taken along $y=0$, $x=0$, and $x=y$ from (b). From (c), the super-Gaussian index is found to be 1.55. The y-axis of (b) corresponds to the z-axis of symmetry of the simulation (a). SPECT3D images are used to calculate the hot-spot radius and super-Gaussian index.

Compared with those in Figs. 3, 4, and 5, the density structures in Fig.6(a) are distributed unevenly around the target. Areas of greater density are located on the upper and lower areas of the target and travel into the middle of the target. The target has compressed so that the target is stretched in the R direction. The intensity image in Fig. 6(b) is similarly stretched. The lineouts taken in Image (c) show a combination of the variability seen in Fig. 4(c) and the narrowing at

the center seen in Fig. 5(c) and are more strongly peaked at the center than the clean, low-mode, and mid-mode lineouts. This causes the super-Gaussian index to decrease further to 1.55.

4. Time evolution history of the hot-spot size

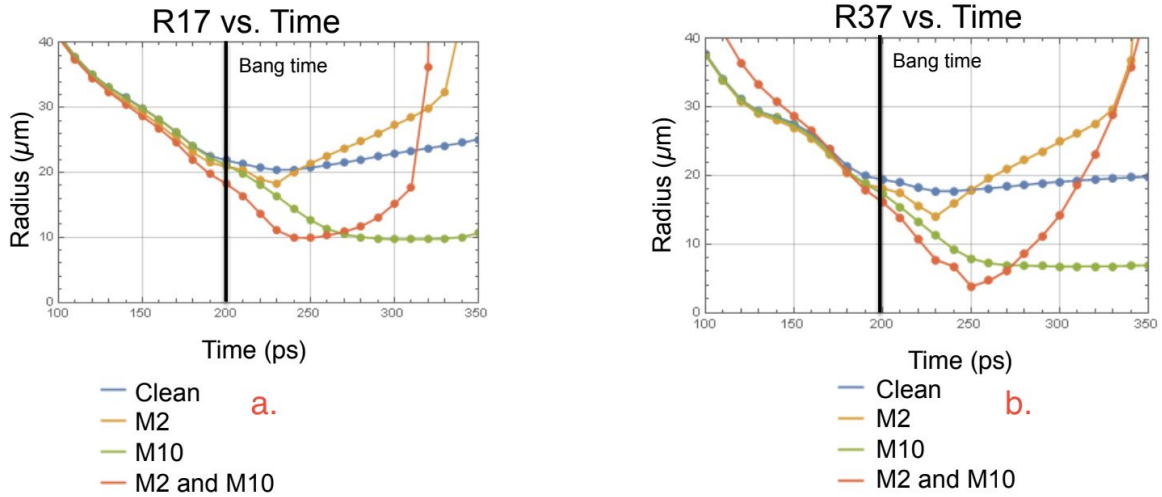


Figure 7: Graphs of (a) radius R_{17} and (b) radius R_{37} as functions of time.

The hot-spot radius R_{17} and the radius $R_{37} = \sqrt{a \times b} [-\ln(0.37)]^{1/\eta}$ at 37% of maximum intensity are plotted as functions of time in Fig. 7. This figure shows how these radii change over time for different perturbation modes. When compared with data from experimental implosions, the data from these graphs can be used to infer the presence of different perturbation modes.

5. Time evolution history of the super-Gaussian index

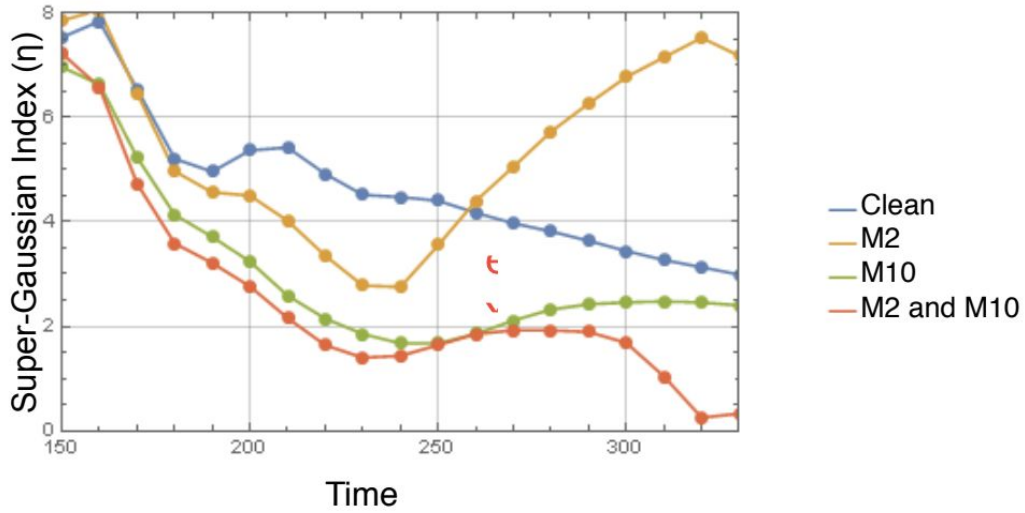


Figure 8: Graph illustrating the relationship between super-Gaussian index (η) and time (ps)

From the SPECT3D images produced, the super-Gaussian index for the clean, mode 2, mode 10, and combination modes was isolated and plotted in Fig. 8. Fig. 8 shows that the super-Gaussian index decreases at the end of the implosion during laser shots with combination mode perturbations located on the target. These results provide a preliminary indication that the time dependence of the mode-number content and the super-Gaussian index are related. Through comparison with data from experimental implosions, relationships such as this may be used to infer the presence of perturbations of different mode numbers.

6. Conclusion

SPECT3D synthetic x-ray images are used to analyze asymmetries of the hot spot. Detection of mid-mode asymmetries in implosions is challenging. However, the synthetic x-ray images produced through this study are effective as a means for understanding the shape of

target profiles with perturbations of different mode numbers over the course of a target implosion. In addition, the time evolution of the hot-spot radius and the super-Gaussian index appear to be related, allowing the presence of mid modes in implosions to be inferred through comparisons with similar data from experimental implosions. These techniques can be implemented to better understand target perturbations, diagnose experimental implosions for potential issues, and analyze target compression over the course of the implosion.

7. Acknowledgements

This project would not have been possible without the help of my advisors, Dr. Arijit Bose and Dr. Reuben Epstein, whose patient support and assistance have guided me along the entire process. I would like to thank Dhruvir Patel, who guided me through producing the synthetic images, and Alison Christopherson who provided the data used to create my images. I would also like to thank Dr. Craxton for providing me with the wonderful opportunity to participate in the LLE high school program and conduct this research project. Finally, I would like to thank the Laboratory for Laser Energetics for this amazing learning experience.

8. References

- [1] R.S. Craxton *et al.*, "Direct-Drive Inertial Confinement Fusion: A Review," *Physics of Plasmas* **22**, 110501 (2015).
- [2] D.H. Sharp, "An Overview of Rayleigh-Taylor Instability," *Physica D*. **12**: 3–18 (1948).
- [3] A. Bose *et al.*, "The Physics of Long- and Intermediate-Wavelength Asymmetries of the Hot Spot: Compression Hydrodynamics and Energetics," *Physics of Plasmas* **24**, 102704 (2017)
- [4] S. Regan *et al.*, "Demonstration of Fuel Hot-Spot Pressure in Excess of 50 Gbar for Direct-Drive, Layered Deuterium-Tritium Implosions on OMEGA," *Phys. Rev. Lett.* **117**, 025001 (2016).
- [5] A. Bose *et al.*, "Hydrodynamic Scaling of the Deceleration-phase Rayleigh-Taylor Instability," *Phys. Plasmas* **22**, 072702 (2015)
- [6] J. J. MacFarlane, I. E. Golovkin, P. Wang, P. R. Woodruff, and N. A. Pereyra, "SPECT3D—A Multi-Dimensional Collisional-Radiative Code for Generating Diagnostic Signatures Based on Hydrodynamics and PIC Simulation Output," *High Energy Density Phys.* **3** (1-2), 181-190 (2007).

Ambient-Temperature Ammonia Removal Process for Sol-Gel Anti-Reflective Coating Solutions

Joyce Luo

Pittsford Mendon High School

Advisor: Kenneth L. Marshall

University of Rochester

Laboratory for Laser Energetics

Summer High School Research Program 2017

January 2018

Abstract

The current sol-gel preparation process utilizes refluxing (boiling of a solution with condensation of the solvent) to remove the ammonia catalyst and halt the formation of a rigid silica-oxide network. This process requires specialized glassware, cooling water, and a controlled heat source, all of which require precise control and frequent monitoring. Removal of the ammonia by the process of bubbling a gas into the solution (purging) significantly simplifies the process and eliminates the need for a heat source. The ability to displace ammonia dissolved in 2.5 L of ethanol by purging using three inert gases (argon, helium, and nitrogen) was evaluated at a flow rate of 4 L/min in a simple setup to assess the new process efficiency versus refluxing. Similar ammonia removal rates were observed for all three gases (~24 hours to reduce the solution pH from 11 to 7). Nitrogen purging was successfully applied to remove ammonia from a 2.5 L batch of production sol-gel solution in ~42 hours with minimal effort and attention. The purging process potentially enables 2-3x more sol-gel solution to be processed in 24-43 hours compared to refluxing.

1. Introduction

Sol-gel anti-reflective coatings are used in the OMEGA EP and OMEGA laser systems at the Laboratory for Laser Energetics (LLE) to prevent beam energy losses due to reflection, known as Fresnel losses. These coatings are created from a solution of tetraethylorthosilicate (TEOS), H₂O, and ethanol. Ammonium hydroxide is then added as a basic catalyst, which increases the pH of the solution to approximately 11. Under these conditions, TEOS undergoes *hydrolysis* by OH⁻ ions, resulting in elimination of ethoxide radicals that are converted to additional ethanol. The remaining partially hydrolyzed orthosilicate skeleton then undergoes a *condensation* reaction, where these hydroxyl-terminated orthosilicates combine to eliminate

water and begin the formation of colloidal silica particles (Fig. 1, top) . These particles are then aged until they reach the desired size and form a colloidal silica structure. Refluxing (boiling of a solution with condensation of the solvent) removes the ammonia catalyst, which terminates particle growth and decreases the pH to 7. This creates a sol-gel coating solution that can be spin- or dip-coated onto glass optics (Fig. 1, bottom).

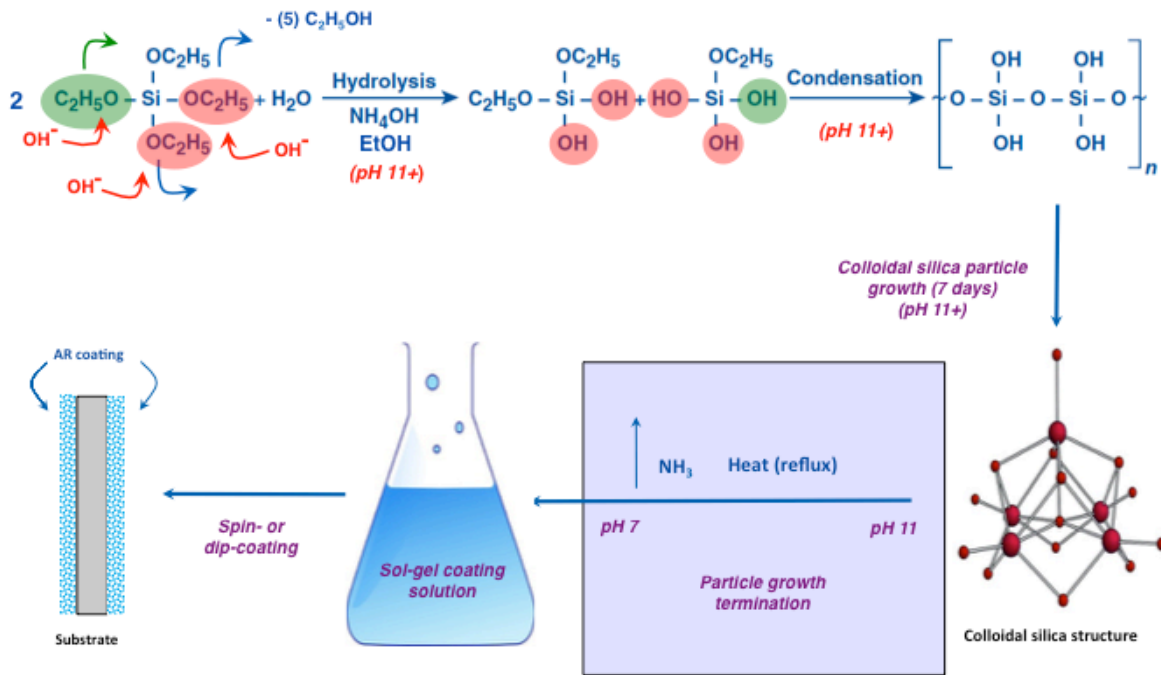


Fig. 1: Formation of an anti-reflective coating via the sol-gel preparation process. Ammonium hydroxide is added as a catalyst to the solution of H₂O, ethanol, and tetraethylorthosilicate (TEOS), which initiates hydrolysis of the terminal groups followed by condensation of two or more partially-hydrolyzed siloxane chains to create colloidal silica particles of a desired size. Refluxing terminates particle growth and removes the ammonia to create a sol-gel coating solution that can be spin- or dip-coated onto glass optics.

Refluxing involves a complicated setup, which must be monitored frequently throughout the ammonia removal process. As shown in Figure 2a, the setup includes a 5 L round-bottom flask, a heating mantle, an electronic temperature controller, glass wool for insulation, a magnetic stir plate with a corresponding magnetic stirrer, and a reflux-distilling head with an integral water-cooled condenser. A steady stream of water through an inlet in the distilling head must be maintained throughout the refluxing cycle so that condensation of the solvent (ethanol)

can occur (Fig. 2b). The pH is measured through an outlet on the side of the distilling head (Fig. 2b). One reflux apparatus can process 2 L of sol-gel, and two reflux apparatuses can be set up at a time. Therefore, only 4 L of sol-gel can be processed within one 24-hour cycle. The Optical Manufacturing Group (OMAN) at LLE produces 20 L batches of sol-gel that have been aged to the desired particle size and transfers them in 4 L Erlenmeyer flasks to the LLE Optical Materials Laboratory. The sol-gel must then be transferred again into the 5 L round-bottom flasks of the reflux apparatuses. Overall, this process is cumbersome, and it requires 5-6 days to process a complete batch of sol-gel from OMAN.

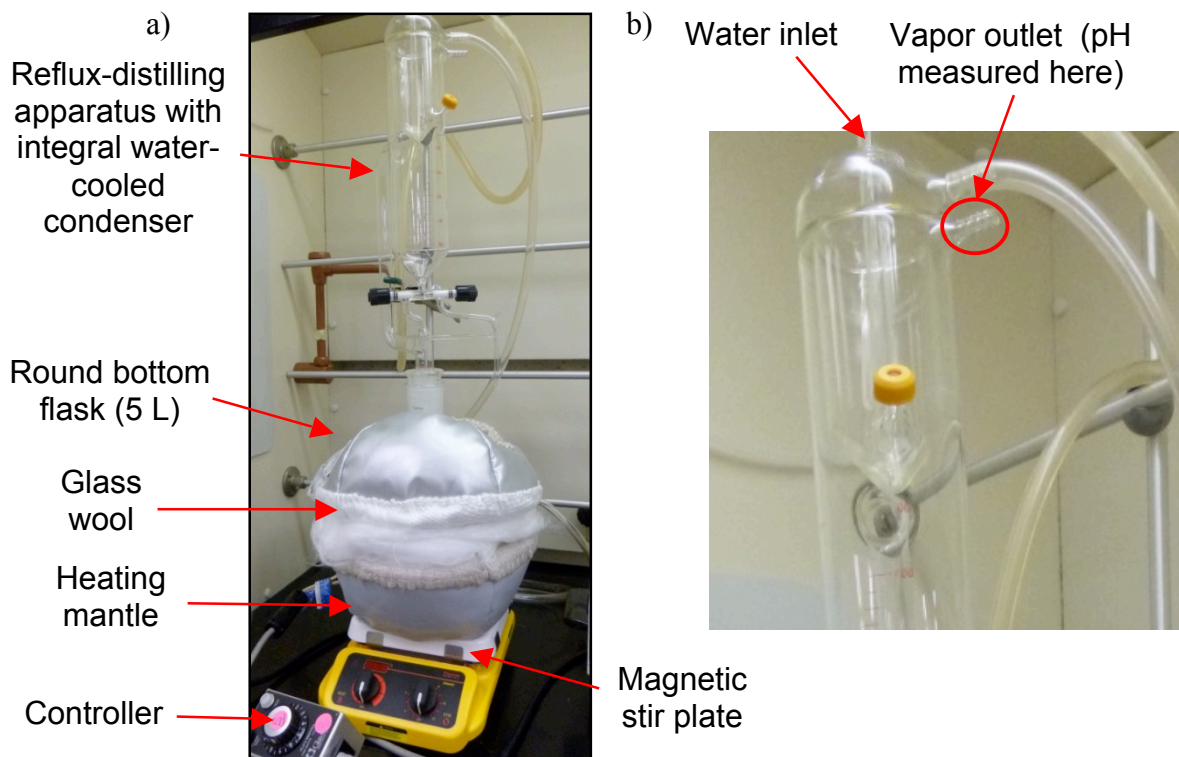


Fig. 2: Current refluxing setup. a) A complex apparatus including specialized glassware, a controlled heat source, and cooling water is necessary for refluxing. b) The distilling head includes an integral water-cooled condenser that returns the solvent (ethanol) back into the solution. The pH is measured at the vapor outlet.

In previous work, a gas purging process was developed to simplify ammonia removal and eliminate the need for a heat source [1]. The setup consists of a three-necked round-bottom flask,

an addition funnel, a magnetic stirrer, a condenser, and a gas dispersion tube with a coarse (12C) glass frit at the end (Fig. 3). Inert nitrogen gas is dispersed into the solution through the coarse glass frit to displace the ammonia within the sol-gel. The rate of ammonia loss is monitored using moistened pH paper at the vapor outlet of the condenser until a pH value of 7 is reached. The addition funnel is used to maintain the initial solution volume by adding ethanol back into the solution, while the condenser prevents too much ethanol from evaporating. This process was initially tested on a small scale with 200 mL ethanol and ammonium hydroxide solutions to determine the optimal nitrogen gas pressure and flow rate. The process was then tested with sol-gel, which yielded a similar purge time.

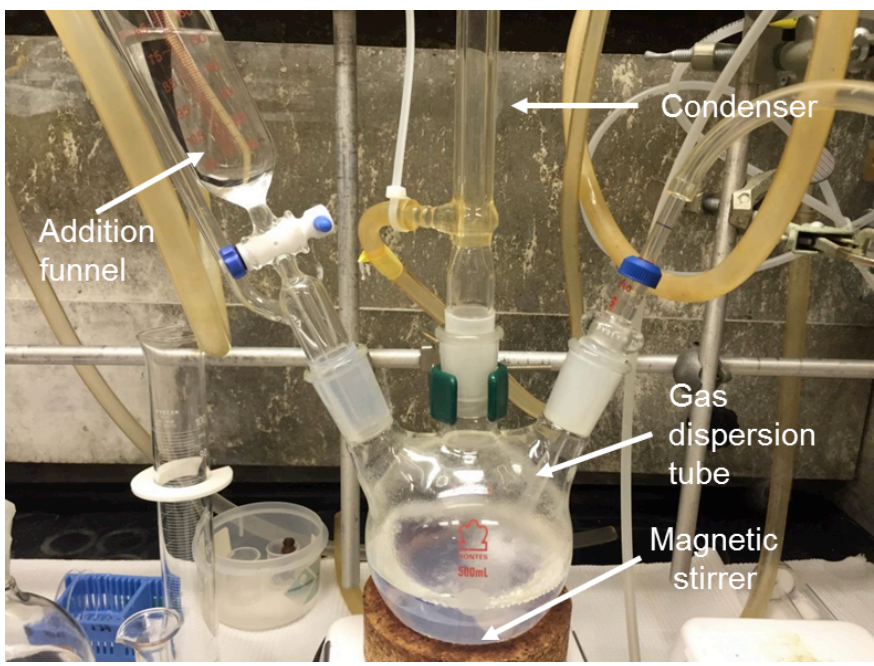


Fig. 3: Initial inert gas purging setup. A three-neck round-bottom flask was used for a small-scale prototype where nitrogen was dispersed into solution to displace the ammonia [1].

Anti-reflective coatings produced from the small-scale nitrogen-purged sol-gel solutions exhibited similar transmission and laser damage resistance to those produced by the reflux process [2][3]. At 351 nm, which is the wavelength for OMEGA and OMEGA EP, refluxed and nitrogen-purged single-sided anti-reflective coatings (non-optimized) yielded similar percent

transmittances (Fig. 4). Laser damage testing was conducted on the coatings at 351 nm using 1-on-1 and N-on-1 protocols with a 1 ns pulse width [3]. One-on-one testing involves the irradiation of different sites with single laser shots with an incremental increase in laser fluence until damage is observed, while N-on-1 testing involves the irradiation of a single site with an incremental increase in laser fluence until damage is observed. Table 1 compares the damage thresholds for refluxed and nitrogen-purged anti-reflective coatings. N-on-1 and 1-on-1 testing yielded similar laser damage resistances between the two types of AR coatings.

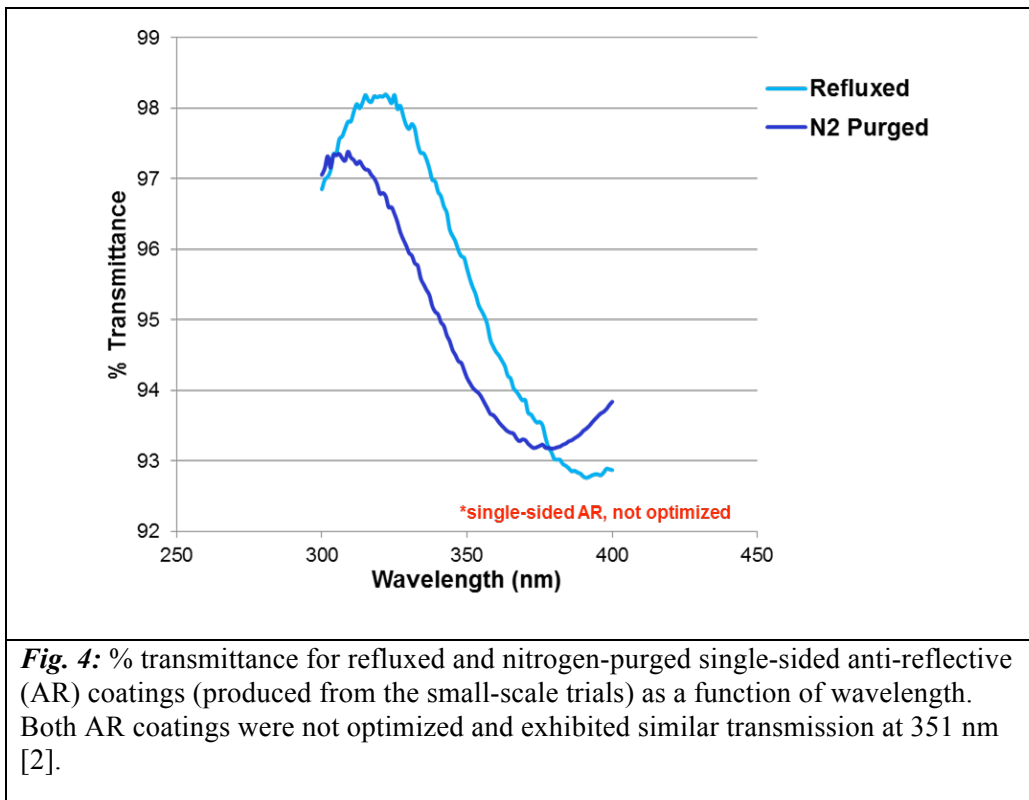


Table 1: Laser damage testing results for refluxed and N₂-purged single-sided AR coatings (produced from the small-scale trials) at 351 nm with a 1 ns pulse width [3].

Damage Testing Type	Refluxed	N ₂ -purged
1-on-1	8.65 ± 0.18	8.53 ± 0.09
N-on-1	15.77 ± 1.35	17.31 ± 0.40

In this work, three production scale experiments were performed in order to optimize the inert gas purging process. The first two experiments used ethanol and ammonium hydroxide solution, and the third experiment used sol-gel solution. The first experiment tested the effect of inert gas flow rate on ammonia removal time and ethanol loss. Nitrogen gas was used for the experiment, and two trials were performed: one with a flow rate of 2 L/min and one with a flow rate of 4 L/min. The second experiment assessed whether nitrogen, argon, or helium was most effective at removing ammonia from solution. A flow rate of 4 L/min was used for all three trials, and ammonia removal time and ethanol loss were recorded at the end of each trial. The third experiment demonstrated the inert gas purging process in sol-gel solution using nitrogen gas and helium gas. These experiments are vital in enabling the inert-gas purging process to replace refluxing.

2. Experimental

The inert-gas purging process was tested at production volume (2.5 L) in a simple glassware setup (Fig. 5) using ethanol and ammonium hydroxide. Rather than a three-necked round-bottom flask, a 4 L Erlenmeyer flask was used to assess the efficiency of the process with a different flask geometry. This also removes the need to transfer large solution volumes between storage vessels and the purging apparatus because sol-gel solution is generally produced in Erlenmeyer flasks. Flexible extension tubes were used to route the inert gas into the solution. The tubes were zip-tied together to prevent gas leakages. This series of tubes was then connected to a stiff extension tube, which was zip-tied to a gas dispersion tube with a coarse (12C) glass frit at the end. The stiff tube allows the frit to reach the bottom of the flask, so the gas can be evenly distributed. To maintain constant stirring at 240 rpm, a large magnetic stir bar and stir plate were used. The gas pressure was measured by a pressure gauge, and a Dwyer flowmeter with a range

of 1-10 L/min of air was used to control the gas flow rate. For the trials involving nitrogen, the gas was routed from the nitrogen source that is connected to the fume hood. For the trials involving argon and helium, the gas was routed from high-pressure gas cylinders through two-stage gas regulators, which were used to set the argon and helium gas delivery pressures. Three experiments were performed: the first testing the optimal flow rate, the second testing whether nitrogen, argon, or helium had the most efficient ammonia removal rate, and the third testing inert gas purging in sol-gel solution.

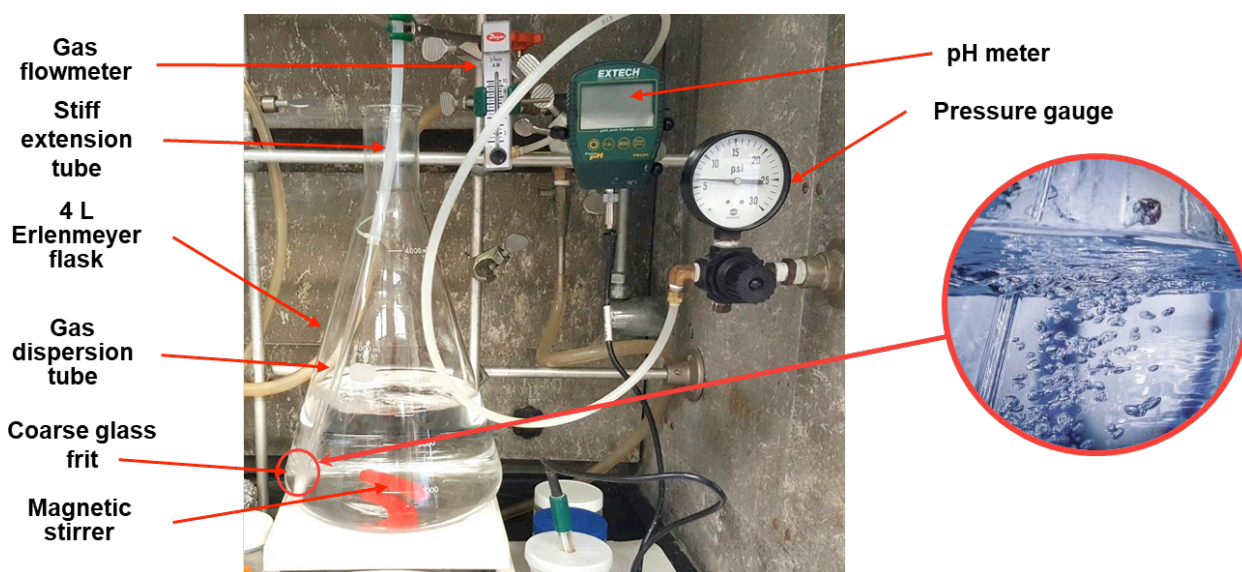


Fig. 5: Production-scale gas purging setup with a solution of ammonium hydroxide and ethanol. Gas is dispersed into solution by a coarse glass frit that creates bubbles that help displace the ammonia gas. This figure shows the purging setup used for nitrogen.

2.1 Effect of flow rate

The first two production-scale trials were performed with nitrogen gas at flow rates of 2 L/min and 4 L/min. Since nitrogen makes up the majority of air, it was treated as air when setting the flow rates with the Dwyer flowmeter. Ethanol (2430 mL) and ammonium hydroxide (70 mL) were used in both trials. The gas pressure was set so the pressure gauge inside the fume hood read 7 psi, before turning the flow meter on. A line was marked on the outside of the flask to indicate the initial solution level before purging was started. No measures were taken to prevent

ethanol loss (no condenser was used), and ethanol was added using a graduated cylinder at regular time intervals to maintain the initial solution volume. The pH was measured from an inch below the opening of the flask with both a pH meter and pH paper. There seemed to be a disparity between the values shown by the pH meter and the pH paper, possibly due to a slight calibration error in the pH meter. The pH paper seemed to more accurately measure the rate of ammonia loss, but since it measures only in integer values, the pH meter values were used for graphing the results to show the rate of ammonia loss. Each trial was stopped once a pH of 7 was reached according to the pH paper.

2.2 Choice of inert gas

Other inert gases were evaluated for their ability to remove ammonia from sol-gel solution. Solubility and viscosity properties of three gases were compared to that of ammonia to hypothesize which gas would be the most viable candidate. Argon and nitrogen gas both have a high solubility in comparison to ammonia, which indicates that they would displace the ammonia catalyst more readily than those with a lower solubility (Table 2). Nitrogen seemed to be the most viable candidate because of its high solubility and moderate viscosity. Although helium gas has a lower solubility, this property would make it the easiest to remove from solution, which is why the gas was still tested in the production-scale experiments.

Gas	Solubility in Ethanol (cm ³ /kg)	Viscosity (10 ⁻⁵ Pa*s)
He	38.4	1.96
Ar	309.7	2.23
N ₂	393.7	1.76
NH ₃	87.8	0.99

Table 2: Solubility in ethanol and viscosity for helium, argon, and nitrogen in comparison to ammonia [4][5]. These inert gases were evaluated for their ability to remove ammonia from sol-gel solution based on their chemical properties.

Nitrogen, helium, and argon were used for purging tests in ethanol and ammonium hydroxide solution. Ethanol (2430 mL) and ammonium hydroxide (70 mL) were used for all three trials. The desired flow rate for each gas was 4 L/min, but since the Dwyer flowmeter measures the flow rate of air, a correction factor was applied to calibrate the gas flow rates in terms of air. The correction factor was multiplied by the desired flow rate (4 L/min) to get the air equivalent [6]. Argon's correction factor is 1.18 [6], which yielded a flow rate of 4.72 L/min of air. The gas regulator was set to approximately 2.1 psi for the argon trial. For helium, the correction factor is 0.37 [6], which yielded a flow rate of 1.48 L/min of air. The gas regulator was once again set to 2.1 psi for the helium trial.

2.3 Application to sol-gel solution

The purging process was applied to a 2.5 L previously made sol-gel batch using nitrogen at a 4 L/min flow rate. Since the ammonia catalyst had already been removed from this sol-gel, 72 mL of ammonium hydroxide was added to the 2.5 L of sol-gel. The nitrogen pressure was once again set to 7 psi. Helium was also tested using a 2.5 L sol-gel batch and 72 mL of ammonium hydroxide at the calibrated flow rate for helium, and the pressure was set to 2.1 psi.

3. Results and Discussion

3.1 Effect of flow rate

Figure 6a illustrates the effect of gas flow rate on ammonia removal time in ethanol and ammonium hydroxide solution for nitrogen gas. When the flow rate was doubled from 2 L/min to 4 L/min, the purge time was cut approximately in half, from 43.5 hours to 23 hours.

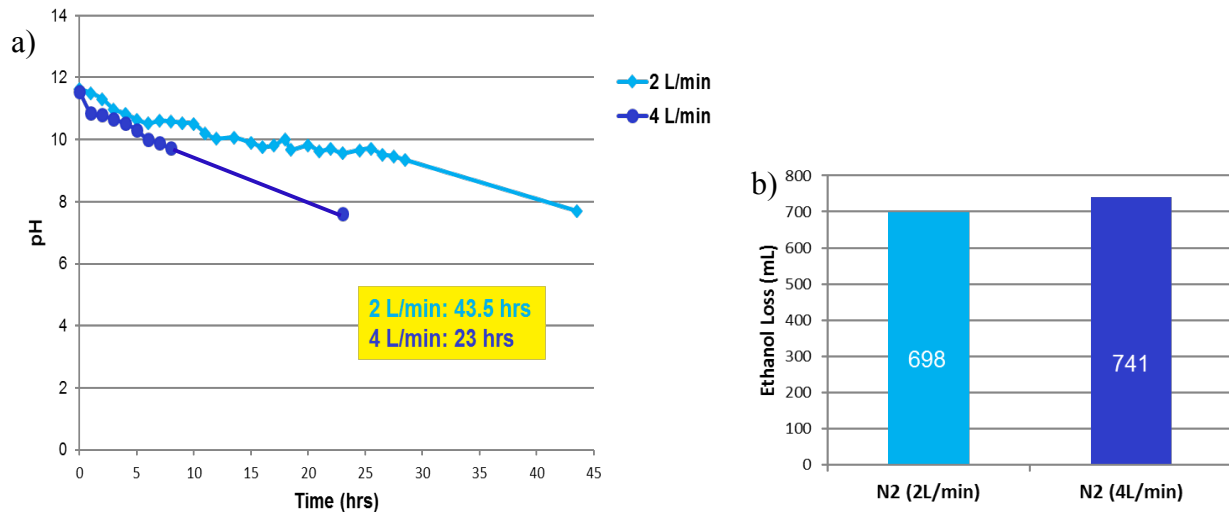


Fig. 6: a) pH as a function of time for nitrogen purging in ethanol and ammonium hydroxide solution at 2 L/min and 4 L/min. Doubling the flow rate cut the ammonia removal time in half. b) Total ethanol loss for nitrogen purging at 2 L/min and 4 L/min. The ethanol loss was not significantly affected when the flow rate was doubled.

The ethanol loss for the 2 L/min trial was 698 mL (27.9% loss), while the loss for the 4 L/min trial was 741 mL (29.6%) (Fig. 6b). This is not a significant difference, which indicates that 4 L/min is a more optimal flow rate than 2 L/min.

3.2 Choice of inert gas

Nitrogen, helium, and argon performed similarly in removing ammonia from the ethanol solution at a gas flow rate of 4 L/min. There was no significant difference between the purge times of the three gases, as the data only ranged from 23-26.5 hours (Fig. 7a). In terms of ethanol loss, argon performed better than the other two gases, with an ethanol loss of 532 mL (20.9%), compared to 741 mL (29.6%) for nitrogen and 664 mL (26.6%) for helium (Fig. 7b). The cause for the differences in ethanol loss seems to follow the patterns illustrated by the gases' viscosity properties. Argon has the highest viscosity at 2.23 [5] and the least ethanol loss, while nitrogen has the lowest viscosity at 1.76 [5] and the greatest ethanol loss. However, the ethanol loss results do not correlate with the solubility data for each gas. More trials will have to be performed to confirm whether argon has significantly lower ethanol loss.

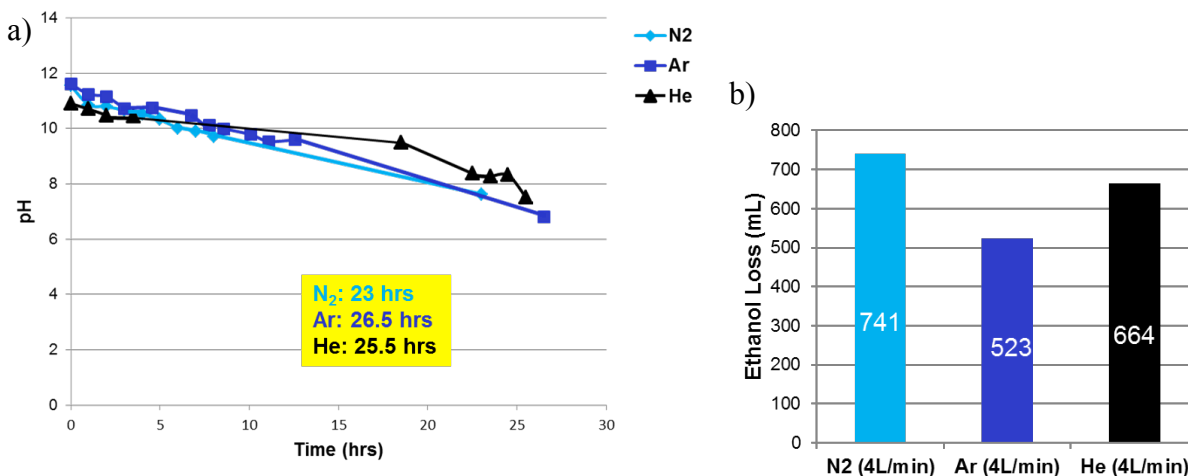


Fig. 7: a) pH as a function of time for nitrogen, argon, and helium purging in ethanol and ammonium hydroxide solution at 4 L/min. All three gases had similar ammonia removal rates. b) Ethanol loss for nitrogen, argon, and helium purging at 4 L/min. Argon had the least ethanol loss even with the greatest ammonia removal time.

3.3 Application to sol-gel solution

Conditions were controlled so that the nitrogen and helium purging trials with sol-gel batches could be compared to the trials with ethanol and ammonium hydroxide solutions. Helium took longer than nitrogen, with complete ammonia removal occurring after 47.8 hours in comparison to 42.75 hours (Fig. 8). However, helium's ethanol loss was less than nitrogen's, only 35.6% compared to 44.3% (Fig. 8). For both nitrogen and helium, the purge times for the sol-gel solutions were almost double those for the ethanol and ammonium hydroxide solutions. This is most likely because ammonia became trapped in the porous structure of sol-gel, making it harder to purge out. The ethanol loss was also greater for both sol-gel trials, because their purge times were two times longer.

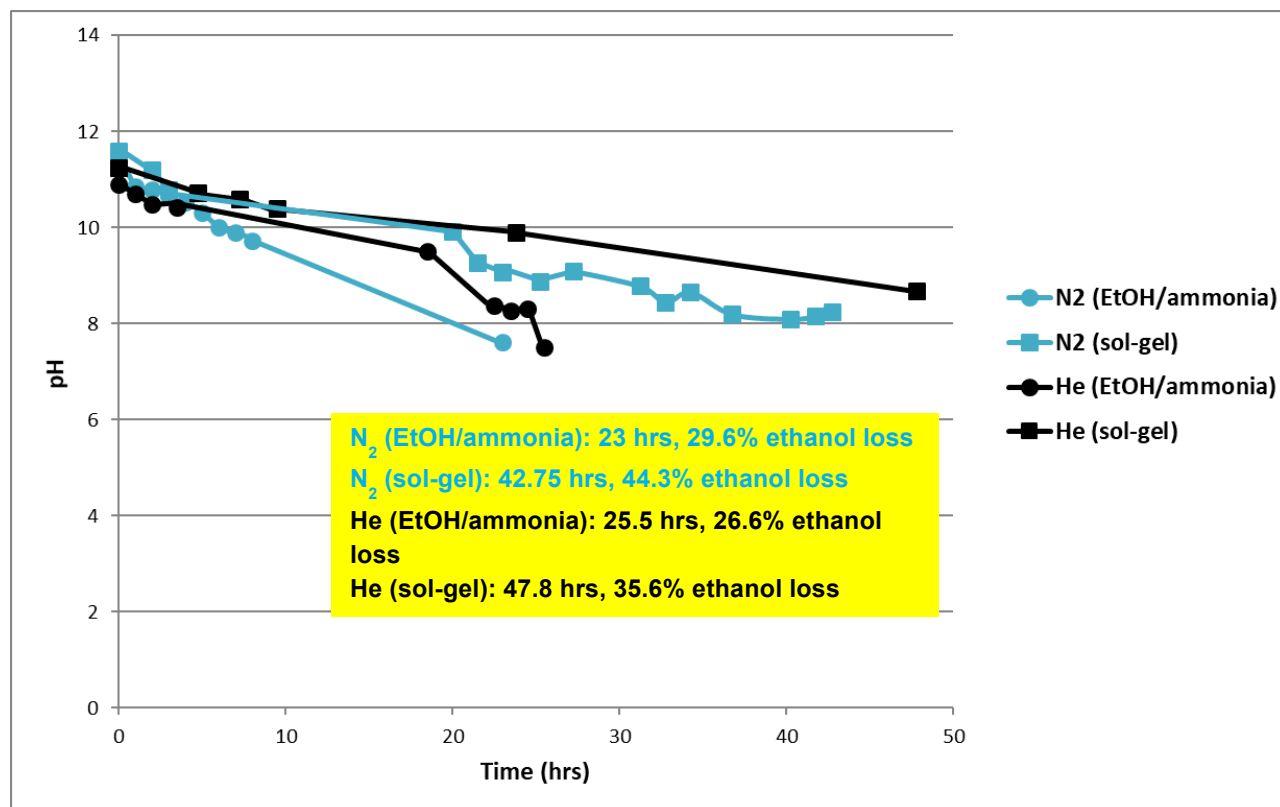


Fig. 8: Nitrogen and helium purging in a solution of ethanol and ammonium hydroxide compared to purging in sol-gel. The ammonia removal time doubled for purging in sol-gel for both gases.

4. Conclusions

A simplified inert-gas purging setup streamlines ammonia removal for sol-gel coating solutions. Nitrogen, helium, and argon were tested to see if one inert gas would outperform the others, but all three gases had similar purge times. Nitrogen is generally the most abundant gas in laboratories and is the easiest to handle, therefore making it the most convenient and lowest-cost option. The inert-gas purging process can be successfully applied to production-scale sol-gel batches using nitrogen gas at a purge rate of 4 L/min. As a result of the simplicity of the inert-gas purging setup, 4-5 apparatuses can be setup in one fume hood. Using refluxing, only 2 apparatuses can be set up within one fume hood. Inert-gas purging requires little equipment compared to refluxing and can process 2.5 L of sol-gel per setup. Therefore, this new process

would allow for 2-3x the volume of sol-gel solution to be processed in 24-43 hours with significantly less effort than by refluxing.

5. Future Work

Additional studies remain before the gas purging process can be validated for sol-gel coating production. Further trials should be conducted using condensers with closed-loop, Freon-based refrigeration cooling to minimize solvent loss. Although ethanol will still have to be added to maintain the original solution volume, resource costs will be reduced if a more efficient setup is created. Any other alterations to the design that can increase the efficiency of the process should be analyzed. Different glass frit porosities, such as an extra-coarse frit, could decrease the ammonia removal time at a given flow rate. Alternative flask geometries could have an effect on the purge rate or the distribution of the inert gas in the solution. Laser damage testing and AR coating quality testing should be determined for a gas-purged, production-scale sol-gel coating batch to be compared to the small-scale trial damage thresholds obtained from previous work. The sol-gel coating batch will likely be purged with nitrogen gas, because helium and argon did not perform significantly better in the trials. The resulting solution will be dip-coated onto a glass optic for testing. If the laser damage threshold is high enough, a production-scale, nitrogen-purged sol-gel AR coated optic should be tested on OMEGA.

6. Acknowledgements

I thank Dr. Stephen Craxton for giving me the opportunity to participate in this amazing program and conduct fascinating research at the University of Rochester Laboratory for Laser Energetics. I am grateful to my advisor, Mr. Kenneth Marshall, for patiently guiding me through laboratory procedures and helping me run my experiments successfully. I also thank Joann Starowitz for helping me with equipment and being an extremely helpful source of information

regarding refluxing. Finally, I thank all of the Materials Lab staff and students for being so welcoming and making my experience enriching and enjoyable.

7. References

- [1] Brendan Coli, "Nitrogen Bubbling Project Description," LLE, May 11, 2016
- [2] Brendan Coli, "Reflux vs. N₂ Purged," LLE, August 3, 2015
- [3] Semyon Papernov, LLE, private communication
- [4] "IUPAC Solubility Data Series," Office of Data and Informatics of the National Institute of Standards and Technology (NIST) Material Measurement Laboratory (MML), February 18, 2015, <https://srdata.nist.gov/solubility/IUPAC/iupac.aspx#vol1.htm>
- [5] "Absolute Viscosities of Gases," The Engineering Toolbox, https://www.engineeringtoolbox.com/gases-absolute-dynamic-viscosity-d_1888.html
- [6] "Basic Flowmeter Principles," <https://www.mathesongas.com/pdfs/products/flowmeter-product-line-overview.pdf>

Modifying Stainless Steel Surfaces by Electropolishing

Arian Nadjimzadah

Brighton High School

LLE Advisor: Dr. Walter Shmayda

Laboratory for Laser Energetics

University of Rochester

Summer High School Research Program 2017

Abstract

Tritium ingress into stainless steel depends on the surface characteristics of the metal. Electropolishing provides a flexible and controllable method of modifying a metal surface by reducing the surface roughness. A program has been implemented to study the dependence of surface roughness on electrolytic current density, voltage, electrolyte composition, polishing time and operating conditions such as temperature and stir rate. Multiple plots of current density versus potential have been generated at different temperatures as a first step in establishing the appropriate operating electrolytic conditions for a given operating situation. A variety of operating conditions have been tested to obtain a smoother surface and to mitigate surface thickness loss. The precise formation of a viscous layer and the control of gas evolution on the surface have been paramount in developing a macroscopically and microscopically smoother finish.

1. Introduction

Substantial work at LLE has been done to study tritium ingress into stainless steel. Specifically, the tritium and stainless steel interactions studied by Shmayda et al. [1] at LLE are dependent on the surface characteristics of the stainless steel sample. Because of this, stainless steel samples have been sent out to a third party to be electropolished. Unfortunately, the quality of these electropolished samples is somewhat questionable. In this work, the mechanism and operating conditions of electropolishing were studied and progress was made toward optimization.

2. Theory

2.1. Electropolishing on Microscale

Electropolishing works on the basis of an electrolytic cell, as shown in Fig. 1, which summarizes the fundamental chemical processes involved in electropolishing. This consists of a source of electrical potential connected to two electrodes. The electrode located at the deficit region of electrons is known as the anode, and the electrode at the excess region of electrons is known as the cathode. An electrolyte solution is present between the anode and the cathode. This solution is necessary to transfer charge through the solution between the anode and the cathode, which is achieved through the movement of ions in solution. The fundamental principle that drives the cell is the oxidation-reduction reaction. At the anode, oxidation occurs, which results in the dissolution of metals into their constituent ions. Water is also oxidized, evolving oxygen. At the

cathode, reduction occurs, which results in the deposition of metal ions. Water is reduced, which evolves hydrogen. The overall result is a net reduction in anodic mass proportional to the charge applied, which can be quantified by Faraday's Law of Electrolysis:

$$m = \left(\frac{Q}{F}\right) \left(\frac{M}{z}\right) \quad (1)$$

where m is the mass lost, Q is the total electric charge passed through the anode, F is Faraday's constant, M is the molar mass of the anode, and z is the valency of ions of the substance (the number of electrons transferred per ion).

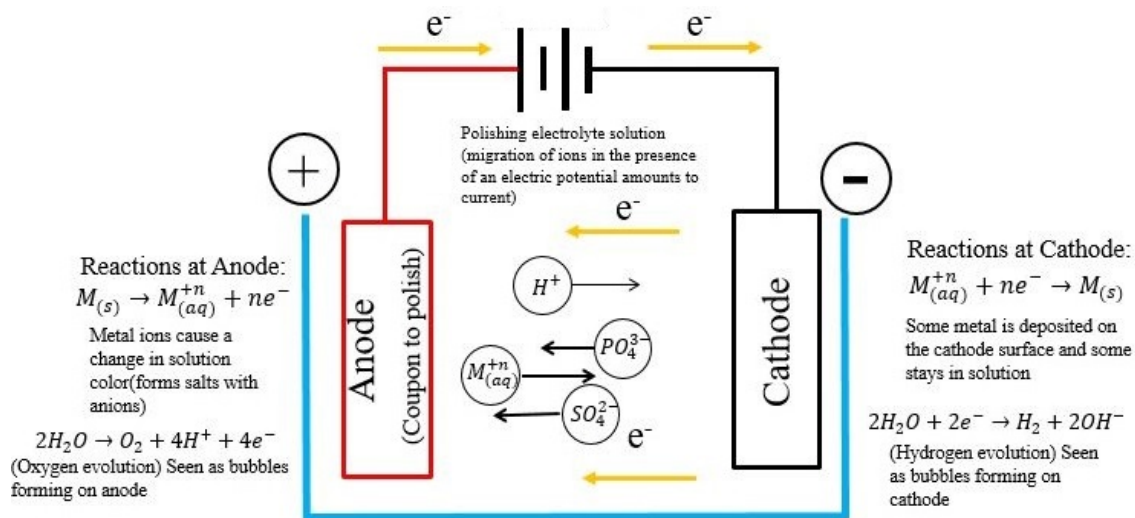


Figure 1: Electrochemical process on microscale. Illustration includes a sulphuric and phosphoric acid electrolyte. Note that a variety of other electrolytes can be used.

2.2. The Viscous Layer and Mass Transfer Mechanism

The chemical reactions detailed above on a large scale are responsible for the mechanism of electropolishing. As metal ions dissolve from the anode surface due to the potential difference, they form a viscous layer which limits the current where the surface concentration is greater than that of the bulk solution. Fig. 2 shows a simplified model of the viscous layer and mass transfer mechanism. According to some theories, the surface metal ion concentration is equal to the saturation concentration, decreasing as the distance from the anode increases [2]. The thickness of this more concentrated metal ion layer is greater in the valleys of the anode than over the peaks.

This results in a lower dissolution in the depressions, because the layer above the surface is already at maximum ion concentration, keeping more dissolution from occurring. Additionally, the thicker viscous layer over the valleys results in an increased resistance, decreasing the current by Ohm's Law. As a consequence of Gauss's Law, electric fields tend to concentrate around peaks, so the current density and dissolution around these regions will increase. All of these factors result in a net leveling of the surface, and a visibly "polished" surface.

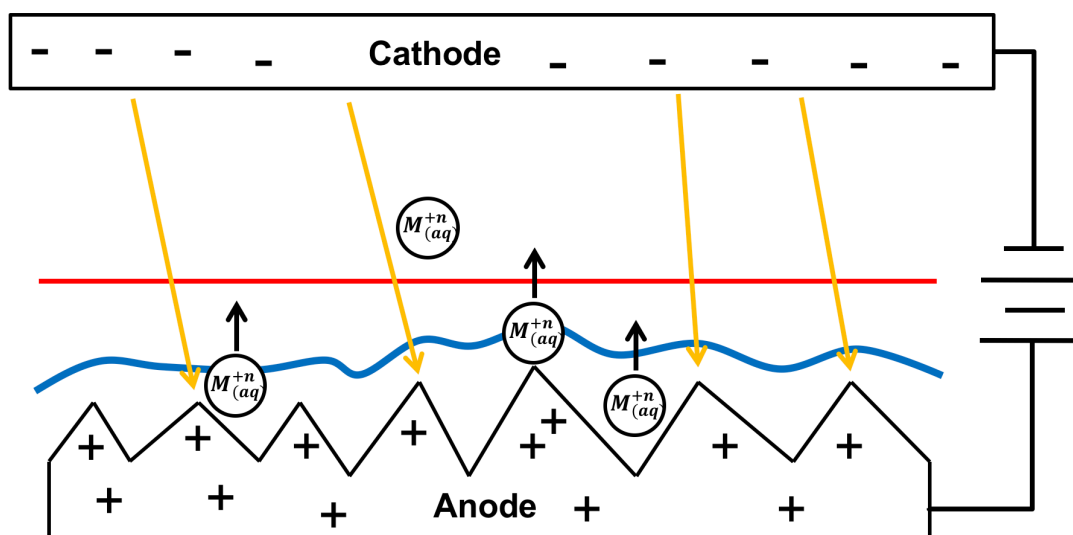


Figure 2: Electrochemical process on macroscale. The viscous layer is represented by the region between the blue curve and the anode surface. The directions in which electrons feel a force concentrated around peaks are illustrated by the yellow arrows. The red line represents the interface between the bulk (above the line) and surface (below the line) electrolyte.

2.3. The Anodic Polarization Curve

Fig. 3 shows the general current density and voltage relationship for an anode in the electropolishing process. The plot of this relationship is known as an anodic polarization curve. Due to the special conditions present at the anode, namely the viscous layer, the polarization curves at the anode and cathode are not identical, so the curve must be specified as "anodic". The current density increases with applied voltage in region I. In region II, however, the current density drops due to the formation of the viscous layer, and plateaus (where it is known as the limiting current density) in region III, the optimal polishing region. The viscous layer then dissolves in region IV,

and current density continues to increase with applied voltage. In this region, significant pitting of the surface occurs. Beyond region IV (not depicted in Fig. 3), the rate of dissolution increases rapidly, and pitting of the surface becomes minimal. Here, polishing can be achieved, but minimizing mass loss on the anode is sacrificed.

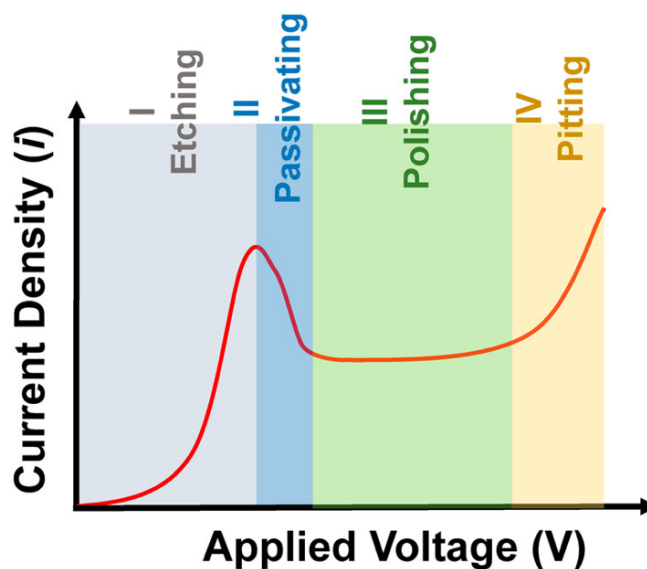


Figure 3: Simplified theoretical Anodic Polarization Curve relating Current Density and Applied Voltage as applied to electropolishing [2]

3. Experimental

3.1. Apparatus Configuration

A system was designed to contain, initiate, and monitor the electrochemical reaction of interest in this experiment—electropolishing. The system consists of two main components: the electrolytic cell (the vessel in which the reaction takes place) and a monitoring and power supply system.

3.1.1. Electrolytic Cell

The electrolytic cell consists of a source of electrical potential difference, an anode and cathode, and an electrolyte through which current can flow. Fig. 4 shows a simplified illustration of the electrolytic cell.

A Teflon block firmly holds two stainless steel counter electrodes and a “claw” like construction holds the sample (coupon) to be electropolished. This unit is then affixed to a vertical metal rod by means of a clamp. The metal rod is conveniently attached to a heated stir plate. The vessel used to hold the electrolyte is a 400 mL beaker containing a stir bar to agitate the solution. This beaker is immersed in a larger beaker filled with water to regulate and mitigate fluctuations in temperature. The aforementioned electrode construction is suspended directly over the 400 mL beaker, so that when an experiment begins it can be lowered into the electrolyte, immersing the electrodes. The electrolyte used during the course of this experiment was composed of 56.7% phosphoric acid, 32% sulphuric acid, and 11.3% water.

3.1.2. Monitoring and Power Supply System

The other main component of the apparatus is the data collection and power supply center. This equipment sits on a cart that can be connected to and disconnected from the reaction vessel through a bundle of wires. This ensures that the data acquisition equipment is a safe distance from the electrochemical reaction, and it allows it to be mobile.

The cart consists of a computer on the top shelf, which is equipped with a LabView program to receive data from the experiment and to trigger the power supply. Fig. 5 shows the program display, where the user inputs the experimental parameters and receives real-time data. On the second shelf, there are a power supply, a multimeter, and a National Instruments DAQ (data acquisition) terminal containing three modules: an electromechanical relay, voltage input, and thermocouple input.

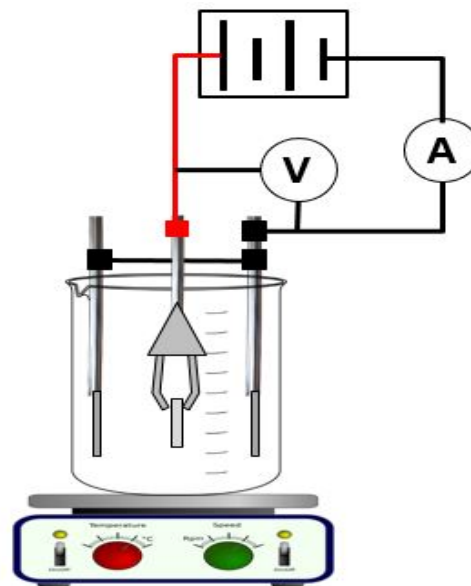


Figure 4: Electrolytic cell illustration. The center anode clip suspends the coupon and is equally spaced between and parallel to the two stainless steel cathode plates. The ammeter and voltmeter are also shown. The water bath immersing the beaker shown and thermocouple have been omitted for clarity.

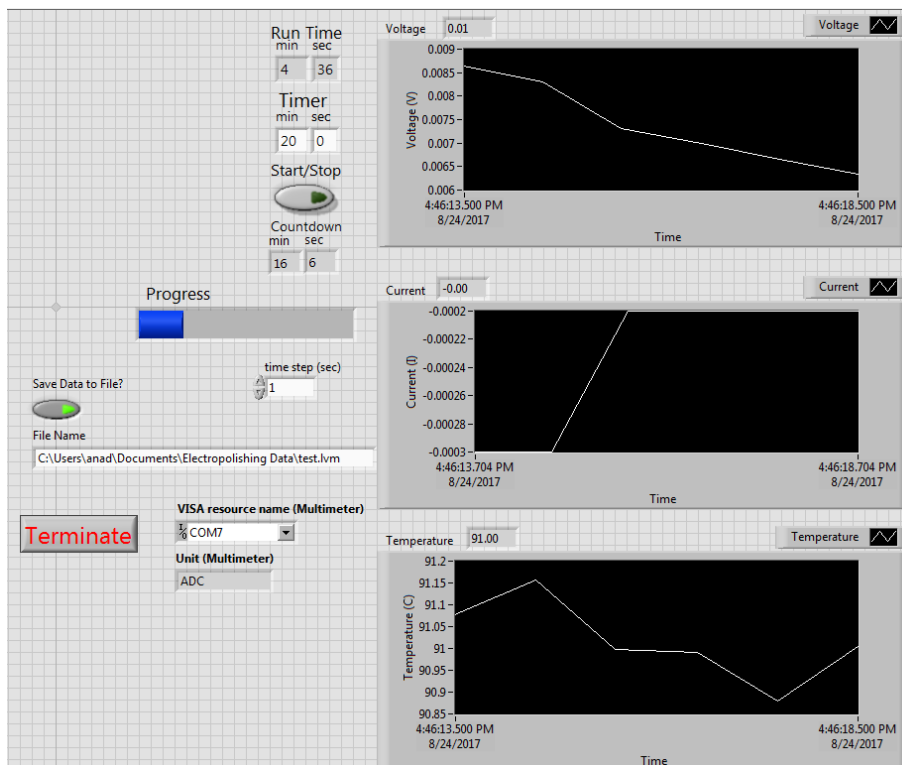


Figure 5: LabView Front Panel. The voltage, current, and temperature readings are updated in real-time. The experimental data is automatically exported and saved to a file.

The multimeter and DAQ terminal are attached to the computer through a USB connection, so that data can be transferred. One end of a pair of wires is attached to the remote control circuit of the power supply, and the other end is attached to the electromechanical relay. When the relay is turned off, an open circuit is created, preventing the power supply from outputting any current, and when the relay is on, a short circuit is created, allowing the power supply to output current.

The power supply, current and voltage monitors, and reaction vessel form a simple circuit shown in Fig. 6. Starting from the power supply output, the negative terminal is attached to the common ground of the multimeter through a wire. Since the multimeter is measuring current, it must be in series with the system. Another wire comes out of the multimeter and terminates at an alligator clip. At the positive terminal of the power supply, a wire extends and also terminates at an alligator clip. The DAQ voltage input module must be connected in parallel with the circuit. Therefore, its positive and negative wires are bundled with the wires coming from the power supply at the alligator clips. The electrolyte solution acts as the main resistor for this simple circuit,

so the alligator clips are attached to the electrodes. It is important to note that for electropolishing, the positive terminal must be attached to the coupon being polished, and the negative terminal to the counter electrode. The opposite is true for electroplating.

The final data analysis unit is the thermocouple module. The positive and negative terminals of the thermocouple DAQ unit are attached to the positive and negative wires of the thermocouple. The thermocouple, power supply, and voltmeter wires lead to the reaction vessel in the fume hood.

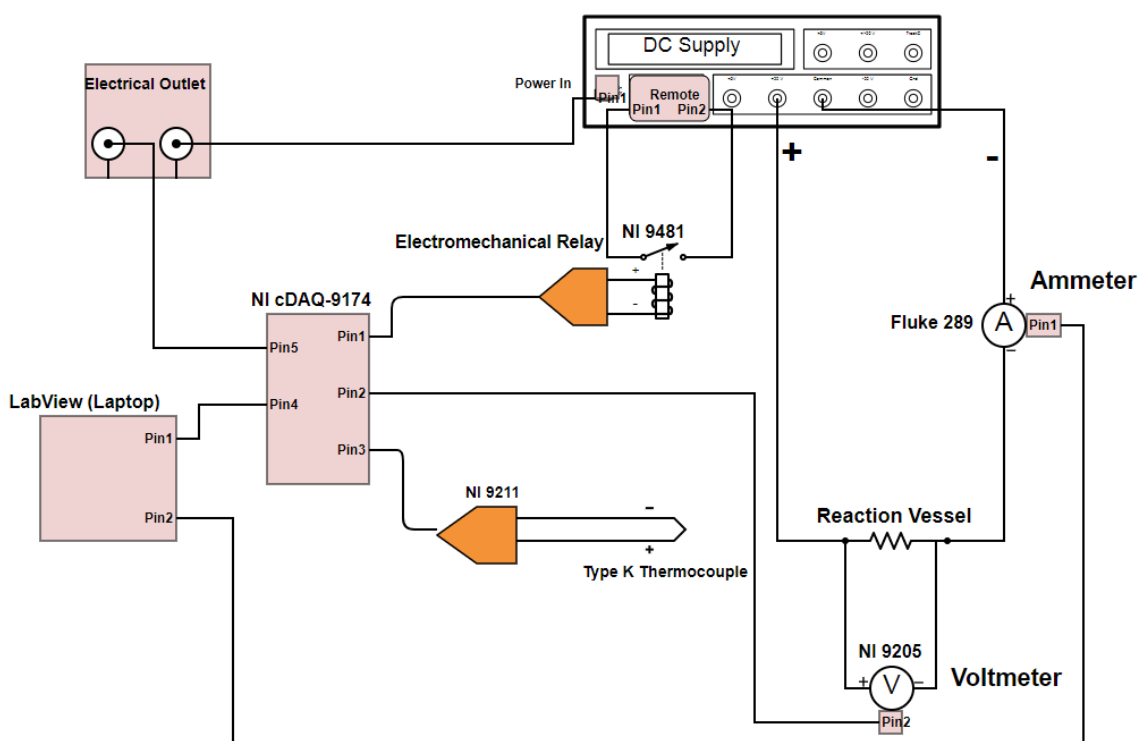


Figure 6: Electrical schematic of the electrolytic cell monitoring and power supply system

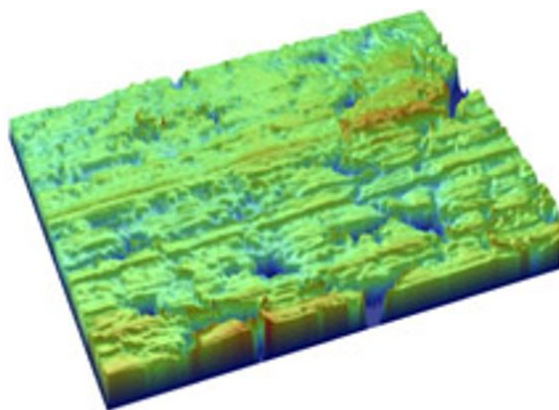
3.2. Electropolishing Procedure

3.2.1. Pretreatment

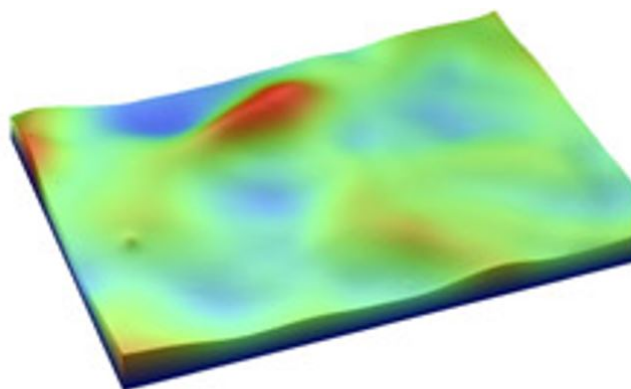
All electropolishing trials begin with the preliminary treatment and analysis of the coupons, which are approximately 16 mm by 20 mm by 3 mm 316 stainless steel samples. The initial step is to mechanically polish the coupons with a $\sim 5 \mu\text{m}$ diamond paste, and then a $0.3 \mu\text{m}$ alumina slurry, which is achieved by an outside company. Then, the coupons must be washed in a three-solvent ultrasonic bath with acetone, DI water, and isopropyl alcohol, in order to eliminate any oils and residues left from the mechanical polishing process.

3.2.2. Interferometry

The surfaces of coupons that are to be polished are analyzed thoroughly before and after polishing. The samples are analyzed with an interferometer, a device that takes a detailed three-dimensional surface scan and quantifies its characteristics. Two main surface metrics were chosen: root mean square surface slope (SDQ) and mean height (Sa). The mean height describes a surface's smoothness generally and is commonly seen in literature. The root mean square surface slope gives the mean slope of a sample, which is a more specific description of surface smoothness, as Fig. 7 illustrates. Each coupon was scanned at 40 equally spaced points over both faces and some representative images were saved.



Sa = 80nm, Sdq= 11.0°



Sa= 75nm, Sdq= 0.2°

Figure 7: A visibly rough surface on the left and a smooth surface on the right. Note that the Sa values are quite similar, whereas the SDQ values are significantly different.

3.2.3. Voltage Scans and Polarization Curve Production

A variety of voltage scans were conducted at a variety of temperatures to determine how the anodic polarization curves change. The curves were produced by first submersing the electrodes and coupon in the electrolyte and setting the voltage dial on the power supply to 0 V. Then, the program run time was set to an arbitrarily long duration. Once the power supply was switched on, the voltage was gradually increased until reaching approximately 4 V (the point at which little of note would be observed on the polarization curve). The data was exported to an Excel spreadsheet, and the surface area of the coupon was measured. With this information, the current density was calculated and plotted against voltage. Fig. 8 shows an example of a representative polarization curve produced as detailed above. The polarization curves produced were very close in shape to the theoretical model shown in Fig. 3. The optimal polishing voltage can be seen in the plateau region.

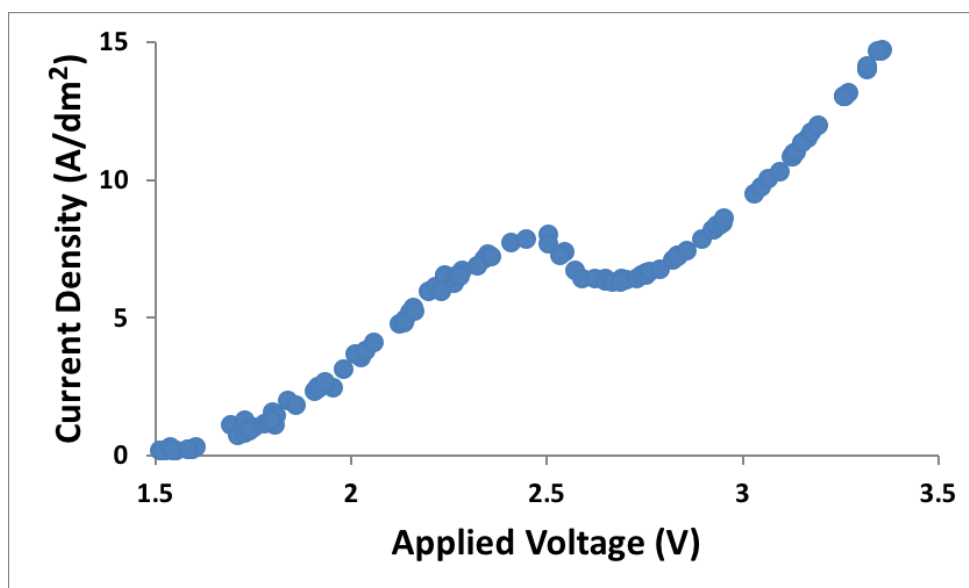


Figure 8: Representative experimentally determined anodic polarization curve with plateau between 2.6 V and 2.8 V. The plateau voltage tended to stay constant over a variety of operating conditions.

3.2.4. Polishing Runs

The mass of the coupon is measured on a scale precise to 10 μg before and after the polishing run. Before the coupon is electropolished, a test coupon is secured to the electrode holding apparatus. Due to the limitations of the power supply, the test coupon must first be submerged in the electrolyte to set the voltage for the trial. The above-mentioned alligator clips are attached to the two electrodes and the thermocouple is secured in the water bath. The multimeter is powered on, and the LabView program is started. The temperature is closely monitored, ensuring that it stays within one degree of the desired temperature. The power supply is then initiated, and the optimal voltage (determined by the location of the plateau on the anodic polarization curve) is set. The power supply is switched off, the desired run time is set in the program, the test coupon is switched out for the coupon to be polished, and the program is initiated, which turns on the power supply. Once the power supply automatically shuts off after the time set in the LabView program has elapsed, the coupon is removed from the corrosive electrolyte bath, and washed with acetone and DI water.

4. Results and Discussion

4.1. Temperature, Agitation Dependence, and the Viscous Layer

The limiting current density (the current density in the plateau region) is highly dependent on the electrolyte bath operating conditions, namely, temperature and solution agitation. The limiting current density i_L is given by [3]

$$i_L = \frac{nFD_0C}{\delta} \exp\left(-\frac{Q_a}{RT}\right) \quad (2)$$

where n is the molar of the total charge of ion involved, D_0 is the exponential pre-factor of the diffusion coefficient of the rate limiting species, C is the saturation concentration of metal ions, δ is the thickness of the viscous layer, Q_a is the activation energy for diffusion, R is the gas constant, and T is the absolute temperature. The viscous layer has been observed as a yellow film visible on the coupon surface during the electropolishing runs. It is expected that its thickness will decrease (decreasing δ) with an increasing bath stir rate, because the agitation will disrupt the layer. The temperature and agitation rate were tested against this theoretical model by generating multiple polarization curves. The limiting current densities of each of these polarization curves were found and plotted as shown in Fig. 9.

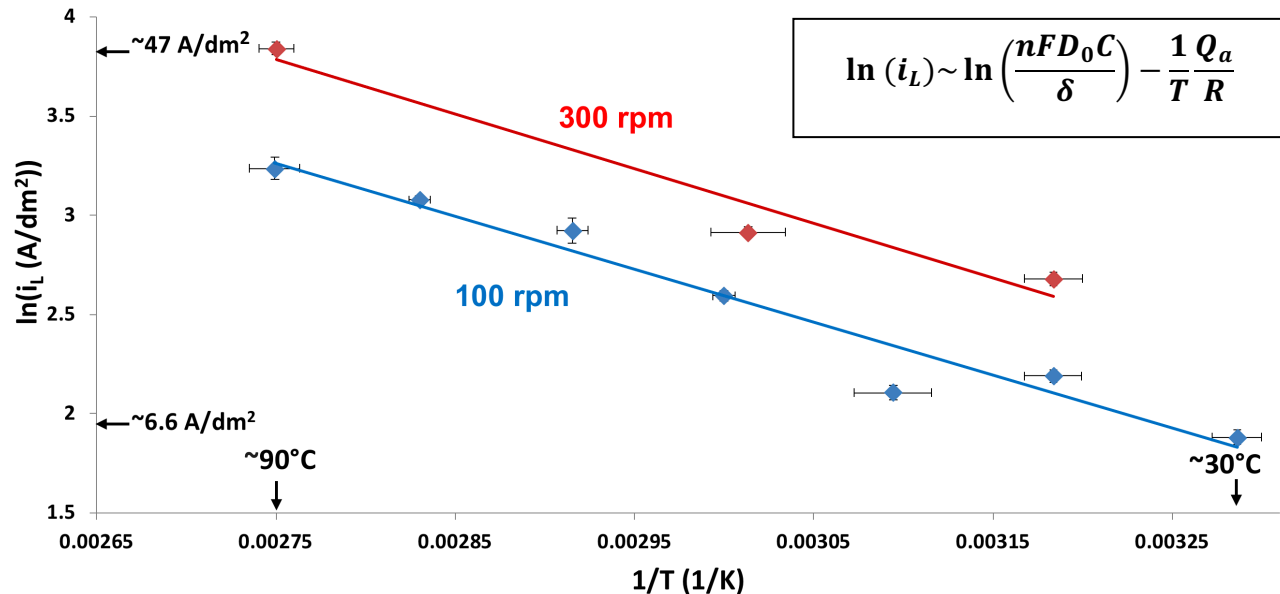


Figure 9: Natural logarithm of the limiting current density plotted against inverse temperature. Temperature and stir rate were varied and the limiting current density changed accordingly. As temperature increased, the limiting current density increased. As the stir rate was increased, the limiting current density also increased.

The linear fit for trials at a stir rate of 100 rpm is approximately parallel to that of trials at a stir rate of 300 rpm, confirming that the activation energy for diffusion is constant. The 300 rpm regression is shifted above the 100 rpm fit, implying that the terms in front of the exponential in equation 2 are greater. The terms n , D_0 , and C remain relatively constant for a given electrolyte and anode, leaving only δ , the thickness of the diffusion layer to vary. The data is consistent with equation 2, as the diffusion layer is visibly thinner at a higher stir rate, and the regression model confirms this. Agitation must be kept low enough in order to preserve the viscous layer, cited as being vital for optimal polishing.

4.2. Surface Deformities

Significant surface pitting has been observed on polished coupon samples, caused by the evolution of oxygen at the anode (the coupon) and hydrogen at the cathode, whose reactions are shown in Fig. 1. The plateau voltage is greater than the reversible potential for oxygen evolution, so oxygen bubbles form on the coupon surface. These bubbles disrupt the viscous layer, resulting in a localized attack of the metal surface [4]. This can be mitigated by the removal of those bubbles through the agitation of the solution. Another more significant

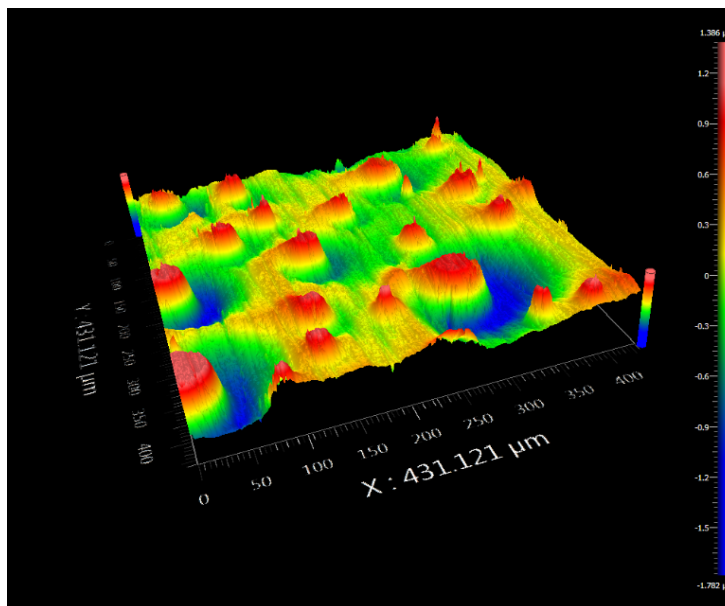


Figure 10: Example of pitting due to hydrogen bubbles. The sample was polished for 30 seconds at a stir rate of 300 rpm. Note the characteristic donut shaped pits. The colors represent surface deformations ranging from $-1.78 \mu\text{m}$ (blue) to $+1.39 \mu\text{m}$ (red).

problem is the evolution of hydrogen at the anode, which occurs at double the rate of oxygen evolution. This is a consequence of the equation for the electrolysis of water, where two moles of hydrogen gas are produced for every mole of oxygen gas. This relatively large amount of hydrogen bubbles disperses into the solution and can be deposited on the anode, due to solution agitation. Donut shaped pits were generated on the surface because of the occlusion of the surface below and increased attack in the surrounding regions [4]. Fig. 10 is an example of this type of pitting observed on multiple coupons. These pits, as opposed to those resulting from oxygen bubbling, can be prevented by reducing solution agitation. It follows that the stirring rate must be chosen very carefully in order to preserve the viscous layer, to prevent oxygen bubbling, and to prevent hydrogen bubbling.

4.3. Polishing above the Plateau

Although optimal polishing is cited to occur in the plateau region, noteworthy results can be obtained at higher voltages. Fig. 11 shows the effects of changing voltage on coupon surface finish.

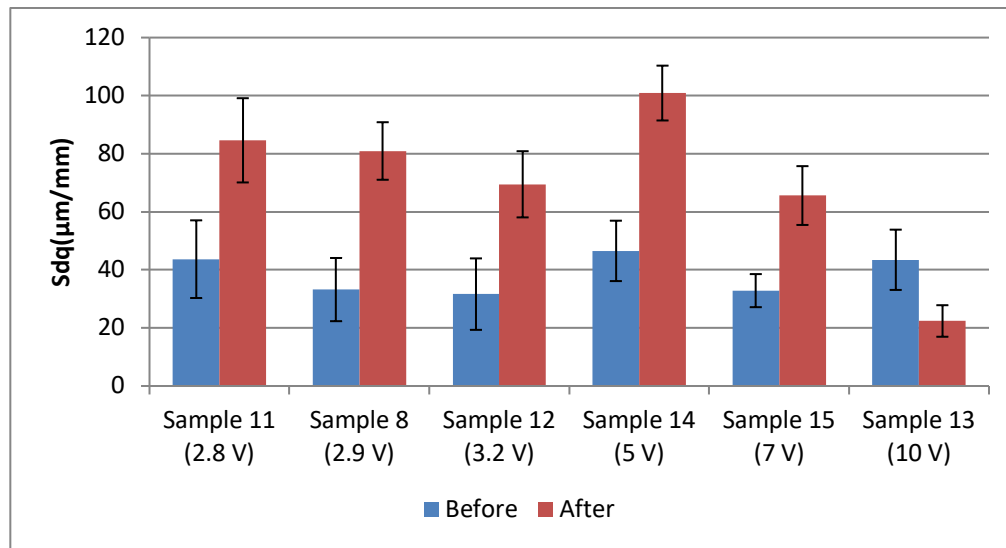


Figure 11: Root mean square surface slope on the Y axis and Voltage on the X axis before and after polishing. All samples polished at 21 C for 10 minutes. Note that the 10 V trial is the only one that saw a decrease in SDQ, and therefore a reduction in surface roughness. Here, SDQ is expressed as the tangent of the angle, as done commonly. An SDQ of 100 $\mu\text{m}/\text{mm}$ corresponds to an angle of 5.71°.

At all voltages between 2.8 V and 10 V (between the end of the optimal polishing region through region IV [see Fig. 3]), the surface finish worsens after polishing. The trial run at 10 V, however, results in a significant decrease in SDQ and a visibly more reflective surface. At this voltage, the viscous layer cannot form, so a high metal ion concentration gradient is not present at the surface of the coupon. Polishing beyond region IV (the 10 V trial is hypothesized to be in this range), as discussed in relation to Fig. 3, rapidly dissolves the metal surface. Dissolution occurs at approximately the same rate over the surface, which results in significant erosion. The results of polishing far beyond the plateau voltage can be seen in Fig. 12.

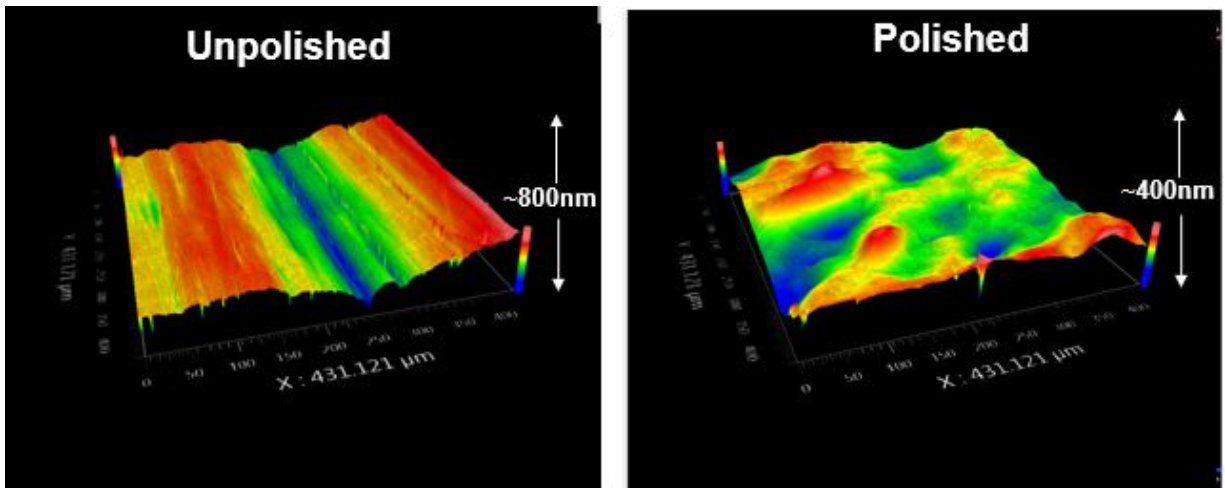


Figure 12: Unpolished coupon on the left. Sample polished for 30 minutes at 12V on the right. SDQ decreased 63.2%. Mass decreased 16%, and thickness decreased $179.3\mu\text{m}$. The optimal thickness loss for applications requiring tight-fitting machined components is $\sim 1\mu\text{m}$. The white arrows indicate the approximate range of surface deformities from peak to valley.

Polishing above the plateau for prolonged periods of time dramatically reduces the surface roughness. This however, comes with a drawback—a substantial amount of metal is removed from the coupon. The decrease in mass observed in the trial in Fig. 12 is unacceptable for applications requiring tight-fitting machined components.

4.4. The Loss of Material in Electropolishing

The loss of mass from a coupon during electropolishing is proportional to the amount of charge applied, the product of current and time. This is quantified by equation 1, Faraday's Law of Electrolysis. Fig. 13 shows a plot of the theoretical mass loss and actual mass loss as a function of applied charge.

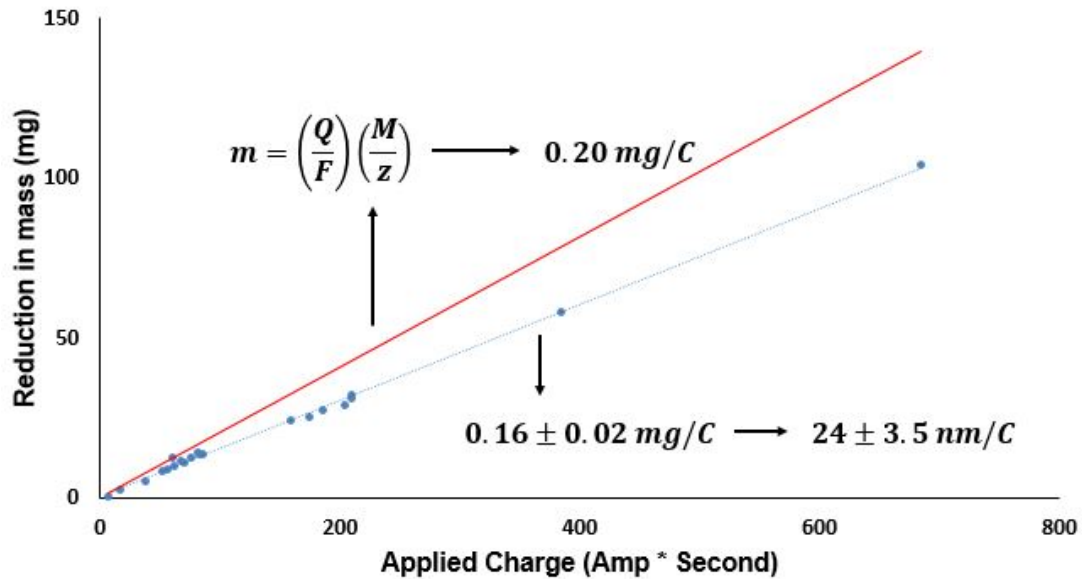


Figure 13: Mass reduction plotted against charge applied predicted by Faraday's Law of Electrolysis (red) and experimentally determined (blue). Appropriate values of M , molar mass of the metal, and z , valency of metal ions, were substituted into equation 1. The mass lost is 76% of that predicted by Faraday's Law. The thickness loss equivalent of $24 \pm 3.5 \text{ nm/C}$ was calculated by considering the density of the stainless steel and surface area of the coupons.

The actual reduction in mass is consistently proportional to the amount of charge applied. This provides a powerful predicting tool for applications in this experimental setup. A certain amount of material can be removed with relative precision, by supplying a known current (investigated in Fig. 9) for a certain amount of time.

5. Conclusion and Further Steps

The mechanism of electropolishing was investigated and theory was applied in order to probe the effect of operating conditions on surface finish. Electropolishing is a problem in optimization, so a careful balance must be found between operating parameters. Tradeoffs have to be made between surface roughness and the thickness removed, as they are inversely related. If too much charge is applied to the sample, its roughness will decrease significantly, but more material will be lost. If too little charge is applied, the roughness will not change significantly, but less material will be lost. Additionally, the stirring rate and temperature need to be carefully controlled in order to preserve the all-important viscous layer and, at the same time, prevent pitting.

The optimal conditions are a lower total charge, careful stirring, and a higher electrolyte temperature to increase the limiting current density. Progress has been made toward optimizing these factors, and the electropolishing system is better understood. The next steps include moving toward a pulsed power system, where DC current is supplied intermittently. This would limit the formation of bubbles and lead to a less pitted surface. An inventory of samples should also be assembled to be chemically analyzed, as electropolishing changes not only the physical properties of a surface, but also the chemical properties.

6. Acknowledgements

I would like to thank Dr. Craxton for providing me with this extremely enriching experience and well-organized program. I would also like to thank my advisor Dr. Shmayda for his guidance and helpful weekly presentations. Finally, I would be remiss if I did not thank the individuals in my lab: Matt Sharpe, Cody Fagan, and especially Daniel Bassler, for their guidance and assistance throughout the course of the program.

7. References

- [1] W. T. Shmayda, M. Sharpe, C. Fagan, and W. U. Shroder, Laboratory for Laser Energetics, unpublished.
- [2] D. Landolt, "Fundamental Aspects of Electropolishing," *Electrochimica Acta*, Vol. 32, No. 1, pp. 1-11, 1987.
- [3] G. Yang, B. Wang, K. Tawfiq, H. Wei, S. Zhou & G. Chen (2017) Electropolishing of Surfaces: Theory and Applications, *Surface Engineering*, 33:2, 149-166, DOI: 10.1080/02670844.2016.1198452
- [4] A. Chandra, 2012, 'On the Mechanism of Niobium Electropolishing', Graduate Program in Materials Science and Engineering, The Ohio State University.

Improving the Uniformity of Revolver Designs for the National Ignition Facility

Yujia Yang

Brighton High School
Rochester, New York

Advisor: Dr. R. S. Craxton

Laboratory for Laser Energetics

University of Rochester
Rochester, New York

November 2017

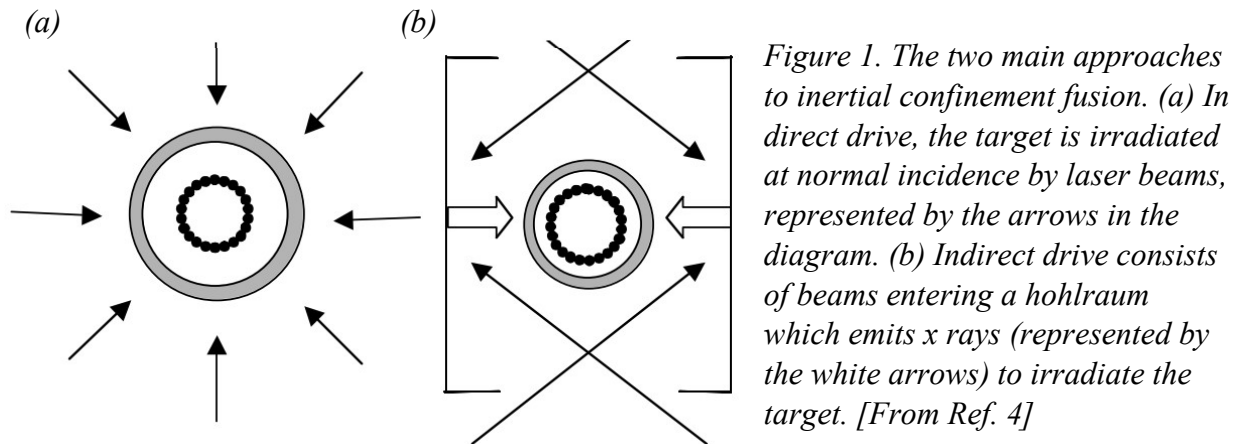
1. Abstract

The proposed *Revolver* target, consisting of nested beryllium, copper, and gold shells, is an alternative model, with approximately twice the radius, to the conventional target for implosions on the National Ignition Facility (NIF). A new design has been developed for *Revolver* using custom phase plates, since the maximum allowed defocus of current NIF phase plates produces focal spots that are too small, leading to significant nonuniformity in the azimuthal direction. This work considered variations of the size and ellipticity of the beams and their intensity profiles and pointings. The flux limiter was shown to have little effect on the uniformity of various designs, showing that the heat flow in *Revolver* is predominantly classical. The new design, developed using the 2D hydrodynamics simulation code *SAGE*, optimizes the NIF beam parameters to decrease the overall nonuniformity by a factor of 1.25 and to reduce the azimuthal nonuniformity by more than two-fold.

2. Introduction

Fusion is a nuclear reaction in which the nuclei of hydrogen isotopes, typically deuterium (1 neutron) and tritium (2 neutrons), combine to form a helium nucleus, releasing a high-energy neutron in the process. This reaction can be achieved by using laser beams to irradiate a target capsule containing these two isotopes of hydrogen, ablating the outer layer outwards, while an equal and opposite force compresses the deuterium and tritium (DT) inwards. Targets used for designs on the National Ignition Facility (NIF) at Lawrence Livermore National Laboratory are thin plastic (CH) shells, approximately 1.5 mm in radius, filled with DT in solid, liquid, or gaseous form. The lasers are able to bring the DT to conditions of extremely high temperature, density, and pressure, overpowering the Coulombic repulsion forces of positively charged nuclei to allow fusion reactions to occur for a short period of time. If the product of the compressed fuel's density and radius is large enough, the helium nuclei will deposit their energy in the fuel in an event known as ignition. If ignition occurs, the energy produced from the fusion reactions may equal the energy input, a phenomenon known as breakeven. Once high energy gain is achieved, when the energy output is approximately a hundred times the energy input, laser fusion can be considered an abundant alternative energy source.

There are currently two approaches to laser fusion: direct drive^{1,2} and indirect drive.³ Direct drive is illustrated by Figure 1(a), where laser beams directly irradiate the target from normal incidence at all angles. The University of Rochester's Laboratory for Laser Energetics currently uses this configuration on the OMEGA laser system to conduct their fusion experiments.



The other approach is indirect drive [Figure 1(b)], where the target lies inside a cylindrical hohlraum, made of a material with a high atomic number (typically gold). The lasers are aimed through two holes at the top and bottom of the hohlraum. When beams hit the hohlraum, it emits x rays that provide the energy needed to compress the target capsule. Though approximately 80% of the laser's initial energy is absorbed and given off as x rays, the target only absorbs about 20% of the energy, the rest being absorbed by the gold or escaping through the holes of the hohlraum. Despite this loss of energy, its efficiency is comparable to direct drive as indirect drive allows for greater uniformity through the x ray radiation. Though NIF is designed for indirect drive, it's currently carrying out both direct and indirect drive fusion experiments.

Since NIF's current configuration is set up for indirect drive, its beam ports aren't in the ideal locations for direct drive. There are a total of 48 laser beam ports, located in four rings in each hemisphere at angles θ of 23.5° , 30.0° , 44.5° , and 50.0° from the vertical. Laser beams are arranged in groups of four, called a quad, and each port contains one quad. If NIF's beams with their current configuration are all pointed towards the center of the target, the equator is extremely underdriven in comparison to the poles, resulting in an ellipsoidal shape rather than a sphere, as illustrated by Figure 2(a). As a result, a method with repointings of beams, called polar

direct drive,⁵ is used to obtain uniform direct drive implosions on NIF [Figure 2(b)]. In polar direct drive, the beams are repositioned towards the equator in order to drive the equator the same amount as the poles.

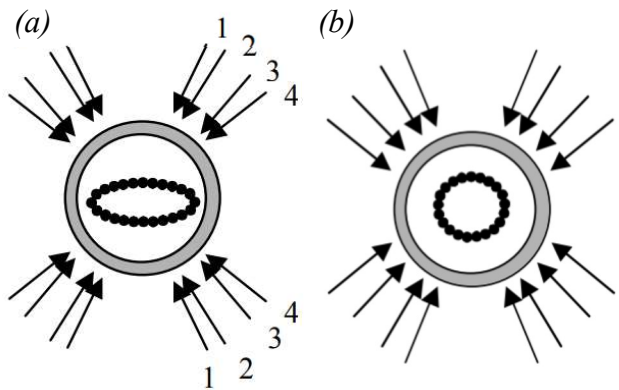


Figure 2. Two ways in which NIF's beam configuration for indirect drive can compress a target through direct drive. (a) When laser beams are aimed at the target's center, the poles compress much more compared to the equator. Rings 1-4 are indicated. (b) Repositioning beams to be pointed closer to the equator results in a nearly uniform implosion. [From Ref. 4]

A new, alternative design has been proposed for experiments on the NIF, shown in Figure 3, which displays a comparison of the standard target² [Figure 3(a)] to *Revolver*⁶ [Figure 3(b)]. *Revolver* is twice as large in diameter compared to the standard target, 6 mm to the standard 3 mm. It is claimed that its size and the properties of its materials make it a low risk, lower reward alternative to the high risk, high reward setup of the standard target.

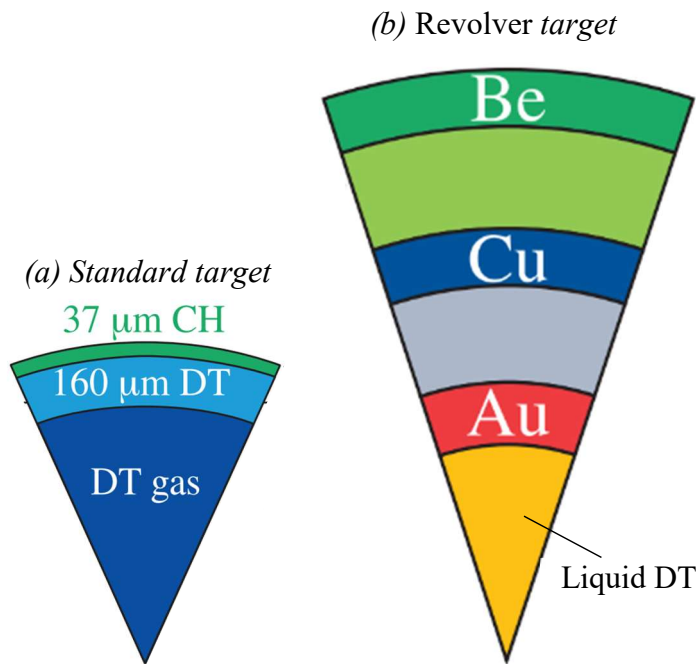


Figure 3. Comparison between the standard target and Revolver. (a) The standard target consists of deuterium-tritium gas surrounded by solid DT, contained in a plastic shell. (b) Revolver is approximately twice the diameter of the standard target, consisting of nested gold, copper, and beryllium shells. [(a) from Ref. 2, (b) from Ref. 6]

While the standard target consists of gaseous DT in the center, surrounded by a layer of DT ice and a thin layer of plastic (CH), *Revolver* consists of nested gold, copper, and beryllium shells, with liquid DT inside the gold shell and low-density foam inside the beryllium and copper shells.

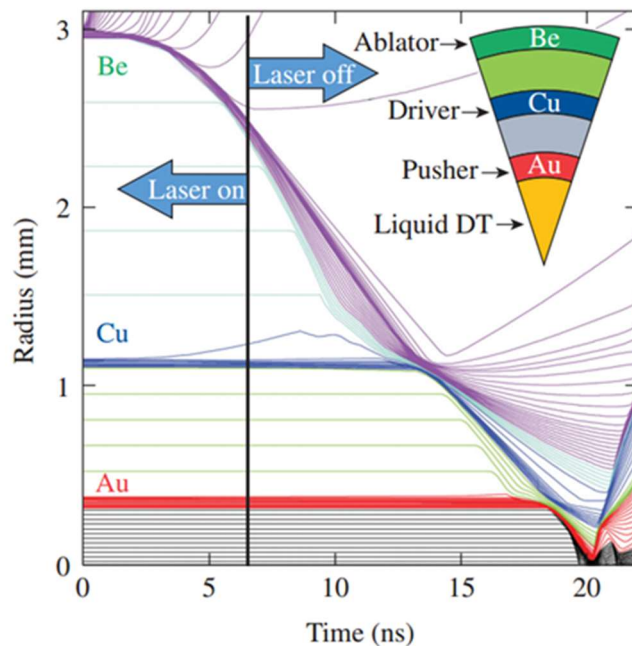


Figure 4. Radius vs. time graph of the Revolver target. The end of the laser pulse is shown by the black vertical line; the pulse continues for 6.7 ns before turning off. The beryllium absorbs the laser pulse energy for only a short period before imploding to hit the copper shell, which then implodes, hitting the gold shell that compresses the DT. It is claimed that refreshment of material at each successive shell reduces magnifying nonuniformity. [From Ref. 6]

Figure 4 shows the implosion path of the three shells.⁶ The laser pulse accelerates the beryllium inwards, which implodes to hit the copper shell, which then implodes to hit the gold shell that then compresses the liquid DT for fusion reactions to occur. The gold acts as a thermal blanket, allowing much of the heat from fusion to be retained within the deuterium. In addition, gold restricts the expansion of DT as fusion reactions occur, slowing the expansion of the *Revolver* target as a whole. The duration of the laser pulse is another major difference between the two targets. In the standard target, the laser is usually kept on until the target reaches full compression. However, on *Revolver*, the laser pulse [Figure 5] is short, turning off at 6.7 ns, before the beryllium reaches the copper shell [Figure 4].

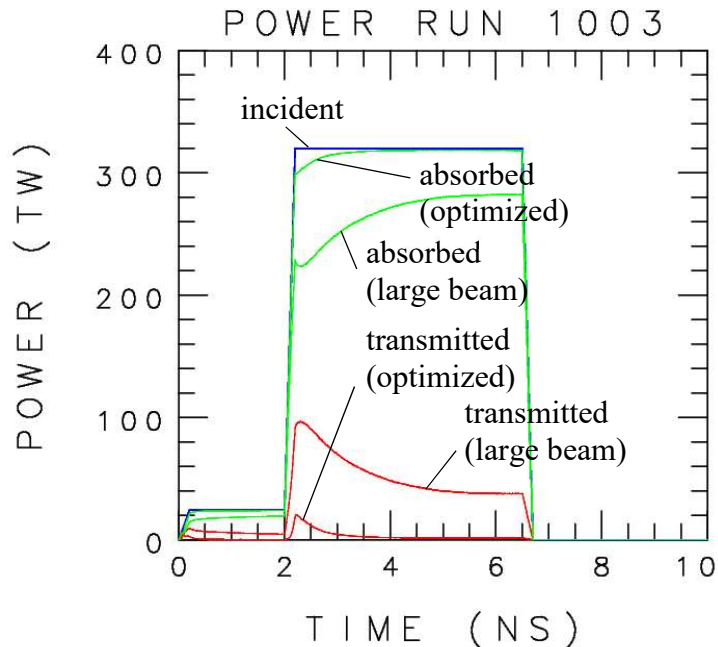


Figure 5. Power vs. time graph showing incident, absorbed, and transmitted power in terawatts. The temporal profile (incident) is shown in blue and has a step before the main laser pulse at 2 ns; the laser turns off at 6.7 ns. Green lines indicate absorbed energy and red lines show transmitted energy for two designs (see Section 6). [Runs 1003, 1284]

In a previous design⁷ using NIF's current phase plates with a defocus of 35 mm (approximately the maximum defocus available), the beam spots were small and produced regions of localized over- and undercompression. The goal of this work was to achieve uniformity along the azimuthal direction by using larger beam spots on the target's surface to compensate for the larger size of the *Revolver* target. In order to produce larger beam spots, custom phase plates were implemented to control the size and shape of beam spots on the target surface. Through bigger spots as well as other adjustments, including pointings and ellipticity of beam spots, azimuthal nonuniformity was reduced by more than two-fold through the use of custom phase plates, while overall nonuniformity was lowered as well.

3. Previous Design

A raytrace of a Ring 4 beam of the design using NIF's current phase plates⁷ is shown in Figure 6. As seen, the beam is aimed near the equator, and nearly all of the rays of this design are completely absorbed, while those that are deflected still deposit close to all of their energy in the target. Overall, the target has an extremely high energy absorption of 99.6%.

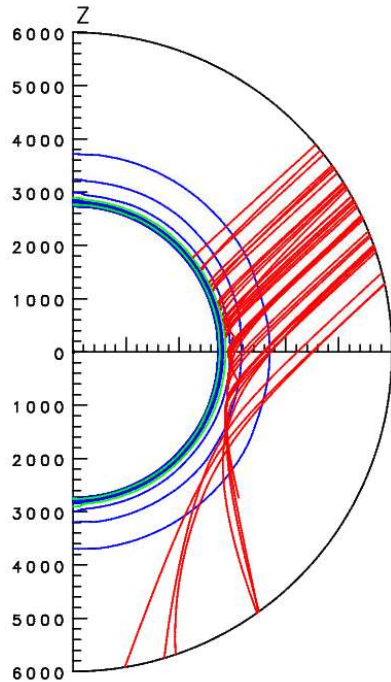


Figure 6. Raytrace of the bottom-right beam of Ring 4 at 5 ns of the design using NIF's current phase plates. All rays are aimed tightly in the vicinity of the equator. Density contours are shown by the blue circular lines, which show increasing density as the blue semicircles decrease in radius. The vertical axis on the left shows distances in μm . [Run 1002]

Due to this high absorption of beam energy by the equator, the equator is able to compress uniformly in relation to the poles, leading to an extremely low root-mean-square (rms) nonuniformity of 0.17% in the θ direction,⁷ as shown by the plot of the center-of-mass radius vs. θ in Figure 7, which comes from a 2D calculation that averages values over the azimuthal angle ϕ .

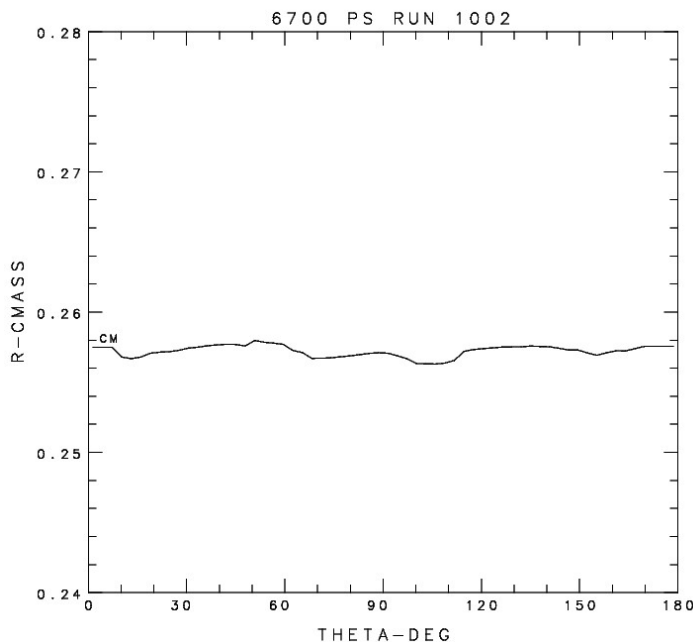


Figure 7. Center-of-mass radius (cm) vs. θ (degrees) of the lowest nonuniformity design using NIF's current phase plates. The line is almost completely straight, showing extremely low variation along the θ direction.

Even at maximum defocus, the current NIF beams produce small beam spots on the target,⁷ as seen by the 3D center-of-mass contour plot in Figure 8, resulting in several localized regions of over- and undercompression. This means that despite the low nonuniformity in the θ direction, variations along the ϕ direction are too large to achieve breakeven.⁸

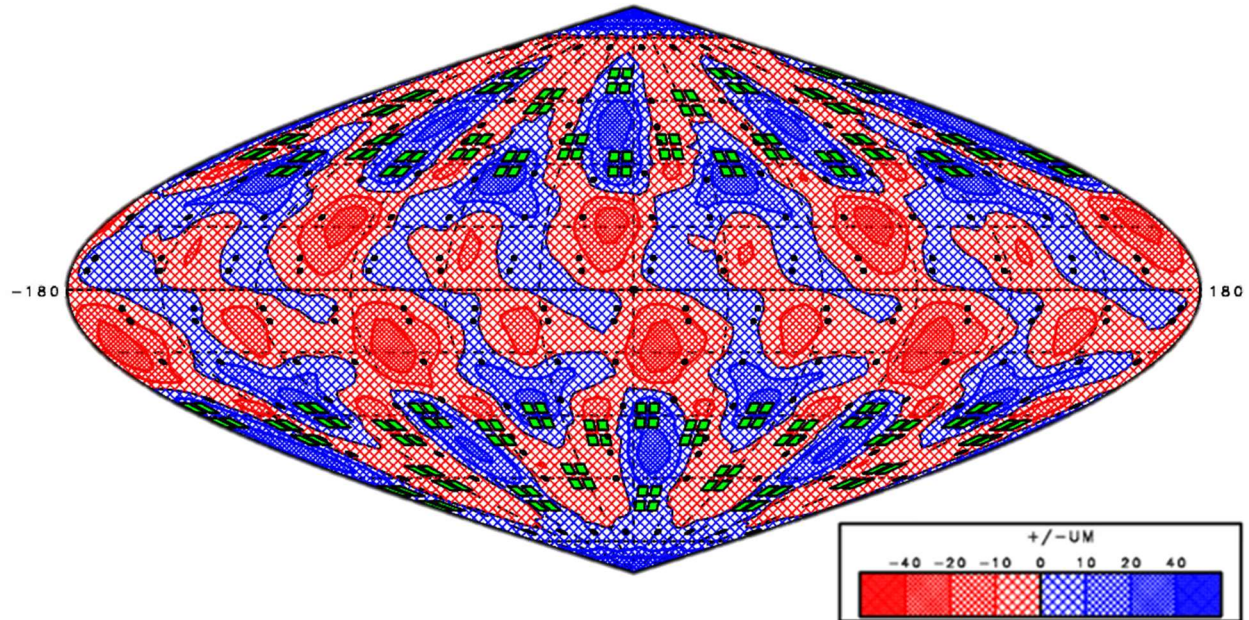


Figure 8. The 3D center-of-mass plot at 6.7 ns with contours indicating deviations from the average radius of the beryllium shell in μm (projection over the whole target surface). The green squares are the locations of beam ports and the black dots are the beam pointings. Blue regions indicate undercompression and red regions show overcompression. It can be seen that there are large variations along the azimuth, resulting in the ϕ variation being too large to achieve breakeven. The plot was constructed as described by Tucker by combining the center-of-mass plot of Figure 7 from a 2D simulation with the 3D energy deposition.⁹ [Run 1002]

The relationship between different elements of rms nonuniformity is given by the equation

$$rms^2 = (rms\theta)^2 + (rms\phi)^2 \quad (1)$$

where rms is the total rms nonuniformity, rms θ is the component of nonuniformity in the θ direction, and rms ϕ is the component of nonuniformity in the ϕ direction. The rms nonuniformity is defined as the rms of the deviations shown in Figure 8 divided by the average radius of 2580

μm . While the design has a relatively high total nonuniformity of 0.40%, it has an exceptionally low θ nonuniformity of 0.17%, which then makes its ϕ nonuniformity comparatively high at 0.36%, according to Equation 1. Another quantity of interest is the rms of deviations shown in Figure 8 divided by the distance traveled, since this gives the rms nonuniformity of the average velocity up to the end of the laser pulse. This value is 2.6%, far over the ideal 1% needed to achieve breakeven.

4. Optimized Design

One of the main parameters considered when implementing custom phase plates was the intensity profile of each beam. Beams that were larger in the horizontal (ϕ) direction were used compared with the previous design (Section 4.1). After the beam sizes in the ϕ direction were established, the ellipticity for each beam was set to decrease the beam sizes in the θ direction to deposit energy uniformly in that direction (Section 4.2). Section 4.3 addresses slight adjustments in beam pointings in both the θ and ϕ directions to minimize nonuniformities. Parameters were varied separately to initially determine which would improve the uniformity, then several parameters were simultaneously varied in incremental changes to arrive at the new design with the lowest nonuniformity. In the optimized design, azimuthal nonuniformity was significantly reduced with total nonuniformity being lower as well (Section 4.4). It should be noted that all beams maintained identical temporal profiles throughout and their energies were not modified.

4.1 Intensity Profiles

For each beam, the intensity I is given as a function of radius r by the equation

$$I(r) = I_0 \exp[-(r/r_0)^n] \quad (2)$$

where I_0 is the maximum intensity in the beam spot, r_0 is the radius of the beam spot, and n is the Gaussian order that determines the shape of the intensity profile within the beam. Figure 9 shows how varying n affects the intensity profile when the radius of the beam spot is $1500\ \mu\text{m}$.

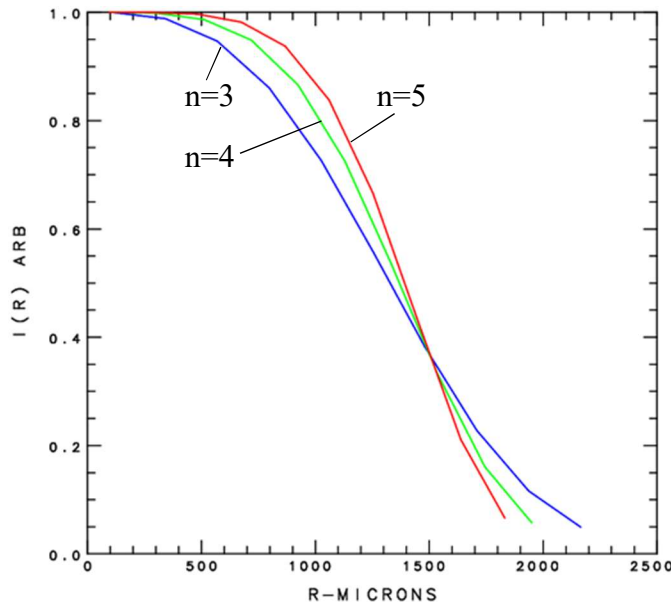


Figure 9. Graph of intensity of laser beam as a function of radius. The greatest intensity is at $r=0$ and it falls off as r increases. The variable that determines this falloff rate is n ; as n increases, the intensity profile becomes steeper. The blue, green, and red lines represent $n=3$, $n=4$, and $n=5$, respectively for an r_0 value of $1500\ \mu\text{m}$.

In the optimized design, beams in rings 1 and 2 had $r_0=1100\ \mu\text{m}$ and $n=3$. In both rings 3 and 4, n was also set to be 3, but the ring 3 quads had r_0 set to $1900\ \mu\text{m}$ while the r_0 of ring 4 beams was $2100\ \mu\text{m}$.

4.2 Ellipticity

Table 1 shows the shape of the focal spots on target in the optimized design as opposed to the previous design. Using NIF's current phase plates, the largest focal spot that can be obtained is approximately $1000\ \mu\text{m}$ in radius and takes the shape of a square with rounded corners, the shape and size that's set for all four rings. With custom phase plates, these beams can be made significantly more elliptical and larger. To obtain these elliptical beam spots on the target, r_0 from the intensity profile function was set to the horizontal radius of the ellipse, and a separate parameter set the ellipticity of each ring, which multiplied the r_0 to obtain the vertical radius.

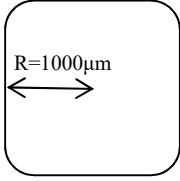
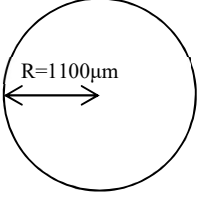
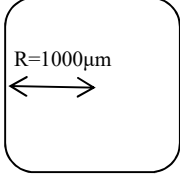
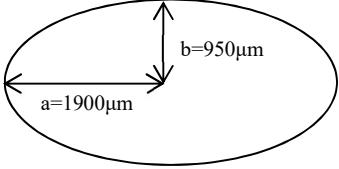
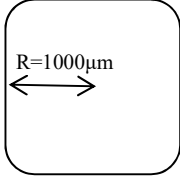
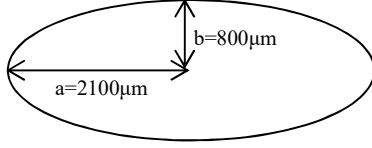
	Previous Design	Optimized Design
Rings 1, 2		
Ring 3		
Ring 4		

Table 1: Parameters of size and ellipticity in all rings for the previous and optimized designs. All beams in the optimized design increased in size. Beams of Ring 3 became a 2:1 ellipse with a radius of 1900 μm along the horizontal axis. Ring 4 beams became even more elliptical with a horizontal radius of 2100 μm and a vertical radius of 800 μm .

In rings 1 and 2, the optimized design's beams deviate very little from the previous design, the beams being only slightly larger, 1100 μm in radius to the previous 1000 μm , and more circular. In rings 3 and 4, the beam shapes of the optimized design contrast greatly to the previous design. The ring 3 beams are 2:1 ellipses with a radius of 1900 μm along the greater axis, nearly twice that of the previous 1000 μm . The ring 4 beams have an even greater ellipticity and are 2100 μm in radius along their greater axis, more than twice the length of the previous design.

Figure 10 depicts the energy deposition plots of the bottom-right beam of each quad in Ring 4 of the previous design [Figure 10(a)] as compared to the optimized design [Figure 10(b)]. It is evident that even when the energy deposition of only one beam in each quad is shown, the uniformity of energy deposition along the ring where the beams are pointed is greater in the optimized design.

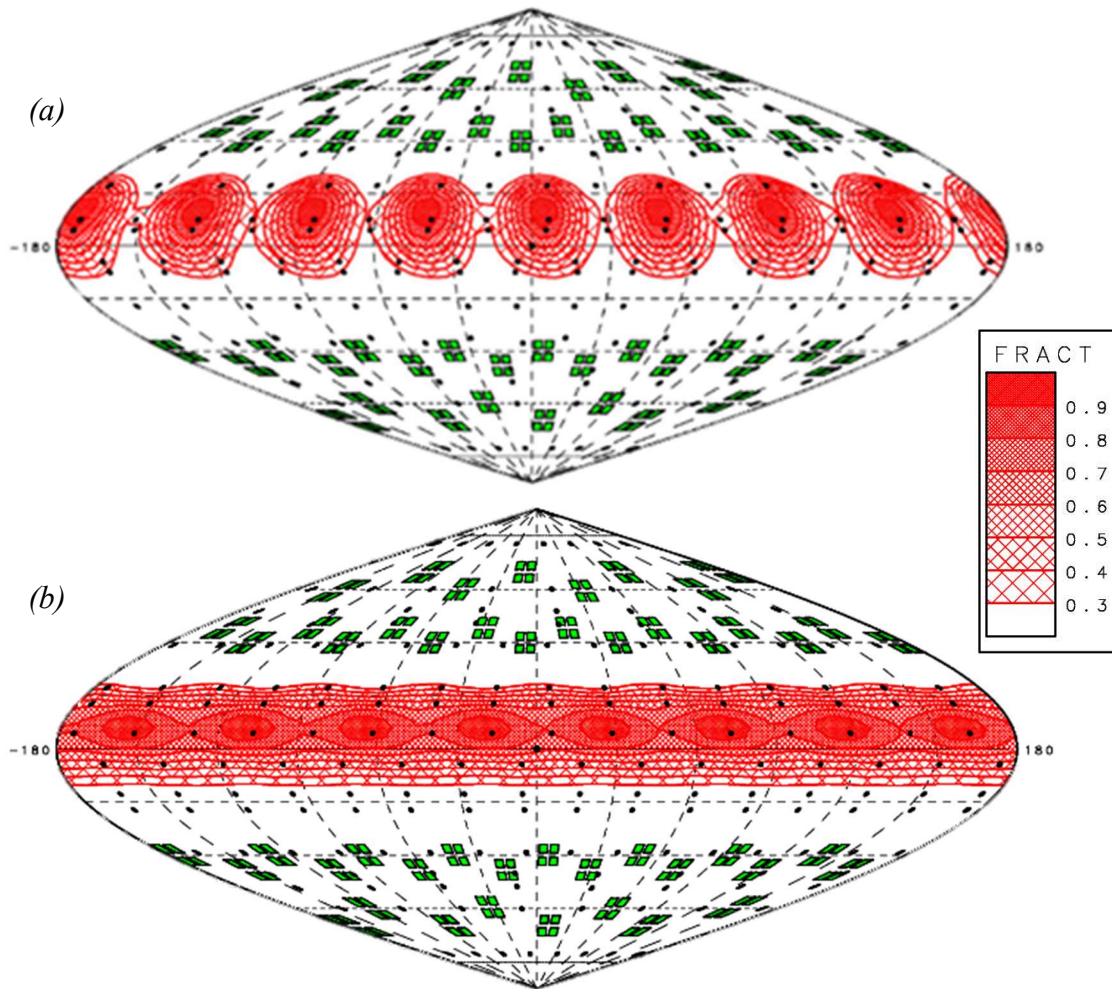


Figure 10. Energy deposition plots of the bottom-right beams of Ring 4 with contours showing fraction of maximum. (a) In the previous design using NIF's phase plates at maximum defocus, small beam spots are produced, depositing energy in eight distinct locations around the azimuth. (b) With bigger beam spots in the optimized design, the pattern becomes much less distinct and a more uniform band of energy appears around the azimuth. [Runs 1002, 1284]

When the energy deposition plots of all beams of ring 4 quads are compared between the two designs [Figure 11], the increase in uniformity is further emphasized. Whereas in the previous design, across the ring 4 beams, there is an eight-fold pattern of spots of greater energy deposition than the rest of the target, the optimized design has an almost completely uniform band of deposited energy across the target's surface, which makes the pattern nearly imperceptible.

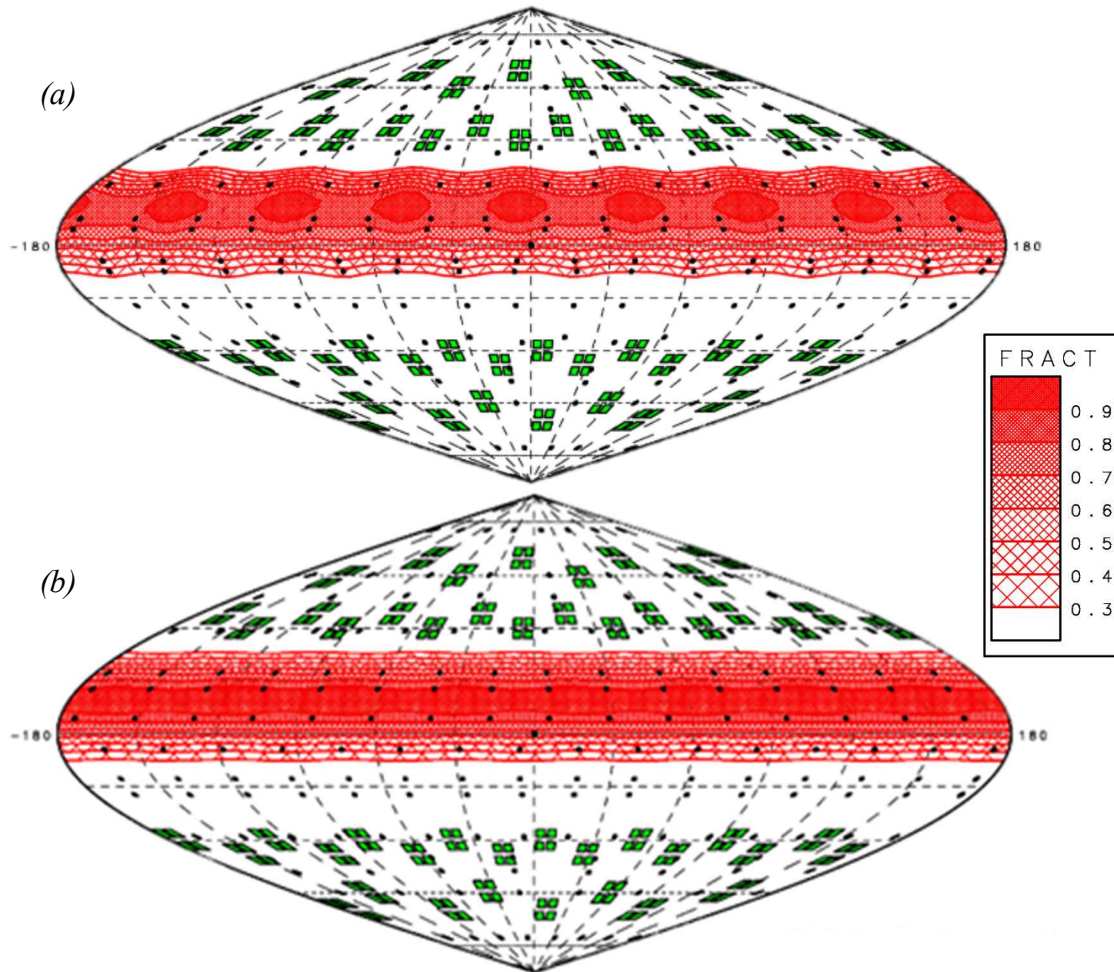


Figure 11. As Figure 10, but energy deposition plots of all beams of Ring 4 combined. (a) In the previous design, an eightfold pattern is still clearly visible, contributing to the localized overcompression regions on the 3D center-of-mass plot (Fig. 8). (b) In the optimized design, bigger beam spots greatly diminish nonuniformities in energy deposition. [Run 1002, 1284]

4.3 Pointings

Though the pointings of the optimized design do not differ drastically from the previous design, the slight modifications contribute to minimizing nonuniformity. Only pointings of Rings 3 and 4 were shifted to decrease nonuniformity. Changes in the ϕ direction were almost insignificant. All angle shifts were set to either 11.25° or -11.25° to maintain uniformly distributed energy in the ϕ direction. The total ϕ angle of 360° has to be split between the sixteen top and sixteen bottom beams in each of Rings 3 and 4, meaning they should all be positioned

22.5° from each other. Setting the right beams of each quad to 11.25° and the left beams to -11.25° ensures equal spacing. The pointings in the θ direction were changed as shown in Table 2. In the previous design, the top and bottom beams of each quad could be closer in the θ direction and still maintain the same energy deposition uniformity. However, with elliptical beam spots that were shorter vertically [Table 1], the top and bottom beams of each quad had to be spread further apart in the θ direction in order to maintain uniform distribution of energy.

	Previous Pointings	Optimized Pointings
Ring 3 top beams	53°	51°
Ring 3 bottom beams	55°	67°
Ring 4 top beams	80°	73°
Ring 4 bottom beams	84°	84°

Table 2. Pointings in Rings 3 and 4 of the previous and optimized designs in the θ direction. The pointings in Rings 3 and 4 were spread further apart in the optimized design to compensate for the smaller vertical size of the beam spots.

4.4 Improved Azimuthal Uniformity

In the optimized design where custom phase plates are implemented, the nonuniformity in the ϕ direction is drastically reduced, more than two-fold, from the design using NIF's current phase plates. Figure 12 shows the 3D center-of-mass radius plot for the optimized design, and when compared with Figure 8, it is clearly evident that the variation in the azimuthal direction has been reduced significantly. The small, localized regions of over and under-compression that were once present have been mitigated and the contours on the plot of the optimized design don't even pass the +20 μm and -20 μm marks (aside from small regions near the poles). In the optimized design, the total rms nonuniformity is 0.32% (a decrease of 1.25 from the previous design), the nonuniformity in the θ direction is 0.27%, and the nonuniformity in the ϕ direction is 0.17%, a major drop from the previous ϕ nonuniformity of 0.36%. In addition, the average rms velocity nonuniformity is reduced from 2.6% for the previous design to 2.1% for the optimized design, of which 1.8% is in the θ direction and 1.1% is in the ϕ direction.

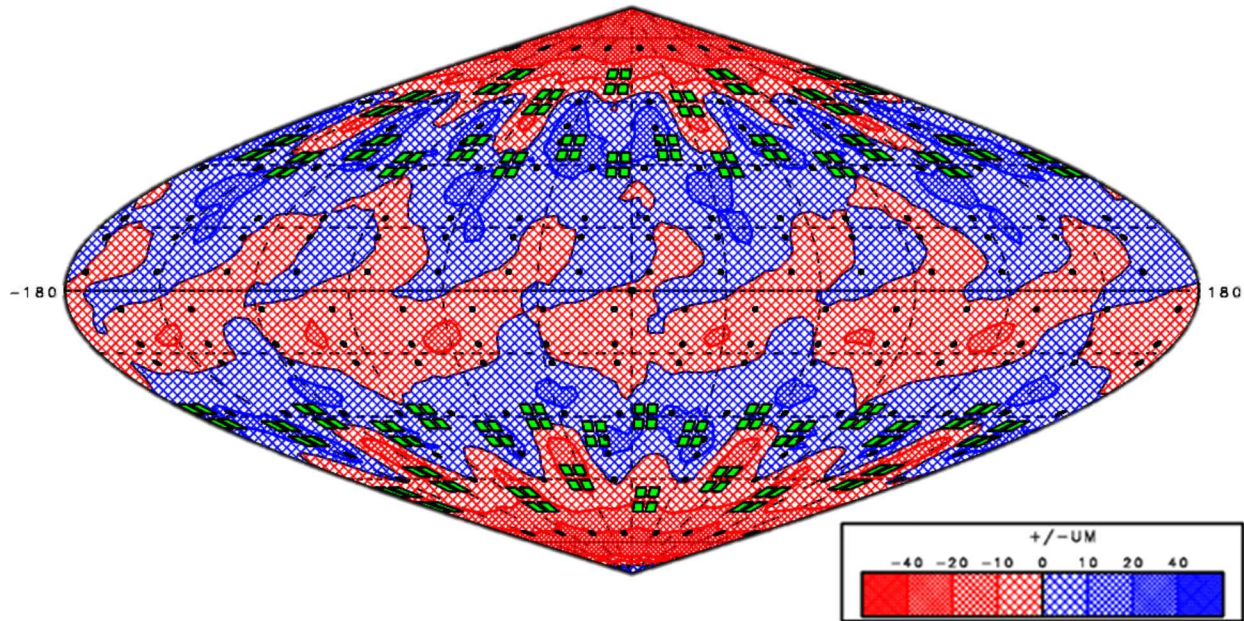


Figure 12. 3D center-of-mass plot for the optimized design at 6.7 ns. This has a much lower nonuniformity in the azimuthal direction than the previous design. The regions of over- and undercompression are no longer localized to small regions and are spread out along the azimuth. It should be noted that all 3D center-of-mass plots share the same scale. [Run 1284]

Plots of the energy deposition vs. ϕ at θ angles of 60° and 50° are shown in Figure 13, where red represents the design using NIF's current phase plates and blue represents the optimized design. At $\theta=60^\circ$ [Figure 13(a)], the red line has approximately twice the variation in intensity as the blue line, similar to the total ϕ variation of the previous design that is approximately twice that of the optimized design. At $\theta=50^\circ$ [Figure 13(b)], the difference in azimuthal variation is much greater: the azimuthal variation of the previous design is nearly five times that of the optimized design. This distinctly illustrates the improvement of azimuthal uniformity in the optimized design. Despite clearly visible improvements, detailed simulations similar to those run in Reference 8 are needed to see if the optimized design will reach breakeven.

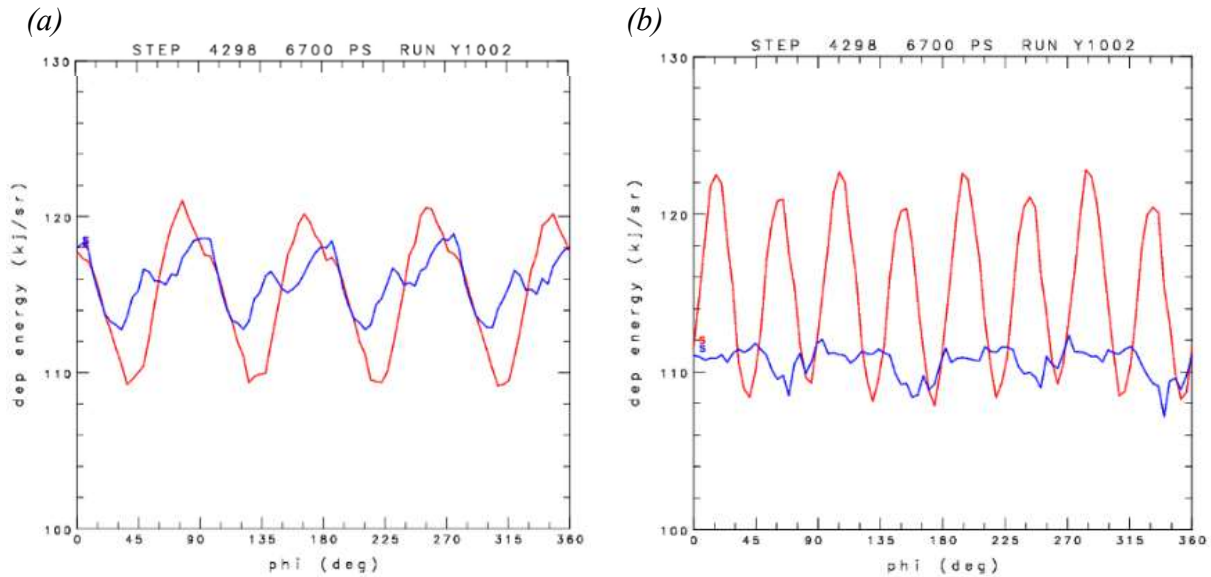


Figure 13. Graphs of deposited energy vs. ϕ at $\theta=60^\circ$ (a) and $\theta=50^\circ$ (b) for the previous (red) and optimized (blue) designs. At $\theta=60^\circ$, the range of azimuthal variation of the previous design is approximately twice that of the optimized design. At $\theta=50^\circ$, the range of azimuthal variation of the previous design is almost five times that of the optimized design.

5. Flux Limiter

In the presence of steep temperature gradients, the classical formula for calculating heat flow breaks down, as it predicts heat flow to be grossly overestimated. In its place, a separate formula including the flux limiter,¹⁰ an adjustable constant, is used to more accurately predict the heat flow.

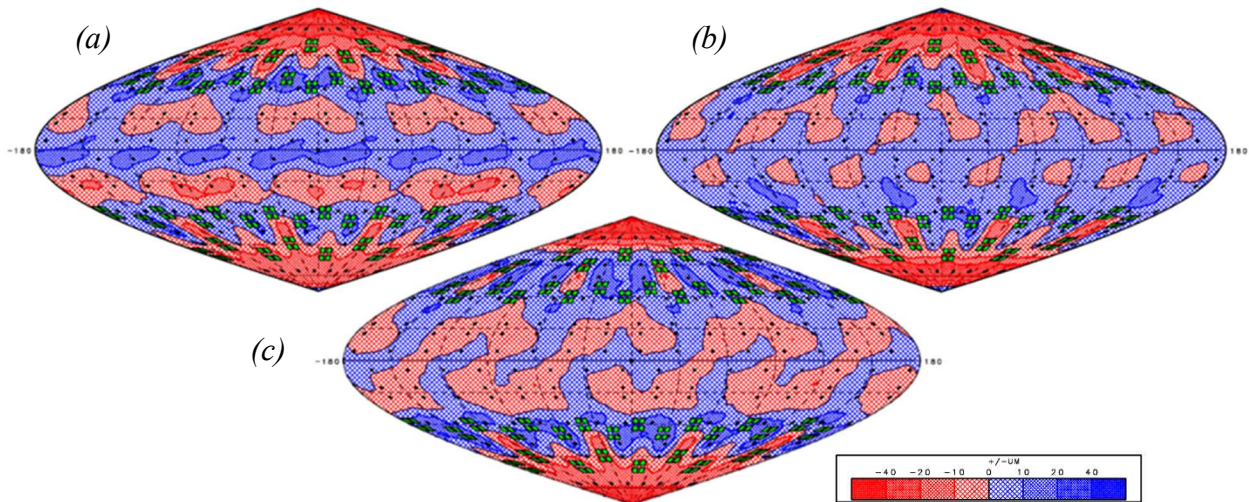


Figure 14. 3D center-of-mass plots at 6.7 ns for varying flux limiters (a) 0.04 (b) 0.08 (c) 0.1. Refer to Figure 12 for the plot of $f=0.06$. [Runs 1294, 1312, 1315]

The optimized design used a flux limiter of 0.06, the common value that has been shown to estimate heat flow with the greatest accuracy in many experiments. To investigate the sensitivity of *Revolver* to changes in flux limiter, three additional runs were done, as shown by the 3D center-of-mass plots of the three runs in Figure 14. Even after changing the value of flux limiter, nonuniformity remained almost the same as before.

Table 3 shows that while absorption increases slightly as flux limiter increases, there is no relationship between flux limiter and nonuniformity, as there is no observable pattern in changes of rms nonuniformity as the flux limiter increases. This demonstrates that heat flow within the *Revolver* target is mainly classical, a positive attribute, as its behavior can be predicted with high accuracy using the classical formula.

Flux Limiter (f)	0.04	0.06	0.08	0.1
rms (%)	0.35	0.32	0.32	0.32
rms θ (%)	0.31	0.27	0.28	0.26
rms ϕ (%)	0.16	0.17	0.15	0.19
Absorption (%)	98.3	98.9	99.0	99.1

Table 3. Rms nonuniformity values across a range of flux limiter values. All rms elements change very little with respect to flux limiter. Within the already low variations in rms, there is no observable pattern in how increasing the flux limiter affects the rms.

6. Too-Large Beam

Although a larger beam spot was absolutely essential in reducing nonuniformity in the azimuthal direction, several problems arise when too large of a beam size is implemented, such as a circular beam with an r_0 of 3000 μm and $n=4$. Figure 15 shows the 3D center-of-mass plot at 6.7 ns to illustrate the problem: the equator is greatly undercompressed, resulting in much larger values of radius when θ is close to 90 degrees. There is a very clear blue band around the equator of the surface of the target shell, showing a region of extreme undercompression. The poles are much more compressed than the equator, leading the target capsule to be an ellipsoid shape

rather than the desired sphere. The maximum and minimum values are $+39.5\ \mu\text{m}$ and $-46.3\ \mu\text{m}$, respectively.

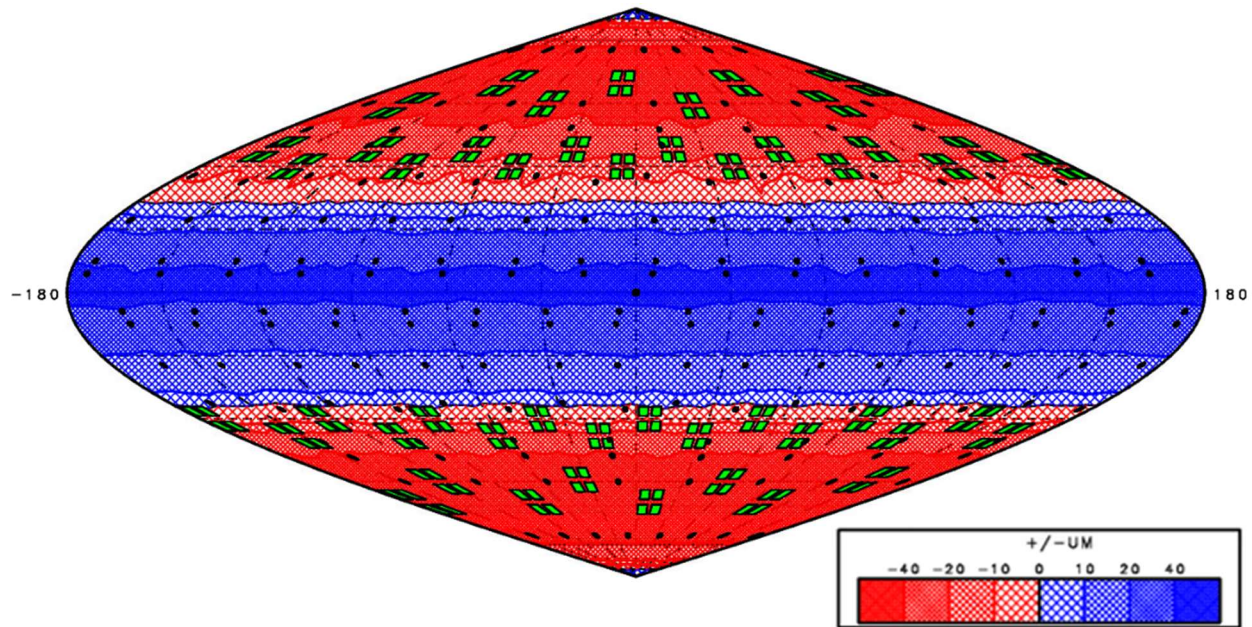


Figure 15. A 3D center-of-mass plot for the design using too-large beams. A distinct blue band is clear across the equator, showing a region of great undercompression. [Run 1003]

An additional problem that's a result of a too-large beam is the large amount of laser energy that misses the target altogether, as shown by the raytrace plots in Figure 16. Figure 16(a) shows the raytrace of the bottom right beam of Ring 4 of the optimized design, where a large portion of the rays hit the target near the equator and are absorbed. Of the deflected rays, almost all of their energy is still deposited in the target. However, the raytrace of the too-large beam [Figure 16(b)] shows that a large portion of the rays from the beam miss the target altogether. Unlike the optimized and previous designs, the rays aren't tightly focused in the vicinity of the equator. The beam size is so large that even though most of the rays are being focused *near* the equator, a lot of rays completely pass by the target without hitting it. The problem with rays that are not significantly deflected is that they can then pass through opposite ports and damage laser optics.

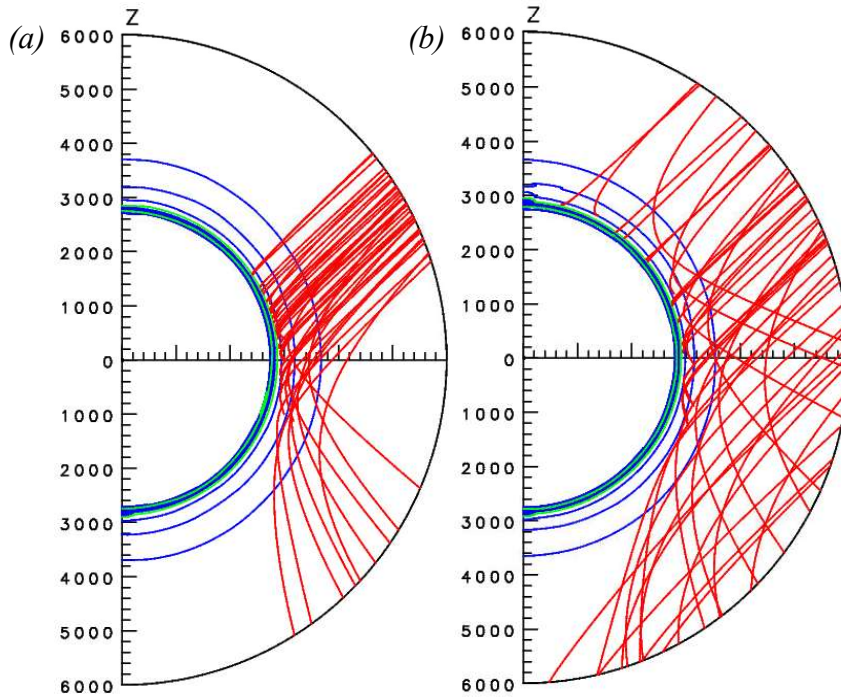


Figure 16. Raytrace plots showing the optimized design (a) and the too-large beams (b) at 5 ns. The rays of the optimized design are almost all absorbed by the target, with the energy of those deflected still being mostly absorbed. With the too-large beam, a large portion of rays pass straight by the target, potentially damaging laser optics. [Runs 1284, 1003]

Since a significant portion of the beam's rays pass by the target completely, there is a relatively large amount of transmitted energy from the too-large beam, as shown by Figure 5, which depicts the incident beam energy as well as absorbed (green) and transmitted (red) energies of the too-large beam and the optimized design. While in the optimized design the target absorbs 98.9% of the energy, the too-large beam has an absorption of only 83.2%. The problem arises with the great number of rays completely missing the target from the too-large beam. The large amount of scattered light that comes from the too-large beam, with a maximum value of 215 kJ/sr, compared to a maximum value of scattered light for the optimized design, a mere 9.6 kJ/sr, poses a critical problem that risks damaging the laser optics, since the safety level of scattered light is approximately 60 kJ/sr, as described by Huang.¹¹

7. Conclusion

By implementing custom phase plates, an optimized design was developed to reduce nonuniformity in the azimuthal direction of *Revolver*. The small, localized regions of over- and

undercompression were eliminated to produce bigger, elliptical beam spots to deposit energy uniformly in the azimuthal direction. Pointings were adjusted, mainly in the θ direction, to distribute energy uniformly in the vertical direction. The flux limiter was shown to have little to no effect on the uniformity, suggesting that heat flow in *Revolver* is generally classical. Though a bigger beam size in the horizontal direction was essential to achieving lower nonuniformity in the azimuthal direction, a too-large beam was shown to have inadequate uniformity and problems in the large amount of laser light that passed by the target completely. Custom phase plates improved azimuthal uniformity by more than two-fold and improved the total uniformity as well.

8. Acknowledgements

First, I would like to thank my family for their endless support throughout the program and Mr. Bradley Allen for his encouragement of my interest in physics. I'd also like to thank the Laboratory for Laser Energetics for providing myself and my fellow interns the materials and resources necessary for our projects. Finally, I'd like to offer my utmost appreciation to my advisor Dr. R. S. Craxton for his invaluable help and guidance, and for giving us this incredible opportunity.

9. References

1. J. Nuckolls, et al., "Laser Compression of Matter to Super-High Densities: Thermonuclear (CTR) Applications," *Nature* **239**, 139 (1972).
2. R. S. Craxton et al., "Direct-Drive Inertial Confinement Fusion: A Review," *Phys. Plasmas* **22**, 110501 (2015).

3. J.D. Lindl, “Development of the Indirect-Drive Approach to Inertial Confinement Fusion and the Target Physics Basis for Ignition and Gain,” *Phys. Plasmas* **2**, 3933 (1995).
4. A. M. Cok, “Development of Polar Direct Drive Designs for Initial NIF Targets,” Laboratory for Laser Energetics High School Research Program (2006).
5. S. Skupsky, et al., “Polar Direct Drive on the National Ignition Facility,” *Phys. Plasmas* **11**, 2763 (2004).
6. K. Molvig et al., “Low Fuel Convergence Path to Direct-Drive Fusion Ignition,” *Phys. Rev. Lett.* **116**, 255003 (2016).
7. E. M. Garcia, private communication.
8. P.W. McKenty et al., “Evaluation of the Revolver Ignition Design at the National Ignition Facility Using Polar-Direct-Drive Illumination,” presented at the 59th Annual Meeting of the American Physical Society Division of Plasma Physics, Paper N07-5, October 2017.
9. L. Tucker, “A Design for a Shock Ignition Experiment on the NIF Including 3-D Effects,” Laboratory for Laser Energetics High School Research Program (2011).
10. R.C. Malone, et al., “Indications of Strongly Flux-Limited Electron Thermal Conduction in Laser-Target Experiments,” *Phys. Rev. Lett.* **34**, 721 (1975).
11. P. Huang, “Analysis of Unabsorbed Light from Exploding-Pusher Targets Used for Proton Backlighting on the National Ignition Facility,” Laboratory for Laser Energetics High School Research Program (2015).